AD-A262 887

MENTATION PAGE

Form Approved
OMB No. 0704-0188

REPORT DATE	3. REPORT TYPE AND DATES COVERED
2/10/92	Annual: 7/15/92 - 1/14/93

4. TITLE AND SUBTITLE
Selective Processing Techniques for Electronics and Opto-electronic Applications: Quantum-well Devices and Integrated Optic Circuits

5. FUNDING NUMBERS
F49620--92-J-0414

6. AUTHOR(S)
Prof. Richard M. Osgood, Jr.

7. PERFORMING ORGANIZATION NAME(S) AND ADDRESS(ES)
Columbia University
Microelectronics Sciences Laboratories
500 West 120th Street
1001 Schapiro CEPSR
New York, NY 10027

8. PERFORMING ORGANIZATION REPORT NUMBER
AFOSR-TR-

9. SPONSORING/MONITORING AGENCY NAME(S) AND ADDRESS(ES)
Dr. Jane Alexander
DARPA
3701 N. Fairfax Drive
Arlington, VA 22203-1714

Dr. Howard Schlossberg
AFOSR
Program Manager NE
Building 410, Bolling AFB
Washington, DC 20332

10. SPONSORING/MONITORING AGENCY REPORT NUMBER
3801

11. SUPPLEMENTARY NOTES

DTIC ELECTE APR 01 1993 S E D

12a. DISTRIBUTION/AVAILABILITY STATEMENT
Distribution Unlimited

12b. DISTRIBUTION CODE

13. ABSTRACT (Maximum 200 words)

During this period, significant headway has been made on the key contract objectives. Several novel integrated optical devices have been demonstrated, and simulation of new devices is guiding further experiments. Our low-damage cryogenic etching technique has been demonstrated to be suitable for sub-micron patterning, and applied to device fabrication. Finally, light-induced wet-etching techniques have been used in several new and important areas of application.

93-06616

93 4 01 054

14. SUBJECT TERMS	15. NUMBER OF PAGES
Wavelength Filters, Quantum Wells, Star Couplers, Semiconductor lasers, IR Filters, Isolators, Integrated Optics, Anisotropic Etching, InP, Via Etching, Optical Wave Simulation.	30
	16. PRICE CODE

17. SECURITY CLASSIFICATION OF REPORT	18. SECURITY CLASSIFICATION OF THIS PAGE	19. SECURITY CLASSIFICATION OF ABSTRACT	20. LIMITATION OF ABSTRACT
Unclassified	Unclassified	Unclassified	Unclassified

SELECTIVE PROCESSING TECHNIQUES FOR ELECTRONIC AND OPTO-ELECTRONIC APPLICATIONS: QUANTUM-WELL DEVICES AND INTEGRATED OPTIC CIRCUITS

Richard M. Osgood, Jr.

Columbia University
Microelectronics Sciences Laboratories
500 West 120th Street
1001 Schapiro CEPSR
New York, NY 10027

Submitted: February 10, 1993

Annual Technical Report for the Period
July 15, 1992 - January 14, 1993

Distribution Unlimited

Prepared For
USAF, AFSC
Air Force Office of Scientific Research
Building 410
Bolling AFB, DC 20332-6448

Sponsored by
Defense Advanced Research Projects Agency (DARPA)
DARPA Order No. 6321
Monitored by AFOSR under Contract #F49620-92-J-0414

Table of Contents

Introduction

The goal of the current DARPA/AFOSR program is to apply selective processing techniques developed at Columbia to the fabrication of specific device structures for both integrated optical and microelectronic devices and systems. Two key technology areas are addressed: a) new techniques appropriate to processing sensitive MQW devices, and b) fabrication of integrated optical devices and circuits. The statement of work for this program is provided in the Appendix. As will be seen in this report, significant headway has been made on these objectives in the first six months of the project, the time period which this report covers. The work described in this report is divided into the following categories:

A. Integrated Optical Devices and Technology

B. Integrated Optical Device and Circuit Modeling

C. Cryogenic Etching for Low-Damage, Sub-Micron Processing of MQW's

D. Applications of Through-Wafer Via Etching

E. Selective Vertical Etching of GaAs/AlGaAs MQW's

A key aspect of this work has been collaborations with other industrial and university partners. Our industrial partners have included Ray Wolfe at AT&T, Paul Lin at Bellcore, Frank Tong at IBM, Jim Yardley at Allied Signal, and Bill Hooper at Hughes Research Laboratories.

A. Integrated Optical Devices and Technology

In the previous DARPA/AFOSR program, we succeeded in developing a fabrication technology suitable for rapid prototyping of passive and active integrated optical device

structures. This work is described in previous reports, and is also presented in Refs. 1 and 2. In addition, we began to apply the techniques to the fabrication of new and complex devices, such as the narrow-band channel-dropping filter (CDF) proposed by H.A. Haus at M.I.T., and end-facet grating based multiplexers.

1. *Channel Dropping Filter*

In the current program, we have completed work on demonstrating several novel devices. First, the CDF described above has been fabricated and tested, and was found to exhibit the basic behavior predicted from the theory, including a sub-Angstrom bandwidth. This is the first experimental realization of this important telecommunications device. Second, we have produced the first thin-film-magnet magneto-optic isolator, and the device exhibits an isolation ratio of 21 dB. Finally, we have fabricated several different designs of integrated optic waveguide modulators, and these exhibit low switching voltage and high extinction ratio.

In earlier reports, we described our work on fabricating a narrow-band channel-dropping filter of a novel design proposed by H.A. Haus at M.I.T. The very first devices showed promise, but required redesign. Late in the last contract period we completed a redesign and second fabrication run using our prototyping technology, in collaboration with P.S.D. Lin at Bellcore for e-beam writing, and the NNF at Cornell for grating etching.

In the early part of this current program, we analyzed the new devices using a recently introduced tunable laser source from HP. A portion of the response is shown in Fig. 1, which shows the output of the resonator arm versus wavelength. A strong resonant peak is observed, which corresponds to the predicted transmission resonances. The power transfer of 30% approaches the theoretical maximum of 50% for this design. Finally, the bandwidth is 0.8Å

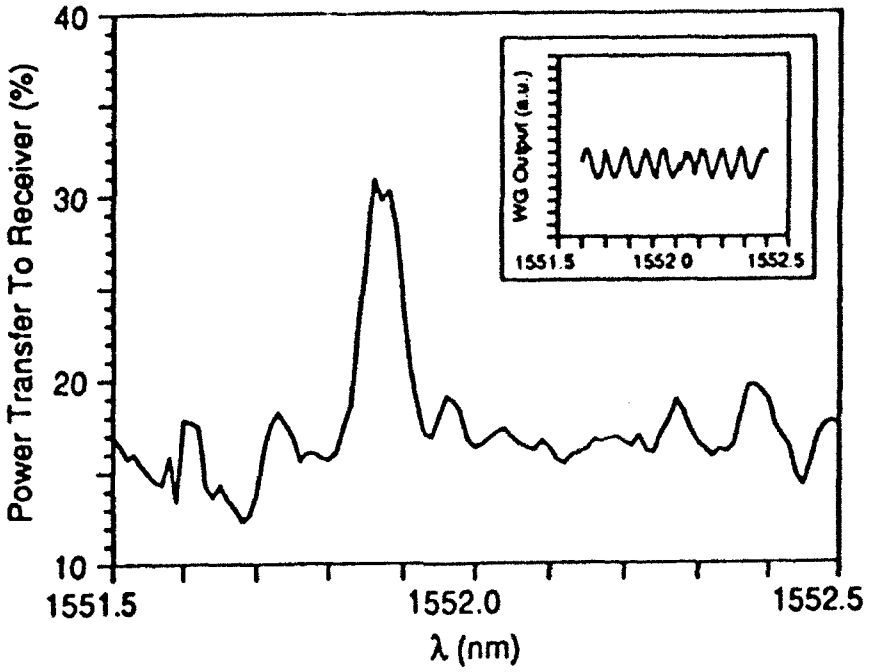

Figure 1. Response of narrow-band channel dropping filter. The bandwith is 0.8Å FWHM.

FWHM, within the predicted sub-Angstrom range, and the narrowest value of any integrated filter design. This is the first demonstration of a CDF of this type, and represents an important step in the development of this technology area. The work was published and is described fully in Ref. 3 (also found in Appendix B).

2. *Thin Film Isolator*

In the area of integrated optical isolators, we have also made significant accomplishments during this period. In the current proposal, we put forth a concept for a magneto-optic isolator driven by thin-film magnets, which could be integrated directly onto optical chips. Detailed calculations of the magnetic fields produced by recently developed magnetic thin-films showed that saturation of properly designed Bi-YIG materials might be achieved.

In this contract period, we brought together the elements of the design through

collaboration with R. Wolfe at Bell Labs. who provided the Bi-YIG waveguide, and C.J. Gutierrez and G.A. Prinz at NRL who provided thin-film magnets according to our design specifications. Fabrication and testing of the final device was done by us at Columbia. Measurements indicate that the thin-film magnets can nearly saturate the Bi-YIG. In addition, the device exhibited good isolation behavior as shown in Fig. 2, which displays the optical output through the Bi-YIG waveguides for two different orientations of the magnetic thin-film. The isolation ratio obtained was 21 dB. This result represents the first demonstration of a thin-film magnet magneto-optic isolator. This has been published and appears in Ref. 4 (also found in Appendix B).

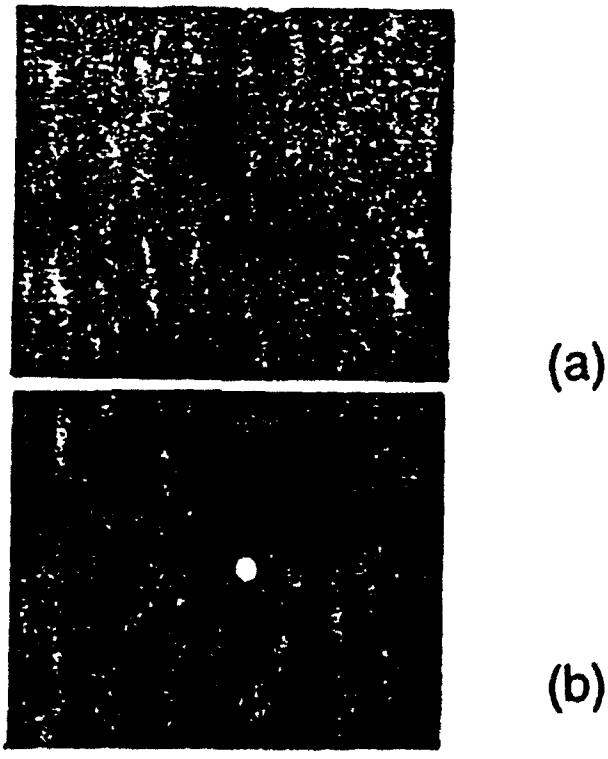

Figure 2. Output of thin-film-magnet magneto-optic isolator for two different film orientations.

3. *Waveguide Modulators*

Finally, in this period, we have successfully used our prototyping capability to fabricate several designs for integrated optical waveguide modulators. Those include a polarization modulator, an amplitude modulator, and a Mach-Zehnder modulator.

The first modulator we fabricated was an electro-optic polarization modulator.[2] This was reported previously, however it is useful to summarize the results in order to understand the new designs. The etched portion of the device was a groove-defined straight waveguide. The waveguide metallization was fabricated by a conventional evaporation of aluminum and patterned with laser direct writing of photoresist, which left an electrode on either side of the waveguide, allowing an electric field to be applied within the waveguide core.

The device was tested by using a polarization-maintaining fiber to launch light into the waveguide structure and analyzing the output with an external IR polarizer set at 90° to the input polarization. Figure 3a shows the transmission as a function of applied voltage, and demonstrates an extinction ratio of 17 dB and a V_π of 4 V.

We used the device described above in conjunction with an on-chip polarizer to build a simple, integrated amplitude modulator. Such a device has not been previously reported. The first fabrication steps of this device were similar to those that led to the polarization modulator described in the above paragraphs. However, the electrodes were not deposited along the whole length of the waveguide. A part of the device was left for the positioning of a polarizer. The polarizing element was a thin metal film which is known to exhibit strong polarization-sensitive optical loss. In particular, the presence of the aluminum strip allows selective TE_0 mode transmission, while the TM_0 mode and higher-order modes do not transmit through the guide.

This filter action is explained by modal repulsion from the metal wall. For our device, this element consisted of a strip of aluminum positioned on top of the waveguide, in the center of the area with no electrodes. In our experiments, laser-defined CVD[5,6] was used to deposit the polarizer. This technique was selected because it is maskless and discretionary. Thus the metallized region may be defined and adjusted without exposing the device to a second photopatterning step. Prior to fabricating this device, we studied the polarization-sensitive attenuating properties of the laser-defined aluminum lines. For this study, aluminum lines of various lengths were direct-written on straight waveguides, and the output intensity was measured as a function of the pad length and normalized to that of a straight waveguide with no aluminum. This measurement was made for both TE and TM and the results showed over 10 dB discrimination of TM compared to TE.

In order to test the device, we launched light polarized at TM into the waveguide structure. Figure 3b shows the transmission as a function of applied voltage, and exhibits an extinction ratio of 13 dB and a V_π of 6 V.

The third modulator that we designed is a Mach-Zehnder-interferometer-based modulator. In the fabrication of this device, a much complex and accurate writing sequence is required. The electrode configuration we used is again that of coplanar strips where the electrodes are on either side of each of the two parallel arms, allowing an electric field to be applied within the waveguide core of each arm. Since a central electrode can be shared by both guides, a total of three electrodes are required for this device. Again, we used our computer-controlled direct-

(a)

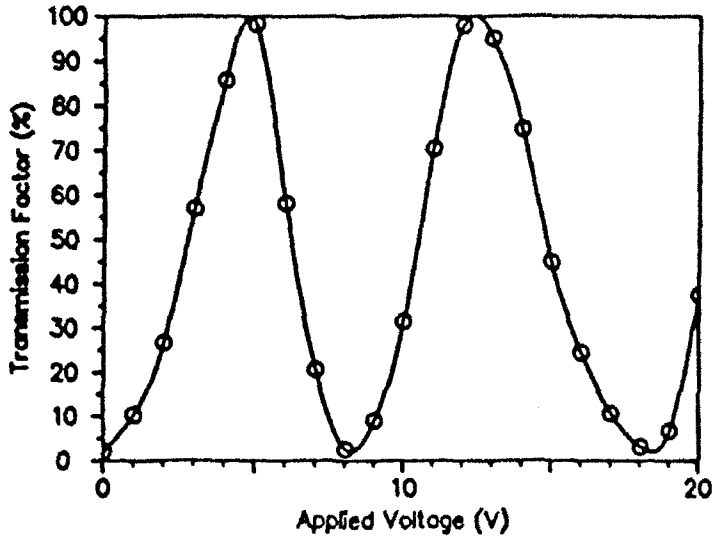

(b)

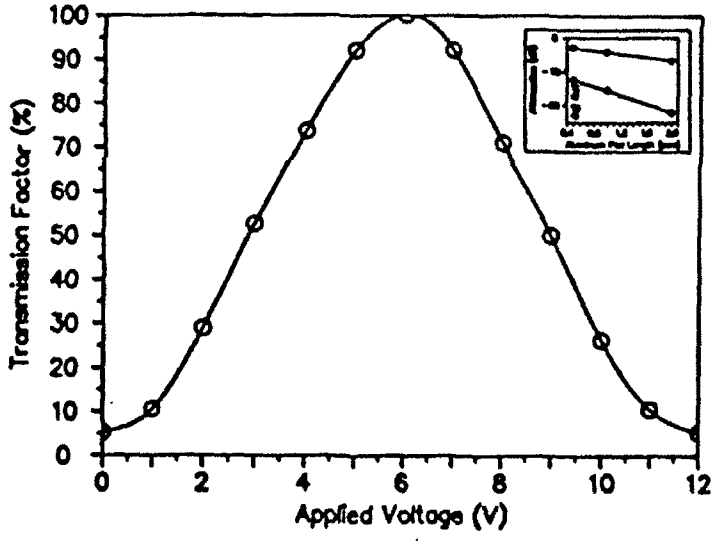

Figure 3a,b. Laser-fabricated amplitude modulators with a) external polarizer, b) on-chip polarizer.

writing technique to fabricate the passive part of the device. The metallization was fabricated by a conventional deposition and patterned with laser direct writing which formed three electrodes allowing an electric field to be applied within the waveguide core of both arms.

In order to test the device, we launched light into the input waveguide. The two outer electrodes were connected to ground and the central electrode was connected to a positive voltage. The application of a voltage across the two arms lead to the expected modulation of the amplitude. Figure 3c shows the transmission as a function of applied voltage, and demonstrates an extinction ratio of 15 dB and a V_π of 5 V.

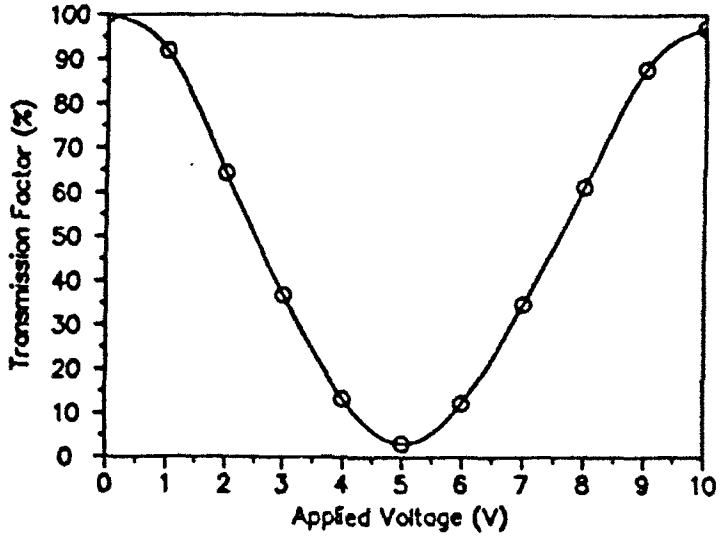

Figure 3c. Mach-Zehnder configuration.

The above results demonstrate the flexibility of our prototyping technique in fabricating a wide variety of active waveguiding structures useful for integrated optics. This work will be submitted for publication shortly, and is described further in the attached draft manuscript (Appendix B).

B. Integrated Optical Device and Circuit Modeling

In the final report of the previous contract, we described a project in which several simulation techniques that we had developed were being used in the development of a general

integrated optical device and circuit modeling package called B-PROP. This program will assist us, and other researchers in the field, in analyzing important problems in the design and fabrication of integrated structures. This work is being done in collaboration with Allied Signal.

During this period, we have completed the first two versions of this package, and have used it to study a number of problems. In particular, working with Allied we have explored the design of highly multimode star couplers for fabrication in polymer materials. In collaboration with H. Fetterman at UCLA, we have designed an optical delay line. Finally, we are currently using the program to assist our work on wavelength demultiplexers by considering the design of low divergence adiabatic tapers. Specific information on the delay line and star coupler projects is given in the following paragraphs.

In the optical delay line project, the goal is to take an optical signal at 1.3 μm, and split it 8 ways, with each arm having an optical path delay appropriate to operation of a 10 GHZ phased array radar system. This length, for GaAs, is about 300 μm. A sketch of the device is shown in Fig. 4. Several design goals need to be achieved. First, the y-branches must be asymmetric designs with splitting ratios from 12.5 - 50%. Second, low-loss large angle bends need to be produced to carry the signal to the outside of the chip where the detector arrays will be located. Finally, these functions need to be performed within the geometric constraints imposed by the 300 μm optical path delay requirement.

B-PROP was used first to examine asymmetric y-branches of the design shown in Fig. 5a. Power transfer as a function of the length of the tapering region is shown in Fig. 5b. As can be seen from the figure, power splitting in the required range is achievable. Next, a study of bends indicated that 5 mm radius of curvature would have negligible loss. Finally, all

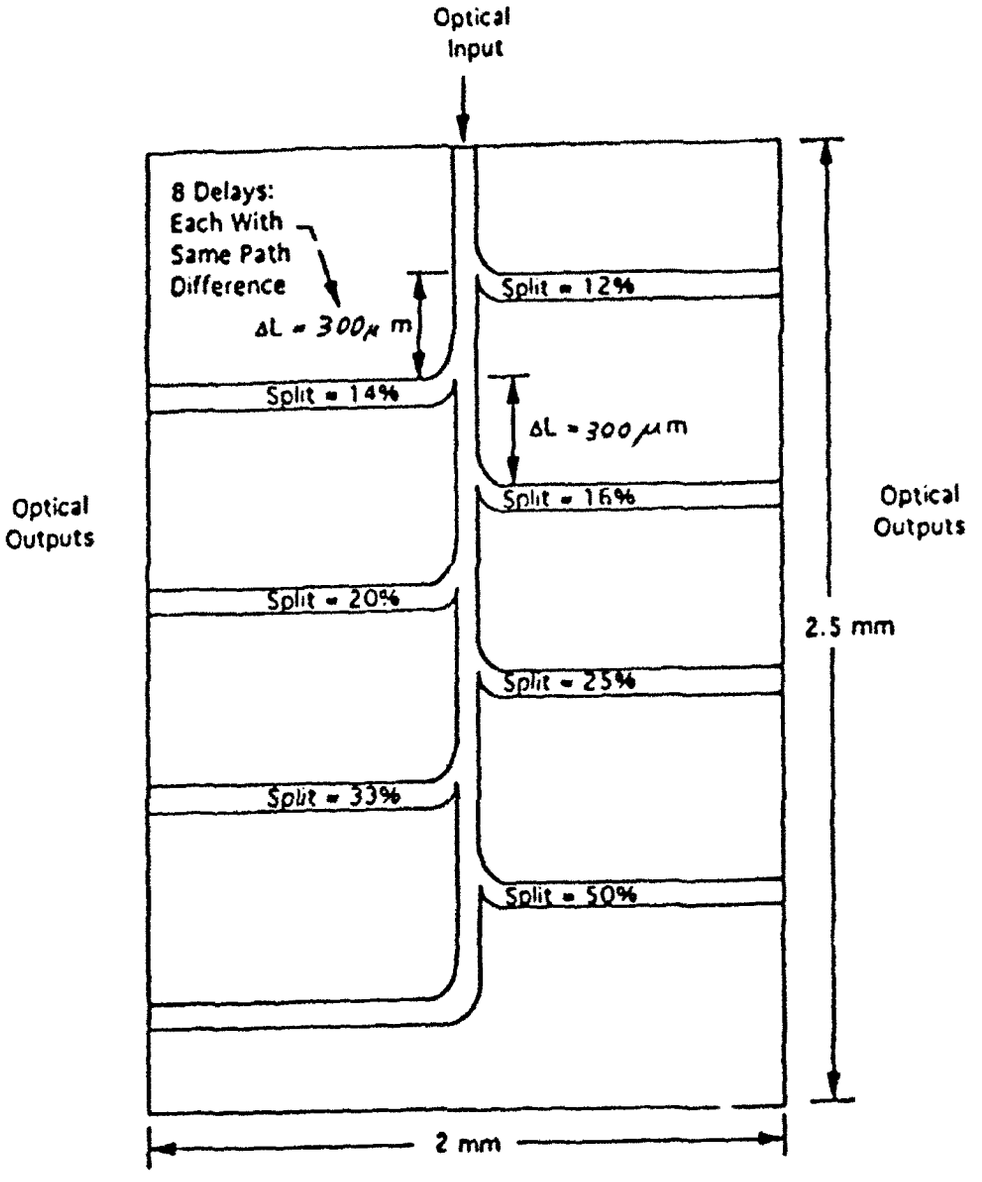

Figure 4. Sketch of optical delay line for use in phased array radar.

(a)

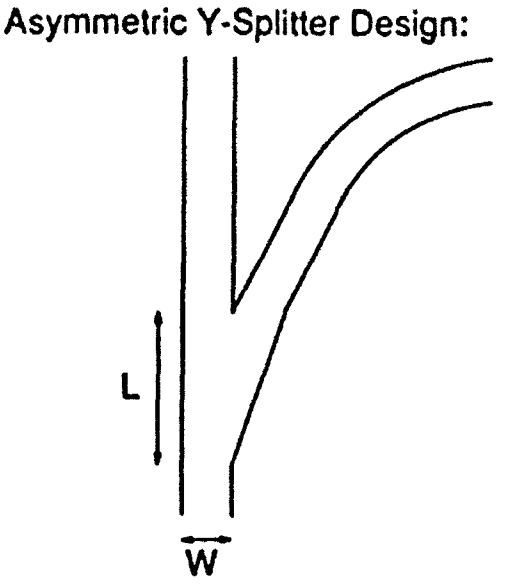

(b)

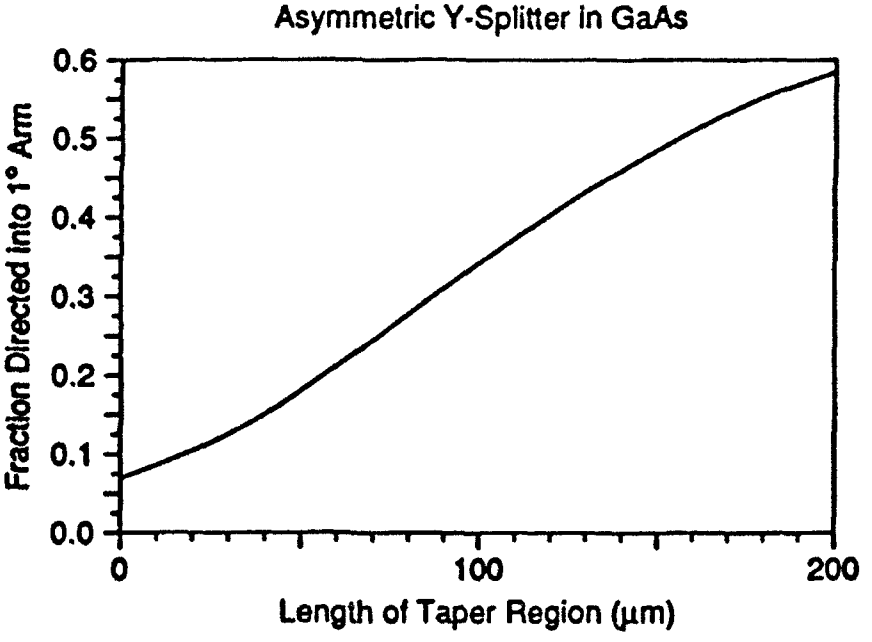

Figure 5. Asymmetric y-branch design and expected performances.

the components were put together in a 4-way optical delay line simulation of half of the actual 8-way device. A graph of the wave propagation in this structure is shown in Fig. 6. Fabrication of the device is currently underway using our prototyping technology.

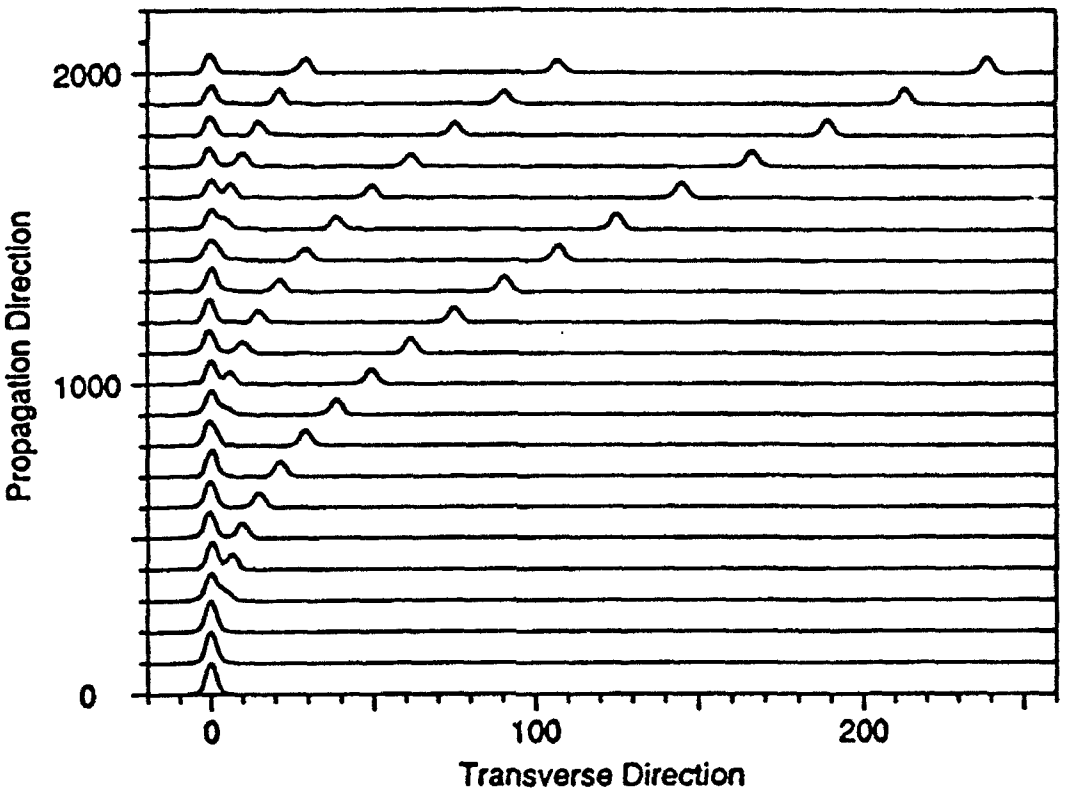

Figure 6. B-PROP simulation of propagation in optical delay line.

In the star coupler project, we are motivated by the industrial applications of multimode star couplers which are of interest to our collaborator, Allied Signal, and by the lack of published work in this area. Optical star couplers are widely used in lightwave local-area networks for even distribution of signals among several users. Configuration of a star coupler consists of an input and output array of waveguides connected by a wide slab waveguide. Star

couplers with single-mode waveguiding arrays are widely used and studied. However, due to limitations of multimode waveguiding in communication networks, multimode star couplers have been persistently neglected. Multimode star couplers are important for lightwave division in local subscriber systems for distributive services, star-based local area networks, and high-power splitting. In addition, multimode star couplers can be readily fabricated in polymers with the aid of various processing techniques.

Two arrays of multimode channel waveguides separated by a wide interaction region make the basic structure of the device. We have examined operational characteristics including intensity profiles as a function of device geometry, refractive index difference (or numerical aperture) and input profile. These calculations form the basis for constructing effective polymer waveguide devices and they extend the viability of finite difference beam propagation computational techniques into the realm of multimode structures.

The analysis of the devices was performed by utilizing the B-PROP program. To perform the simulations, we define multimode star coupler structures in a layout with N input and output waveguides having a symmetric step-index profile of width W. They are connected by an interaction region which is a waveguide of width N·W; input and output waveguides enter that region at various angles. Through the effective index method, channel waveguiding structures are represented in the simulation as slab waveguides. We launch a field distribution into one of the waveguides in the input array. The launched field distribution is comprised of a sum of all the modes supported by the input waveguide. The total signal power is equally split among the modes and the initial phase is chosen randomly. These conditions simulate the lightwave output of the previous device serving as a source for the star coupler, as each mode

propagates with different characteristic phase velocity.

The beam is propagated along the structure and the field distribution in the input waveguide, the interaction region, and the output waveguides is observed and the field intensity determined at the end of each output waveguide. Note that the resulting power distribution should ideally be uniform across the output array. Finally, the influence of several different parameters of device geometry, as well as the refractive index difference of the material, on the uniformity of the output intensity distribution was investigated.

Our simulation considers the operation of a multimode star coupler made in polymer material on a PMMA substrate. The widths of the waveguides in the arrays were varied between 50 and 200 μm and their refractive index was varied in the range from 1.50 - 1.581. The device was simulated for the wavelength of $\lambda = 838$ nm. The behavior of the device was studied as a function of the length of the interaction region for different number of modes supported by the input waveguide, keeping all other parameters fixed.

The number of modes was varied between 30 and 120 by first selecting different width of the input waveguides with the refractive index difference fixed and later changing the index difference with the width fixed. While in the most of the parametric studies, we examined the simplest case of the 2x2 star coupler first, in order to gain better understanding of the fundamental dependencies, our subsequent work considered 4x4 star couplers as well.

Figure 7a shows the computed field distribution in a 60-mode 4x4 star coupler. Note that the high spatial frequency present in the field distribution represent the large number of modes and their differing propagation velocities and random phases. The lightwave signal is launched in the left outermost input waveguide and it spreads in the structure establishing a particular field

intensity profile in all the four output waveguides. The relation between the power in output waveguides and length of the interaction region shown in Fig. 7b exhibits two different types of behavior, as seen on the graph. The first effect is a decay of power in the input waveguide

(a)

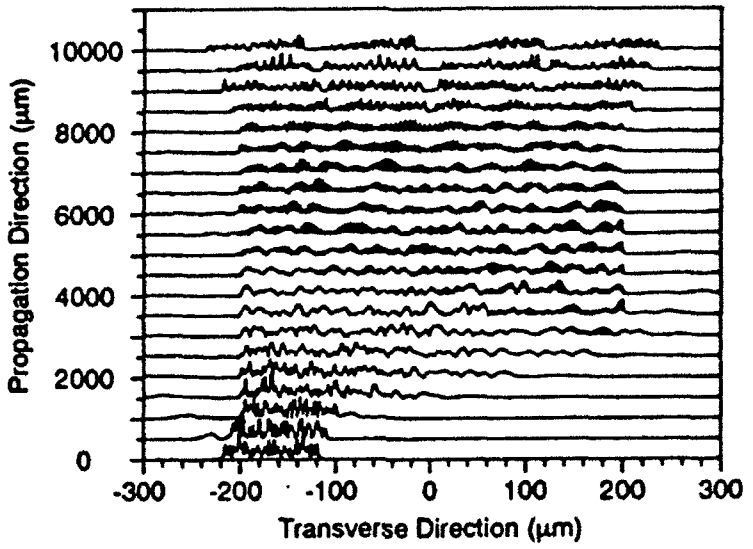

(b)

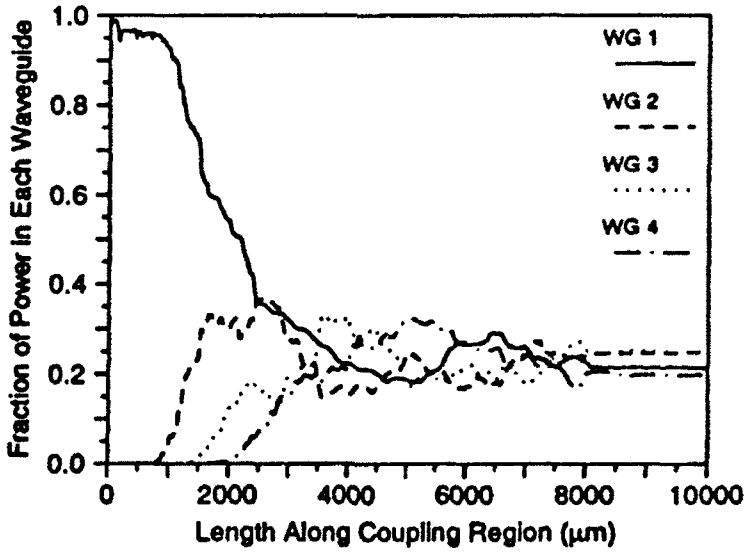

Figure 7. B-PROP simulation of 60-mode 4x4 star coupler in polymeric material.

and a rise of power being transferred into remaining waveguides. Later, power division among output waveguides fluctuates, reaching different values over the limited interval. The length of the interaction region necessary for the first uniform distribution is found to be inversely dependent on the insertion angle of the input waveguide. In addition, the level of fluctuations is observed to become narrower when a larger number of modes is supported by the structure. Thus we can determine the number of modes and required interaction length to achieve a certain level of output uniformity.

By varying several design parameters we obtained uniform power distribution among output waveguides. The required length of the interaction region of the device and the intensity difference among output waveguides can be controlled by adjusting the geometry of the input waveguides and increasing the number of modes supported.

C. Cryogenic Etching for Low-Damage, Sub-Micron Processing of MQWs

Under the last contract, we developed a dry etching process for GaAs and related compounds in which an excimer laser is used to activate a condensed layer of chlorine on the surface of the semiconductor, as well as remove etching products from the reaction area. The restriction of the reactive species to the surface, as well as the limitation of the product desorption to the illuminated area, yield an anisotropic etching without the need for highly energetic particle beams which damage sensitive MQW materials. In the initial work, the technique was well characterized in terms of process parameters. This work is described in previous reports and in Ref. 7. In addition, gold masks patterned by liftoff were used to demonstrate micron-scale patterning, and silicon nitride and silicon oxide were tested for

suitability as mask materials.

In the new contract, we have continued our work on this important technology by first demonstrating sub-micron patterning using e-beam patterned silicon-nitride masks. In addition, we have applied the technique to the fabrication of a quantum-well stripe laser. We have also performed measurements on Schottky devices fabricated on GaAs etched by our technique to demonstrate low damage. Finally, we have made several improvements to our apparatus and process. The above work is described in the following.

One of the ultimate goals of this project is to etch feature of submicrometer dimensions. The first step towards this goal is to find a suitable surface mask. The gold surface masks we have been working with up to now are unsuitable for high resolution applications because they often erode on the sides and because of the resolution limits of conventional lift-off lithography. The requirements for effective masking materials are resistance to the chlorine environment and excimer laser irradiation and the ability to be patterned to submicrometer dimensions.

For our studies of submicrometer etching, we used a Si_3N_4 mask patterned by electron beam lithography and reactive ion etching by Cornell University's National Nanofabrication Facility. The detailed results, along with some micrographs, are discussed in Ref. 8 (also found in Appendix B). Figure 8 shows the cross section of a feature etched on the GaAs (110) surface. We are able to etch features a half micrometer wide with aspect ratios of greater than one. A major finding is that the sidewall slope is independent of both the surface being etched and the orientation of the feature on the surface.

To test the suitability of this etching for device fabrication, we collaborated with Prof. Wen Wang's group at Columbia to apply our etching process to etch a mesa for a single

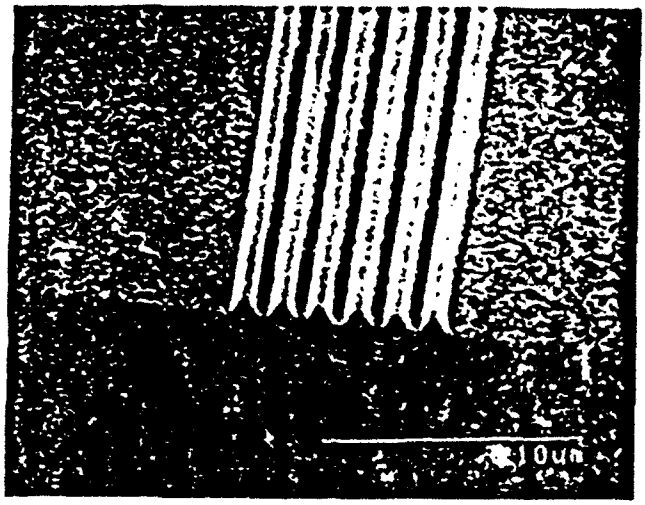

Figure 8. SEM of sub-micron features etched in GaAs using the low-damage cryogenic .

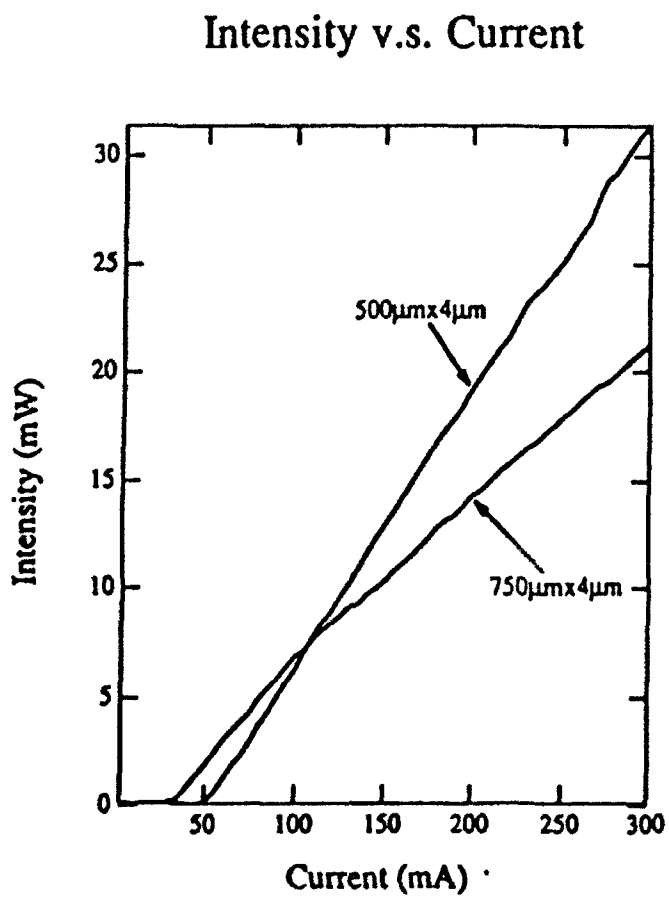

Figure 9. LI characteristic of a quantum well ridge laser etched using the low-damage cryogenic etching technique.

quantum-well ridge waveguide semiconductor laser. The structure of the laser and electron micrographs of the etched structure are in Ref. 8. Figure 9 shows the LI (light out-current in) characteristics of the laser. The performance of these lasers is comparable to that of lasers fabricated by wet etching. Since wet etching of II - V semiconductors is heavily dependent on crystallography and doping type and level, our low temperature etching process is more reliable for achieving micrometer scale structures. To complete this project, several technical challenges needed to be overcome. Most significant is the requirement for a uniform etch depth, which required that the excimer laser beam have a uniform intensity profile. This was accomplished through careful re-design of our optical beam delivery system.

A new etching chamber and load lock system, sketched in Figure 10, has been installed and tested during this period. The purpose of this apparatus is to accomplish sample transfer without exposing the etching chamber to the atmosphere. The new etching chamber is pumped by a turbo pump and during etching, the background pressure is about 10^{-7} Torr. The installation of the load lock system allows us to repeatedly do experiments without breaking the vacuum; as a result, we can obtain better surface morphology. We point out that a load lock system is important for low temperature etching processes, as many contaminants, such as moisture and residual etching products, tend to absorb on the sample surface at low temperatures.

We continued to explore effects of the addition of rare gases to the etching chamber, as described in the last report. The results for various rare gases are included in Figure 11. For the addition of Xe, Kr, and Ar, we saw an enhancement of the etch rate to about twice the normal etch rate with increasing rare gas partial pressure, and then a quenching of the etch rate

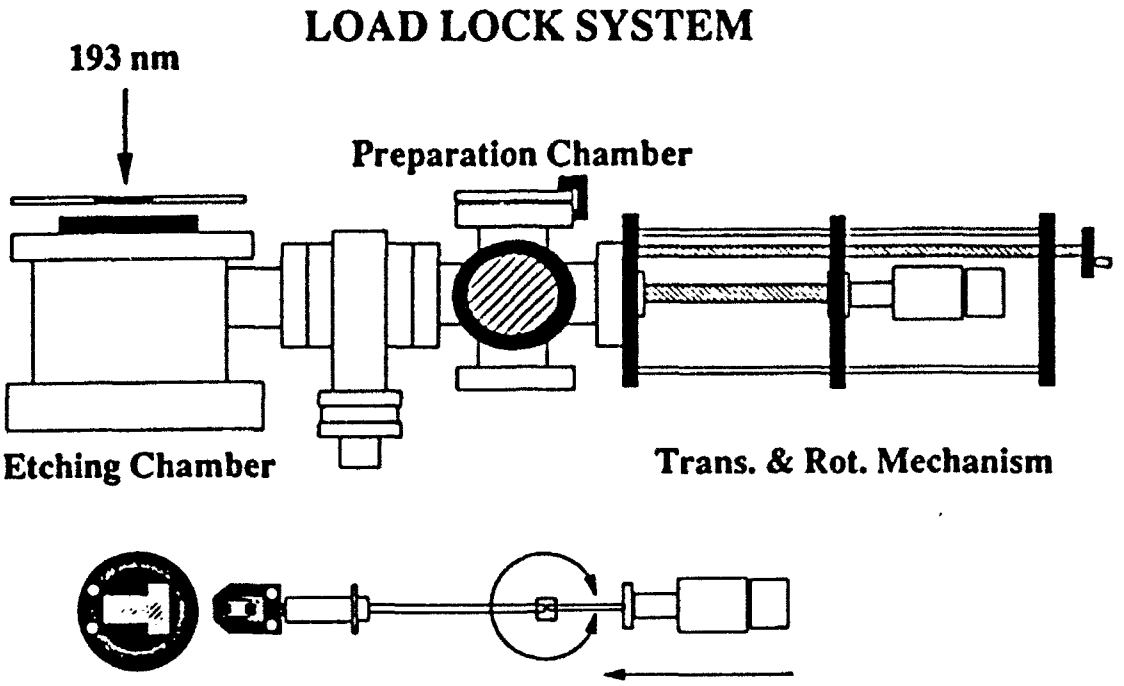

Figure 10. New vacuum chamber and load lock for cryogenic etching system.

with further addition of the rare gas. The addition of He or Ne causes no enhancement of the etch rate. Instead, they immediately cause a decrease in the etch rate. We suggest that the etch rate enhancement is attributable to a parallel channel for generating Cl atoms through the formation and decay of excited rare gas halide molecules. We have also found that the addition of rare gases results in a noticeable improvement of surface morphology.

D. Applications of Through-Wafer Via Etching

In the previous contract, we reported the development of a technique for rapid etching of through-wafer vias in SI-InP. In collaboration with Hughes, we had applied the technique

to the fabrication of vias in actual MMIC microwave devices. This work has been described in previous reports, and has been submitted for publication.

In this first period of the current contract, we have successfully transferred this technology to Hughes, and they are replicating our experimental setup in their labs. In addition, we have fabricated additional devices for microwave testing, which is currently underway. Results should be available in the coming months.

In addition, we have initiated a collaboration with Steve Forrest at Princeton to apply our etching technique to the fabrication issue in his "Smart Pixel" designs. Vias would be etched through SI-InP wafers to allow power connections between photocells on the back of the wafer to electronics on the front of the wafer. Work on this project is currently underway.

Finally, we have investigated a new application which uses our via etching process to fabricate large arrays of cylindrical vias which can act as transmission filters in the infrared. The filter consists of a series of cylindrical waveguides that are ~ 20 μm in diameter and ~ 100 μm in depth, with smooth straight sidewalls. The side walls must be highly conductive to avoid penetration of the waveguide mode into the walls.

The filter was formed from a 100 μm thick SI-InP Fe doped substrate. The pattern consists of a grid with ~ 20 μm laser etched through via holes, with 50 μm center-to-center spacing, as shown in Fig. 12. The entire pattern covers an area of 3 mm x 3 mm. The sample was mounted vertically in a quartz cell on a computer controlled X,Y,Z stage with an opening on the back. The opening allows the laser light to penetrate through the wafer onto a photodetector. This detector sends a voltage signal to the computer to shut off the beam, move to the next via location, and open the shutter to drill the next via. Thus the opening served as

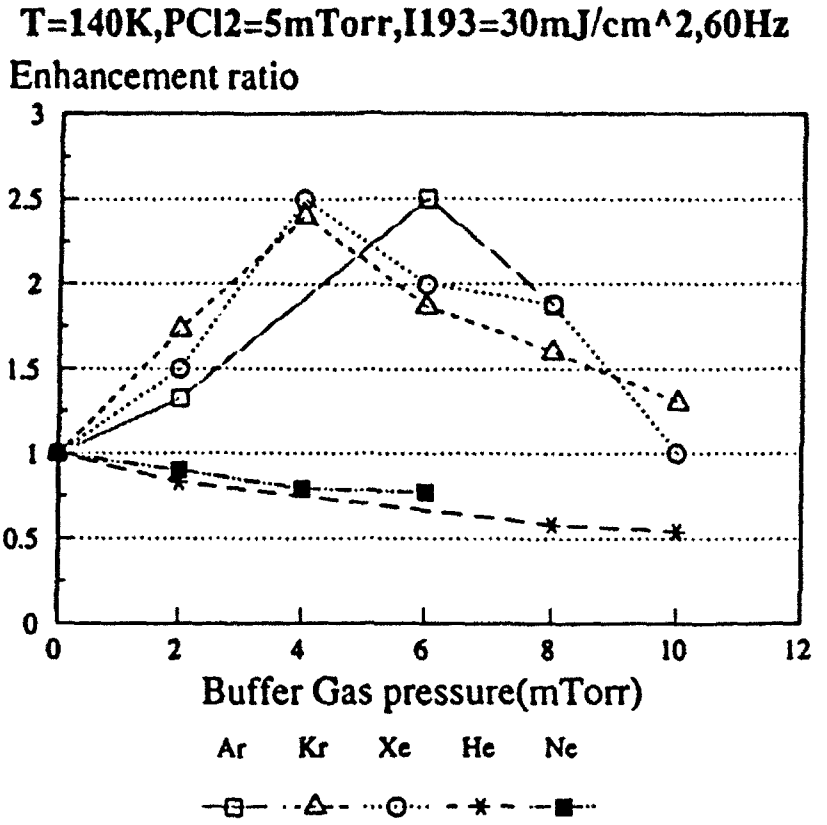

Figure 11. Effect of rare gas addition on cryogenic etch process.

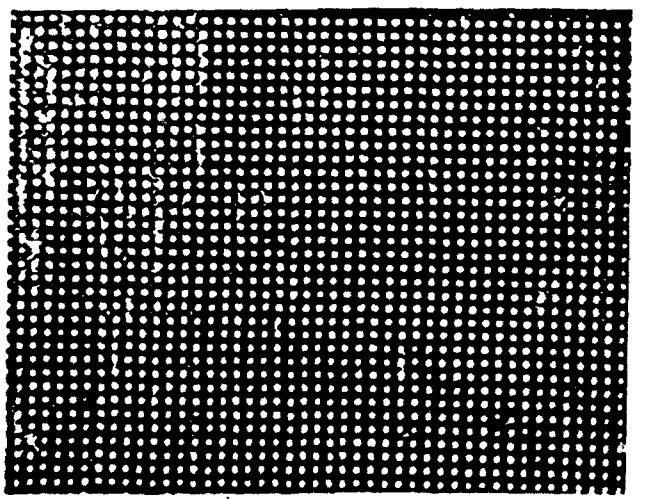

Figure 12. Optical photograph of an array of vias etched in SI-InP for use as an IR transmission filter.

an end-point detection. With this arrangement, the holes obtained were very uniform in diameter and etch time. The average via etch time was ~ 10 sec. After the etching, the sample was removed and rinsed in deionized water leaving the deeply etched through-holes clear as shown in Figure 12. The sample was then metallized Cr and Al using e-beam and thermal evaporation, respectively. The chromium and aluminum layers which covered the walls of the vias were ~ 200 Å and 7000 Å, respectively, resulting in highly conductive cylindrical waveguides.

The far-infrared transmission spectrum of this waveguide filter was measured using a Perkin Elmer spectrometer at 2 wavenumbers (cm^{-1}) resolution. A globar was used as the source and a DTGS bolometer as detector. Figure 13 shows the plot of the transmittance vs.

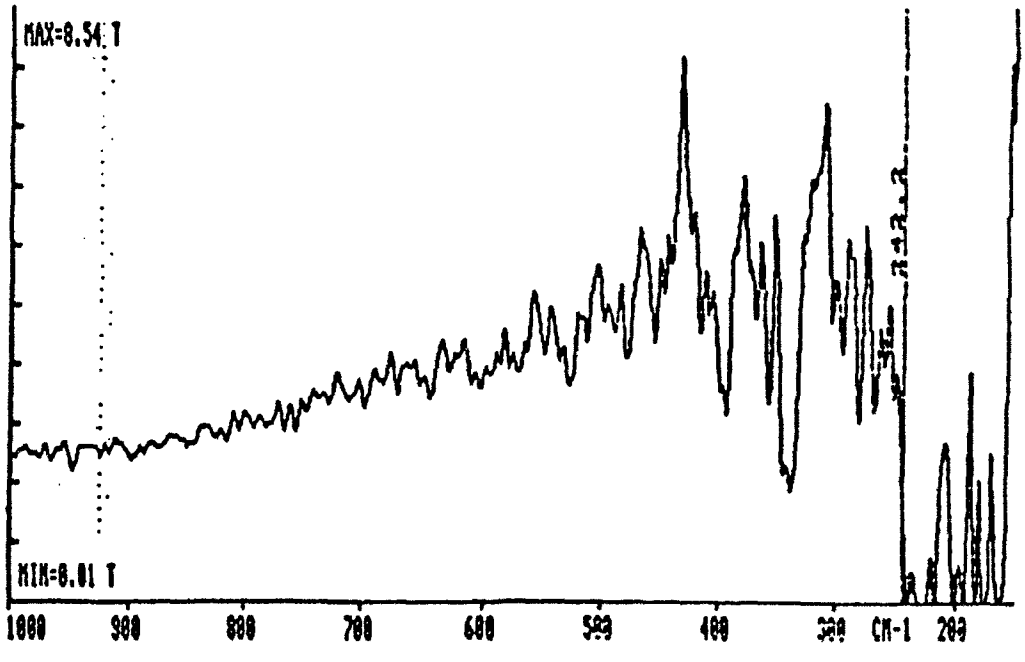

Figure 13. Transmittance vs wavenumbers for IR filter of Fig. 12.

wavenumbers. The position of the cutoff is at 242.2 cm^{-1} which corresponds to a cutoff wavelength of ~ 41 μm. The theory predicts that the cutoff wavelength is twice the diameter of the via hole. In our case the average diameter of the via is ~ 21 μm, implying a cutoff of 42 μm, in good agreement with the measurement. As shown in Fig. 13, the cutoff is very steep giving the filter a very high contrast.

E. Selective Vertical Etching of GaAs/AlGaAs MQW's

For the current contract, we proposed to explore a technique for controlled, vertical etching of multiple quantum-well structures, which could selectively remove different material layers. In the proposal we described initial work on a light-induced photoelectrochemical process for etching GaAs/AlGaAs, in which the shape of IV curves might be used to monitor the process.

During this first period of the current contract, we have completed our study of multilayer etching in GaAs/AlGaAs, and have obtained an understanding of the basic process physics. Furthermore, we showed that the changes in potential or current at the interface can be used to form an *in situ* process o. profiling diagnostic. This large body of work is described fully in the attached draft manuscript (Fink and Osgood, Appendix B), which has been submitted for publication in the J. Electrochem. Soc.

References

1. L. Eldada, M.N. Ruberto, R. Scarmozzino, M. Levy, and R.M. Osgood, Jr., J. Lightwave Tech. **10**, 1610 (1993).

2. L. Eldada, M.N. Ruberto, R. Scarmozzino, M. Levy, G. Scelsi, and R.M. Osgood, Jr., Technical Digest, Integrated Photonics Research Topical Meeting, New Orleans, LA, **10**, 336 (1992).

3. M. Levy, L. Eldada, R. Scarmozzino, and R. M. Osgood, Jr., IEEE Photon. Technol. Lett. **4**, 1378 (1992).

4. M. Levy, I. Ilić, R. Scarmozzino, and R. M. Osgood, Jr., "Thin-Film-Magnet Magneto-Optic Waveguide Isolator," submitted for publication in the IEEE Photon. Technol. Lett. (1992).

5. T. Cacouris, G. Scelsi, P. Shaw, R. Scarmozzino, R.M. Osgood, Jr., and R.R. Krchnavek, Appl. Phys. Lett. **52**, 1865 (1988).

6. N. Zhu, T. Cacouris, R. Scarmozzino, and R.M. Osgood, Jr., J. Vac. Sci. Technol. B **10**, 1167 (1992).

7. M.C. Shih, M.B. Freiler, G. Haase, R. Scarmozzino, and R.M. Osgood, Jr., Appl. Phys. Lett. **61**, 828 (1992).

8. M.B. Freiler, M.C. Shih, R. Scarmozzino and R.M. Osgood, Jr., Mats. Res. Soc. Symp. Proc., Fall Meeting, Boston, MA, (1992).

Presentations to Industry and Symposia
July 15, 1992 - February 14, 1993

1. Z. Lu and R.M. Osgood, Jr., "*In Situ* Surface Oxidation, Cleaning and Passivation of GaAs and GaSb using a Microwave Electron-Cyclotron-Resonance (ECR) Plasma Source," Gordon Conference, New Hampshire, August 10-14 (1992).

2. M.B. Freiler, M.C. Shih, R. Scarmozzino and R.M. Osgood, Jr., "Excimer Laser Driven Cryoetching of GaAs and Related Compounds," presented at the Gordon Research Conference, Meriden, NH, July 27-31, (1992).

3. T. Fink and R.M. Osgood, Jr., "Photoelectrochemical Etching of GaAs/AlGaAs Multilayer Structures," (invited talk) University of California at Santa Barbara, September 16, (1992).

4. M.C. Shih, M.B. Freiler, R. Scarmozzino and R.M. Osgood, Jr., "Cryogenic Etching of GaAs Activated by Excimer Laser Radiation of Physisorbed Chlorine," AVS Symposium, Chicago, IL, November 9-13, (1992).

5. M.B. Freiler, M.C. Shih, R. Scarmozzino and R.M. Osgood, Jr., "Excimer Laser Induced Cryoetching of GaAs and Related Materials," Mats. Res. Soc. Symp., Fall Meeting, Boston, MA, November 30-December 4, (1992).

6. M. Levy, L. Eldada, R. Scarmozzino and R.M. Osgood, Jr., "Fabrication of Narrow-Band Channel-Dropping Filters," submitted to the Optical Fiber Conference, OFC '93, San Jose, CA, February, (1993).

Publications
July 15, 1992 - February 14, 1993

1. T. Fink and R.M. Osgood, Jr., "Photoelectrochemical Etching of GaAs/AlGaAs Multilayer Structures," submitted for publication in the J. Electrochem. Soc. (August 14, 1992).

2. M. Levy, L. Eldada, R. Scarmozzino, and R. M. Osgood, Jr., "Fabrication of Narrow-Band Channel-Dropping Filters," IEEE Photon. Technol. Lett. **4**, 1378 (1992).

3. M. Levy, I. Ilić, R. Scarmozzino, and R. M. Osgood, Jr., "Thin-Film-Magnet Magneto-Optic Waveguide Isolator," accepted for publication in the IEEE Photon. Technol. Lett. (1992).

4. T. Fink and R.M. Osgood, Jr., "Light-Induced Selective Etching of GaAs in AlGaAs/GaAs Heterostructures," accepted for publication in the J. Electrochem. Soc. (1993).

5. O. Ghandour, R. Scarmozzino and R.M. Osgood, Jr., "Laser-Assisted InP Via Etching for Microwave Device Applications," submitted for publication in the IEEE Transactions on Semiconductor Manufacturing (October 6, 1992).

6. B. MacDonald, C. Guest, M. Freiler, R. Scarmozzino, A. Smith and R. Hunter Jr., and R.M. Osgood, Jr., "Efficient Multiple Via Etching of Polyimide Films Using Fresnel Phase Zone Plate Arrays," submitted for publication in the Appl. Opt. (November 23, 1992).

7. L. Eldada, M.N. Ruberto, R. Scarmozzino, M. Levy, and R.M. Osgood, Jr., "Laser-Fabricated Low-Loss Single-Mode Waveguiding Devices in GaAs," **10**, 1610 (1993).

Work Statement APPENDIX A

1. SELECTIVE PROCESSING FOR QUANTUM DEVICES

- Cryogenic Etching of III-V Materials for MQW's
  - Extension of current technique to submicrometer patterns.
  - Etching of bulk AlGaAs, GaSb, InAs, and AlSb.
  - Examination of heterostructure etching.
  - Application of process to MQW material and devices.
- Photoelectrochemical Etching
  - Use of electrochemical techniques to monitor layer by layer removal of QW material for selective processing of MQW structures.
  - Demonstration of etching of two-height quantum-well array.

2. INTEGRATED OPTICS AND PHOTONIC STRUCTURES

- Development of Photonic Circuit Elements Fabricated by Selective Processing.
  - Modulating and Switching Devices: Mach-Zender interferometric amplitude modulator and directional-coupler-based 2 x 2 switch.
  - Wavelength Selective Devices: Wavelength demultiplexer and narrow-band channel dropping filter.
  - Integrated Magnetic Optical Isolator.
- Application to Integrated Optical Switching Arrays: Demonstration of 4 x 4 switch.
- Theoretical modeling of photonic devices and circuit elements.

Laser-Fabricated Low-Loss Single-Mode Waveguiding Devices in GaAs

Louay Eldada, *Member, IEEE*, Mark N. Ruberto, *Member, IEEE*, Robert Scarmozzino, Miguel Levy, and Richard M. Osgood, Jr., *Senior Member, IEEE*

***Abstract*—We have used a maskless laser etching technique to fabricate novel waveguides and waveguiding structures directly into the surface of GaAs/AlGaAs heterostructures. The modal and loss properties of these groove-defined structures have been measured as a function of waveguide geometry, and low-loss single-mode waveguides have been produced. Using the technique, we have fabricated various passive optical devices in a single processing step. Waveguide bend and branch losses have been measured and are comparable to those in conventionally fabricated devices. Experimental results are described by simple theoretical models. The technique is attractive as a prototyping tool for developing and testing new integrated optic circuits.**

I. Introduction

RECENTLY, we have developed a new technique for direct-writing of optical waveguide devices in semiconductor surfaces [1], [2]. The process uses a focused laser beam to photoelectrochemically etch micrometer-scale grooves in GaAs/AlGaAs heterostructures, thereby patterning rib-like optical waveguide structures. The technique does not require the use of a mask; thus, the etching can be done in a single step. In conjunction with computer-controlled scanning of the optical beam, the technique can be used as a prototyping tool for developing and testing new integrated optic circuits. In addition, its ability to contour easily the lateral and longitudinal effective index profile offers the potential for fabricating novel integrated optic devices [3]. The technique is capable of patterning low-density features with long lineal dimensions over comparatively large planar areas, for application to both optical packaging and integrated optic circuits. This capability is matched to the requirements of arrays of waveguides and switches, typical of switching fabrics, arranged over areas which are large, e.g., ~10–100 cm^2, in comparison to those characteristic of IC die. In this connection we note that writing techniques have been reported to be useful for semiconductor [1], [2] polymeric, [4]–[6], and $LiNbO_3$ [7] waveguides.

However, before writing of prototype circuits can be made possible, it is necessary to demonstrate that low-loss, single-mode waveguides can be written on low-loss substrates. Further, it is necessary to be able to write the "building-block" structures or basic passive devices which are necessary to route light across the surface and into electro-optic switches. In addition, these devices should have predictable characteristics, describable by an appropriate elecromagnetic model.

Manuscript received January 21, 1992; revised June 1, 1992.

The authors are with Microelectronics Sciences Laboratory, Columbia University, New York, NY 10027.

IEEE Log Number 9203419.

In this paper, we present experiments which demonstrate the writing of high quality optical waveguides on GaAs/AlGaAs substrates. In addition, we demonstrate that low loss bends and branches can be made repeatably. The appropriate analytical models for predicting the performance of these passive devices are also described.

II. Laser Fabrication of Rib-Like Waveguides

The experimental procedure and physical mechanism for laser-induced photoelectrochemical etching have been described in detail elsewhere [8]. Briefly, a laser beam is focused onto a GaAs/AlGaAs heterostructure sample, which is immersed in a thin overlying film of electrolyte and contained in a quartz cell. The focused radiation generates electron-hole pairs near the semiconductor surface, and the holes are transported to the interface leading to the anodic dissolution of the semiconductor in the vicinity of the laser spot. The *resolution* of the process is determined by the optical beam size and by the transport of the minority carriers in the semiconductor. By scanning the laser beam over the sample via computer-controlled translation stages, micrometer-scale trenches can be formed in the GaAs layer in any desired pattern. For most experiments, the laser wavelength was 275 nm; the laser spot size was about 2 μm (full width at 1/e intensity); the etchant was $HCl:HNO_3:H_2O::4:1:50$; and the substrate was a vertically single-mode waveguide structure consisting of a 1.3-μm layer of n-GaAs on a 2.7-μm layer of n-$Al_{0.1}Ga_{0.9}As$. For all experiments, the IR light was TE-polarized, and the wavelength used was 1.3 μm, at which $n_{GaAs} = 3.4049$ and $n_{AlGaAs} = 3.3566$.

In the GaAs/AlGaAs heterostructure, IR light is confined vertically within the higher refractive index GaAs layer. By etching two grooves partway through the GaAs layer as shown in Fig. 1, light is confined in the region between the grooves by virtue of the greater effective index in the unetched region compared to the etched region [1], [2], as in a conventional rib or ridge waveguide. Note that this trench-defined waveguide geometry differs from the geometry used in many other reports of laser-written waveguides.

An important consideration in device fabrication with this new technology is to have sufficient control of processing to build useful devices. For example, in order to allow flexible design of single-mode waveguides and the optoelectronic devices based on them, it is necessary to have sufficiently high resolution to allow close positioning of the trenches. This requirement presents a potentially serious problem since

Fig. 1. SEM photograph of a single-mode waveguide etched in GaAs/AlGaAs (10^{16} cm^{-3}).

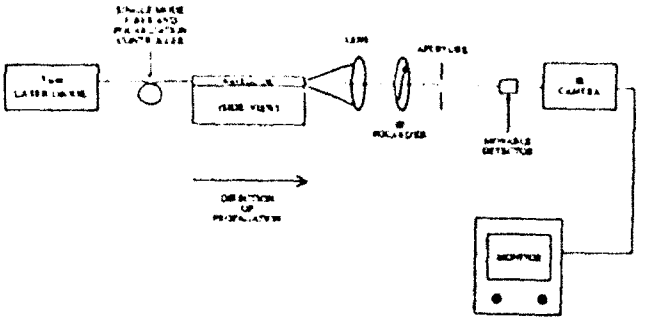

Fig. 2. Schematic diagram of waveguide characterization setup.

for waveguide applications free-carrier absorption limits the doping to low values ($\leq 10^{16}$ cm^{-3}). This low doping level results in a long diffusion length for carriers in the solid (≥ 7 μm), thus making it difficult to obtain high resolution. In connection with our waveguide device research, we have studied electrochemical factors which influence the resolution of our process [9] and have been able to obtain high resolution at low doping, as demonstrated in Fig. 1. This result was achieved through the discovery of appropriate electrolytes which have sufficiently high chemical reaction rates without the use of an applied bias. The latter point is significant since the ability to perform electroless etching using these electrolytes greatly simplifies the fabrication process. Waveguides have been etched in heterostructure material doped as low as 10^{14} cm^{-3}, which is important for fabrication of electro-optic devices in which the depletion width must be sufficiently large to allow penetration of the electric field into the region of the optical mode.

III. Waveguide Characteristics

Rib-like waveguides were fabricated as described above, and their modal and loss properties were measured as a function of geometric parameters. The basic characteristics of these unconventional groove-defined waveguides can be described by simple analytical models using appropriate effective waveguide dimensions as will be shown in the following.

In order to perform the waveguide measurements, the 1.3-μm light of a laser diode was directed through a polarization maintaining fiber, whose cleaved output facet was butt-coupled to one of the cleaved ends of our samples. The lightwave output from the other end of the device was imaged onto an IR camera using a microscope objective. Thus, the intensity pattern could be viewed on a TV monitor. A schematic diagram of the waveguide characterization setup is shown in Fig. 2. By displacing the fiber so as to launch light asymmetrically into the waveguide, higher order modes, if present, would be excited, and appear as multiple lobes on the monitor. Fig. 3 shows optical photographs of two such intensity patterns for waveguides with different trench separations. In the first example, with a trench separation of 6 μm, only one central bright spot can be observed, demonstrating single-mode operation. For the second case, with a somewhat larger separation of 10 μm, two intense lobes can be seen, indicating multimode behavior.

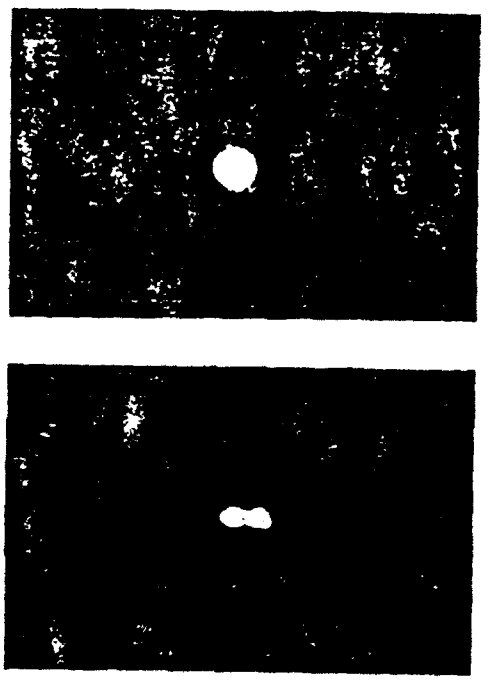

Fig. 3. Optical photographs of waveguide output intensity patterns illustrating single-mode (upper) and multimode (lower) behavior. The trench separation was 6 μm for the single-mode guide and 10 μm for the multi-mode guide. In both cases, the trench depth was 0.65 μm.

In order to analyze more quantitatively the modal properties of these structures, several waveguides were fabricated with different trench depths and trench separations, and were classified as single-mode or multimode according to the number of lobes observed in the imaged intensity pattern. The results are shown in Fig. 4. Here, the effective waveguide width is defined by the trench separation minus the trench width, and corresponds to the approximate width of the flat portion of the rib (see Fig. 1 and the inset to Fig. 6). For shallow trench depth or small trench separation (yielding small effective waveguide width), single-mode operation is achieved. Also plotted in the same figure is the theoretical single-mode/multimode boundary

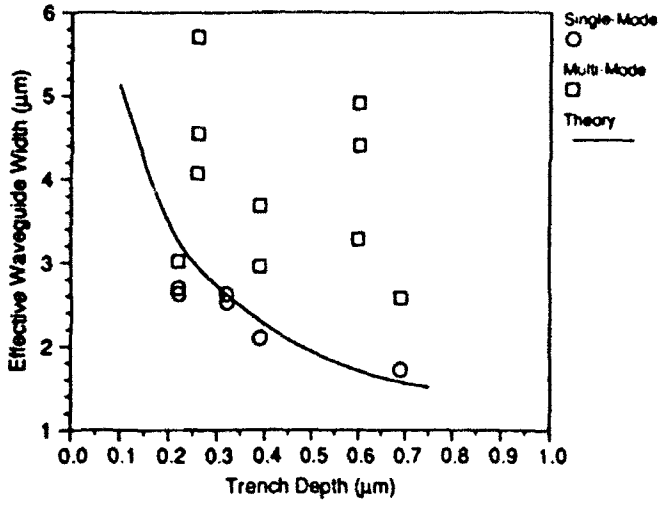

Fig. 4. Modal characteristics for waveguides fabricated with different etch depth and trench separation. The solid curve represents the theoretical single-mode/multimode boundary calculated as described in the text.

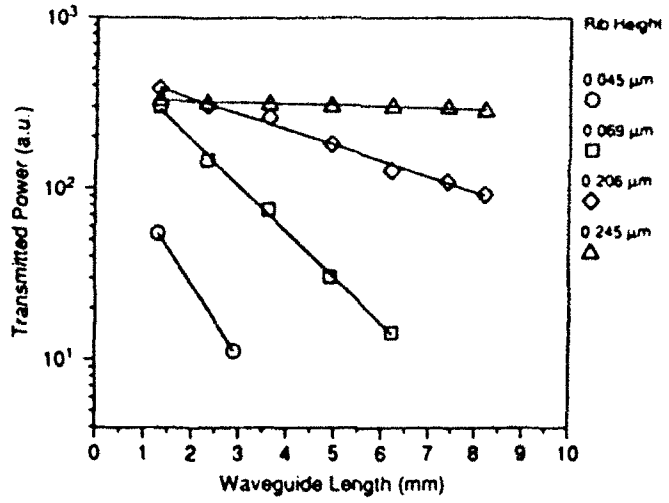

Fig. 5. Waveguide transmission versus length obtained by the cutback method. The graph shows data for waveguides at various laser powers yielding different etch depths. The trench separation was fixed at 7 μm.

curve obtained from the following inequality:

$$w_g < \frac{\lambda}{2} \frac{1}{\sqrt{N_{eff}(0)^2 - N_{eff}(d)^2}} \quad \text{for single mode.} \quad (1)$$

Here λ is the wavelength of the light, w_g is the effective width of the waveguide, $N_{eff}(l)$ is the effective index of the original slab waveguide etched to depth l, and d is the trench depth. This relation is obtained using effective index theory to reduce the two-dimensional waveguide cross section to that of a one-dimensional slab waveguide in the lateral direction, in which the effective index N_{eff} is a function of the local etch depth [10]. The usual dispersion relation for a symmetric slab waveguide is then used to obtain the above expression. The figure shows that this approximate theory gives a good description of the modal properties of our waveguides and is thus a useful criterion for designing new waveguide structures.

From the previous result, we find that for all but the deepest trenches, a trench separation of 6–8 μm generally yields a single-mode guide. Therefore, the trench separation was fixed at 7 μm, and several guides of different trench depths were fabricated in order to determine the waveguide loss versus etch depth for single-mode guides. To measure the loss, the IR camera in the previous setup was replaced with a photodetector. By using the cutback method, we obtained the power transmitted by the waveguide as a function of waveguide length. This was done for several laser etching powers, yielding different trench depths. The results are shown in Fig. 5, with rib height as a parameter. The rib height is defined as the thickness of the GaAs waveguiding layer in the core minus the thickness of that layer in the etched trench. As the laser power is increased, yielding deeper trenches, the light is better confined.

The slopes in Fig. 5 give the loss coefficient of the waveguides. This value is plotted in Fig. 6 as a function of the rib height. As the rib height is increased to about 0.25 μm, the waveguide loss decreases and eventually reaches a value of 0.9 dB/cm, which is a suitably low value for integrated optics

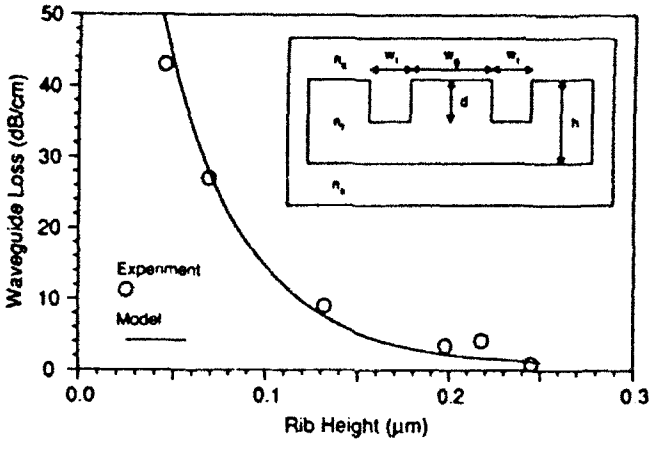

Fig. 6. Waveguide loss versus rib height obtained from the data shown in Fig. 5. The solid curve is the result of a model which includes radiation and scattering loss as described in the text. In computing the radiation loss, values of $w_g = 4$ μm and $w_t = 4$ μm were used. The scattering loss was estimated at 0.6 dB/cm, corresponding to a surface roughness of about 6 nm. The inset shows the idealized waveguide geometry assumed for the calculation.

applications. Also plotted in Fig. 6 is the calculated result from a theoretical model for estimating the loss in these waveguides. In constructing this model, which is described in the next few paragraphs, we have assumed an idealized geometry for the waveguide structure, as shown in the inset of Fig. 6.

For shallow trenches, the loss is dominated by radiation due to light tunneling through the finite-width etched region and propagating laterally into the exterior of the guide, while for sufficiently deep or wide trenches, the loss is limited by scattering due to surface roughness at the air/GaAs interface. Previous analysis yields the following approximate expression for the radiation loss coefficient [10]:

$$\alpha_r = \frac{8\kappa^3\gamma^3}{\beta(1+\gamma w_g/2)(\kappa^2+\gamma^2)^2} \exp(-2\gamma w_t). \quad (2)$$

Here, w_g is the effective width of the guide, w_t is the effective width of the trench, β and κ are the longitudinal and transverse propagation constants, and γ is the transverse decay constant. These propagation constants are computed using effective index theory as described earlier. Note that the above expression is valid for $\exp(-\gamma w_t) \ll 1$.

In computing the scattering loss it is necessary to consider potential contributions related to both vertical and lateral confinement. For our waveguides, simple estimates show that the vertical scattering loss dominates. This is essentially due to the fact that the index difference at the air/GaAs interface, which confines the light vertically, is much larger than the effective index difference between the etched and unetched regions, which produces lateral confinement. The calculation of the vertical scattering loss is complicated by the fact that at the air/GaAs interface, portions of the wave near the center of the guide see a surface roughness which is different from that near the etched trenches. The scattering loss is thus estimated from an effective average surface roughness σ using the following well-known expression [11]:

$$\alpha_s = 2n_f^2 k^2 \sigma^2 \frac{\cos^3\theta/\sin\theta}{h + 1/\gamma + 1/\delta}. \tag{3}$$

Here, γ and δ are the decay constants in air and AlGaAs, respectively, h is the thickness of the GaAs slab, n_f is its refractive index, and $\sin\theta \equiv N_{\text{eff}}(0)/n_f$.

In Fig. 6 we plot the sum of the radiation loss, which is a function of rib height through the effective index, and an estimate of the scattering loss. The scattering loss was calculated as 0.6 dB/cm, corresponding to a surface roughness of about 6 nm. As can be seen in the figure, the agreement between theory and experiment is quite good. Furthermore, from the expression for α_r, we can see that a wider etched region (larger w_t) should yield lower radiation loss. Therefore, waveguides were fabricated using pairs of trenches (separated by 2 μm) on either side of the rib in order to create a wider etched region. The loss for such dual-trench waveguides was found to be reduced to only 0.6 dB/cm, in agreement with the trend predicted above. Note that an alternative means of creating the wider etched region might be to use appropriate optics to form a broader, rectangularly shaped beam profile. Any further attempts to reduce the waveguide distributed loss would probably be limited by scattering at the air/GaAs interface; thus the deposition of a higher index overlayer on the GaAs would be expected to be important to further reduce losses.

IV. Passive Waveguiding Devices

A. Basic Passive Structures

The need to direct light between various components of an optical circuit requires several passive waveguiding structures including tapers, bends, and branches. Due to the maskless nature of our processing technique, such structures can be conveniently fabricated by simply feeding the desired patterns into the software controlling the apparatus. Several passive waveguiding devices were etched in this manner and are shown in Fig. 7. Note that when etching such structures, which are composed of many connected line segments, we have found that it is important to avoid stops and starts at the various line joins which would cause double etching, and deteriorate device performance. Therefore it was necessary to develop our control system so that it would continuously scan one axis, while appropriately stepping or varying the velocity of the other axis to achieve the desired pattern.

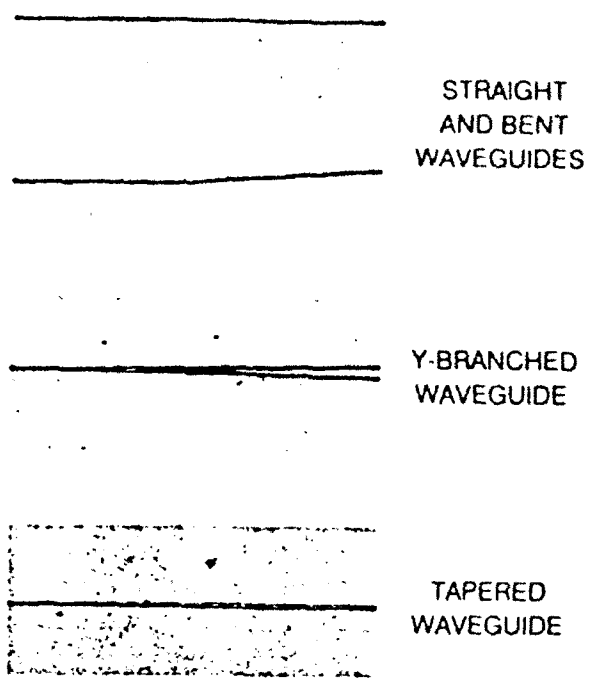

Fig. 7. Optical photographs illustrating various passive waveguiding devices fabricated masklessly using laser etching.

Waveguide bend and branch losses were measured as a function of the relevant angle. This measurement was performed by detecting the output of each device and normalizing to the output of a straight waveguide fabricated on the same sample under the same etching conditions. This normalization removes any coupling, radiation, or other losses that are present, and yields only the loss of each geometric transition. The results are shown in Figs. 8 and 9, in which transmission is plotted as a function of device angle. In both figures we observe the expected behavior, namely for shallow angles, most of the light is transmitted, while for higher angles, losses become significant. For bends and branches, the losses are less than 1 dB for angles less than 2°. Furthermore, the average splitting ratio for Y-branches was found to be 48/52. Thus the performance of these devices is comparable to that seen in structures fabricated by conventional means.[12]

Note that the Y-branch results shown in Fig. 9 are not for the simple design pictured in Fig. 7, and shown schematically in Fig. 10(a). When Y-branches were etched in that fashion, the branch region became distorted during the etch process at the inner "V" point due to the double etching at the tip of the "V" where the trenches overlap. This distortion was especially significant for shallow angles. The effect of the double etching was the narrowing of the waveguiding regions in the vicinity

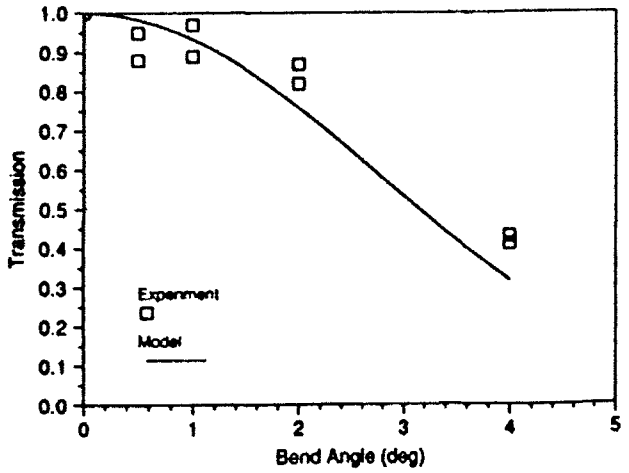

Fig. 8. Waveguide bend transmission versus bend angle. The solid curve is the result of a model based on computing the overlap of modes with tilted wavefronts as described in the text. The parameters used in the calculation were $w_g = 4$ μm and $d = 0.75$ μm.

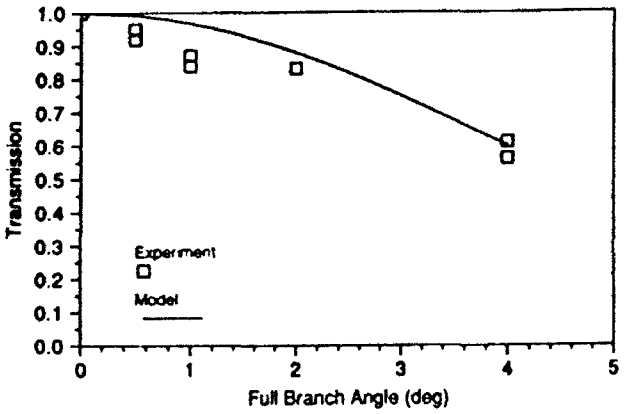

Fig. 9. Waveguide Y-branch transmission versus full branch angle. The solid curve is the result of a model based on computing the overlap of modes with tilted wavefronts as described in the text. The parameters used in the calculation were $w_g = 4.5$ μm and $d = 0.15$ μm.

of the overlap, which induced additional losses. In order to circumvent this problem, an alternate approach was taken. We started etching the trenches of the "V" further forward toward the point where the separation between their centers was equal to the trench width; in this case the edges of the trenches barely touch. This design, shown schematically in Fig. 10(b), resulted in lower losses as expected. However, this approach suffered from another problem. Since the two branch arms were separated by some distance, the overlap with the central part of the incident waveguide mode was poor, resulting in losses which were not as low as desired. To obtain further improvement in Y-branch performance, a "tail" was added to the branch region in order to more effectively split the mode before the actual branching region. This design, shown schematically in Fig. 10(c), reduced the losses even more, and was used for the data in Fig. 9.

The general behavior seen in Figs. 8 and 9 can, in fact, be modeled through approximate analytical expressions. By

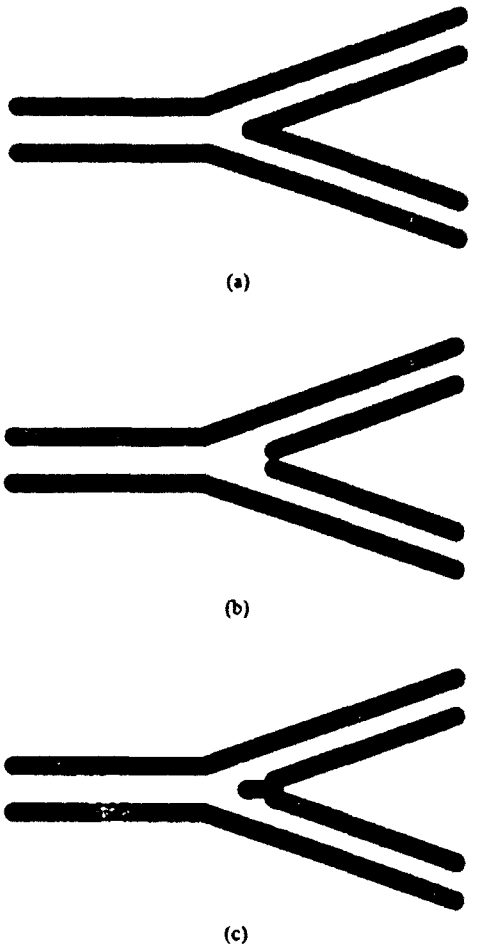

Fig. 10. Schematic diagram of different Y-branch designs studied.

computing the overlap integral between the incident field and the transmitted field with a tilted wavefront, one can obtain the transmitted power as $|t|^2$ where t is the transmission coefficient. For bends, the incident and transmitted fields are

$$E_i(x) = \begin{cases} \cos(\kappa x) & |x| \le a \\ \cos(\kappa a)\exp[-\gamma(|x| - a)] & |x| \ge a \end{cases} \quad (4)$$

$$E_t(x) = E_i(x)e^{-i\beta x \sin\alpha}. \quad (5)$$

Here, β, κ, and γ are as previously defined, $2a \equiv w_g$, and α is the bend angle. The transmission coefficient t is given by

$$t = \frac{\int_{-\infty}^{\infty} E_i \cdot E_t^* dx}{\sqrt{\int_{-\infty}^{\infty} |E_i|^2 dx \cdot \int_{-\infty}^{\infty} |E_t|^2 dx}} = \frac{\gamma}{1+\gamma a}\int_{-\infty}^{\infty} E_i \cdot E_t^* dx. \quad (6)$$

Performing the integration yields the following expression for the bend transmission:

$$t = \frac{1}{1+\frac{1}{\gamma a}}\left\{\operatorname{sinc}(qa) + \frac{1}{2}\operatorname{sinc}[(2\kappa+q)a] + \frac{1}{2}\operatorname{sinc}[(2\kappa-q)a] + 2\frac{\cos^2\kappa a}{(4\gamma^2+q^2)a}(2\gamma\cos\kappa a - q\sin qa)\right\}. \quad (7)$$

Here $q \equiv \beta\sin\alpha$ and $\operatorname{sinc}(x) \equiv \sin(x)/x$. Similar analysis

Fig. 11. A compact directional coupler fabricated masklessly using laser etching. The device is formed from two parallel waveguides defined by two deep outer trenches and one shallow common trench. The coupling coefficient is controlled by the depth of the central common trench.

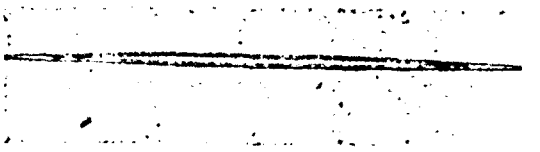

Fig. 12. A passive Mach–Zehnder interferometer device fabricated masklessly using laser etching.

yields the following result for Y-branches [13]:

$$t = \frac{e^{iqa/2}}{1+\frac{1}{2\alpha}}\left\{\operatorname{sinc}\left(\frac{qa}{2}\right) + \frac{1}{2}e^{ika}\operatorname{sinc}\left[(2\kappa+q)\frac{a}{2}\right] - \frac{1}{2}e^{-ika}\operatorname{sinc}\left[(2\kappa-q)\frac{a}{2}\right] + 2e^{iqa/2}\frac{\cos^2\kappa a}{(2\gamma-iq)a}\right\}. \tag{8}$$

Here, the variables are as described above except that α is the half-angle of the branch, and the waveguide parameters β, κ, and γ are for a guide with twice the width of the Y-branch arms. These expressions are plotted in Figs. 8 and 9 along with the experimental data. This model agrees well with the experiment for the range of angles used.

B. Additional Passive Devices

The basic passive structures described above have been used as building blocks to fabricate more complicated passive devices. For example, it is possible to form a waveguide coupler by aligning two waveguides adjacent to each other and using only a single central trench. In this device, coupling can be conveniently varied by adjusting the depth of the central groove over a specific interaction length along the waveguide axis. This approach permits a more compact coupling geometry than is possible with designs based on waveguide separation. Such a coupler is shown in Fig. 11.

In addition, Fig. 12 shows an optical photograph of the passive half of a Mach–Zehnder interferometric amplitude modulator which was formed by joining two Y-splitters. Deposition of electrode structures along the arms of this device creates an active amplitude modulator appropriate for use in integrated optic circuits. An important feature of our fabrication technique is that it is possible to adjust the arm interference at zero bias after the initial processing. This can be done, for instance, by selectively removing the GaAs material in a local region of one arm of the waveguide, thus changing the local effective index of refraction. By monitoring the device output while etching, *in situ* tailoring of device characteristics is possible.

As another application of the use of passive components, we are currently using tapered waveguides to couple guided light into and out of diffraction gratings for wavelength demultiplexing applications.

V. Conclusion

In summary, the technique of laser-induced photoelectrochemical etching has been used to fabricate low-loss single-mode waveguides and passive waveguiding structures and devices. The maskless nature of this processing technique makes it a useful tool for prototyping integrated optic circuits and for use in optical packaging. Although not discussed in this paper, unique characteristics of the process, such as the ability to locally control the etch depth, offer the potential for fabricating novel integrated optic device structures. In particular, the potential of graded effective index structures for loss reduction in waveguide tapers and bends deserves special mention [2], [3]. The impact of low-loss waveguide tapers in reducing coupling losses between waveguides and insertion losses from fibers into substrate-based devices is an interesting and important issue which laser fabrication techniques may be capable of addressing.

Finally, the techniques and devices discussed in this paper are being used to fabricate active devices such as electro-optic modulators and switches, as well as useful passive devices such as wavelength selective filters and wavelength demultiplexers. In particular, we have developed an amplitude modulator based on our waveguides which demonstrates high extinction ratio and low switching voltage. These results will be described in a separate work.

This research was supported by the National Center for Integrated Photonic Technology and the Air Force Office of Scientific Research/Defense Advanced Research Projects Agency.

References

[1] A. E. Willner, M. N. Ruberto, D. J. Blumenthal, D. V. Podlesnik, and R. M. Osgood, Jr., "Laser fabricated GaAs waveguiding structures," *Appl. Phys. Lett.*, vol. 54, p. 1839, 1989.

[2] M. N. Ruberto, R. Scarmozzino, A. E. Willner, D. V. Podlesnik, and R. M. Osgood, Jr., "Graded-effective-index waveguiding strucutres fabricated with laser processing," *SPIE Proc.*, vol. 1215, p. 538, 1990.

[3] R. Scarmozzino, D. V. Podlesnik, and R. M. Osgood, Jr., "Losses of tapered dielectric slab waveguides with axial variations in index of refraction," *IEEE Trans. Microwave Theory Tech.*, vol. 38, p. 141, 1990.

[4] R. R. Krchnavek, G. R. Lalk, and D. H. Hartman, "Laser direct writing of channel waveguides using spin-on polymers," *J. Appl. Phys.*, vol. 66, p. 5156, 1989.

[5] R. R. Krchnavek, G. R. Lalk, and R. Denton, "Photo-polymerized acrylic waveguides for optical interconnects," *MRS Symp. Proc.*, Spring Meeting (Anaheim, CA), 1991.

[6] K. W. Beeson, K. A. Horn, M. McFarland, and J. T. Yardley, "Photochemical laser writing of polymeric optical waveguides," *Appl. Phys. Lett.*, vol. 58, p. 1955, 1991.

[7] J. Y. Tsao, R. A. Becker, D. J. Ehrlich, and F. J. Leonberger, "Photodeposition of Ti and application to direct writing of Ti:$LiNbO_3$ waveguides," *Appl. Phys. Lett.*, vol. 42, p. 559, 1983.

[8] M. N. Ruberto *et al.*, "The laser-controlled micrometer-scale photoelectrochemical etching of III-V semiconductors," *J. Electrochem. Soc.*, vol. 138, p. 1174, 1991.
[9] S. Li, G. Scelsi, M. N. Ruberto, R. Scarmozzino, and R. M. Osgood, Jr., "Factors controlling the resolution in the laser-induced aqueous etching of semiconductors using a focused cw beam," *Appl. Phys. Lett.*, vol. 59, p. 1884, 1991.
[10] R. Scarmozzino, D. V. Podlesnik, A. E. Willner, and R. M. Osgood, Jr., "Modeling of rib-like waveguides with isolation trenches of finite width," *Appl. Opt.*, vol. 28, p. 5203, (1989).
[11] P. K. Tien, "Light waves in thin films and integrated optics," *Appl. Opt.*, vol. 10, p. 2395, 1971.
[12] L. M. Johnson, Z. L. Liau, and S. H. Groves, "Low-loss GaInAsP buried-heterostructure optical waveguide branches and bends," *Appl. Phys. Lett.*, vol. 44, p. 278, 1984.
[13] M. Kuznetsov, "Radiation loss in dielectric waveguide Y-branch structures," *J. Lightwave Technol.*, vol. LT-3, p. 674, 1985.

Louay Eldada (M'88) was born in Beirut, Lebanon, on October 3, 1966. He received the B.S. and M.S. degrees from the Columbia University School of Engineering and Applied Science in 1989 and 1991, both in electrical engineering. He is currently a Ph.D. student in electrical engineering at the Columbia University Graduate School of Arts and Sciences.

In 1990, he worked as a research assistant at the IBM East Fishkill laser laboratory. His work involved setting up laser systems for the study of interaction of light with matter. Since 1991, he has been engaged in research at the Columbia University Microelectronics Sciences Laboratory in a variety of topics related to laser-induced processing of electronic materials, especially III-V compound semiconductors. These include materials deposition and etching as well as integrated optical devices fabrication and characterization.

Mr. Eldada is a member of OSA.

Mark N. Ruberto (M'87) was born in New York City on July 29, 1961. He received the B.S. in physics from Muhlenberg College, Allentown, PA in 1983, where he was the recipient of the Eastman Kodak Scholarship Prize in physics. He completed the M.S. degree from Drexel University, Philadelphia, PA, in 1986 and the Ph.D. degree from Columbia University, N.Y. in 1991 both in electrical engineering. His doctoral research involved the use of laser material processing to study the micrometer-scale etching of GaAs/AlGaAs heterostructures, and to fabricate semiconductor electrooptic and passive waveguiding devices.

Presently, he is a Postdoctoral Research Fellow at the Technion-Israel Institute of Technology in Haifa, Israel. He is currently investigating the performance of compound cavity laser structures using both semiconductor and Er-doped fiber gain media as well as the use of Er-doped amplifiers in microwave fiber-optic links.

Dr. Ruberto is a member of the Laser and Electro-Optical Society, and the Optical Society of America.

Robert Scarmozzino was born in New York, NY, on July 12, 1961. He received the B.S. and M.S. degrees from the Columbia University School of Engineering and Applied Science in 1982 and 1983, and the Ph.D. degree from the Columbia University Graduate School of Arts and Sciences in 1987, all in applied physics. His graduate research was in the area of plasma physics, and primarily consisted of an experimental and theoretical study of collisionless trapped particle instabilities.

Since 1987, Dr. Scarmozzino has been engaged in research at the Columbia University Microelectronics Sciences Laboratory in a variety of applied physics topics related to laser-induced semiconductor processing. These include experiments with, and modeling of, materials deposition and etching, process diagnostics, and integrated optical devices. He is currently a Research Scientist at the Columbia University Microelectronics Sciences Laboratory.

Dr. Scarmozzino has been a member of the American Physical Society, the Materials Research Society, the Electrochemical Society, the International Society for Optical Engineering, and the Sigma Xi Society.

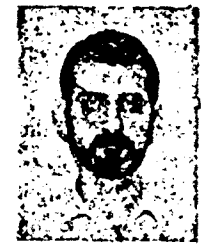

Miguel Levy was born in Lima, Peru. He received the B.S. degree from Duke University in 1972, the M.S. from Cornell University in 1975, and the Ph.D. degree from the City College of New York in 1988, all in physics. His graduate research was in the areas of theoretical and experimental condensed matter physics, primarily on optical and transport studies of heavily doped semiconductors near the metal-insulator transition.

Since 1991 he has been engaged in research on optoelectronic devices at the Columbia University Microelectronics Sciences Laboratory, where he is currently a postdoctoral Research Scientist.

Richard M. Osgood (SM'82–F'87) received the B.S. degree in Engineering at the U.S. Military Academy, the M.S. degree in physics at Ohio State University, and the Ph.D. degree in physics at the Massachusetts Institute of Technology.

He is Professor of Electrical Engineering and Applied Physics at Columbia University in the City of New York. Prior to this appointment, he served on the scientific staff of M.I.T., Lincoln Laboratory (Solid State Physics Division), the U.S.A.F. Avionics Laboratory, and the U.S.A.F. Materials Laboratory. Throughout his professional career he has performed research in many areas of Electrical Engineering, Physical Chemistry and Optical Physics. His most extensive research has been in the development of new infrared and ultraviolet lasers, the application of laser-induced chemistry to materials preparation, and optical surface physics and chemistry.

Dr. Osgood is a member of the ACS, OSA, MRS and a Fellow of the IEEE. He is Co-Editor of *Applied Physics*. Along with Dr. Steven Brueck, he organized the first MRS symposium on Laser Diagnostics and Photochemical Processing. He has served as a consultant to numerous government and industrial organizations, including the DARPA Materials Research Council, DOE Basic Energy Sciences Advisory Board and the Los Alamos National Laboratory Chemistry Advisory Board. In October of 1983, Dr. Osgood was elected to a 3-year term as councillor of the Materials Research Society, and in 1986, he was selected to be an IEEE-CLEOS Distinguished Travelling Lecturer. In 1991, Dr. Osgood received the R.W. Wood Prize from the Optical Society of America and in 1992 he was appointed as a Distinguished Fellow. Also in 1992, Dr. Osgood was appointed as a Distinguished Travelling Lecturer for 1991–1993. Dr. Osgood was formerly the Co-Director of the Columbia Radiation Laboratory and Director of the Microelectronics Sciences Laboratories.

Fabrication of Narrow-Band Channel-Dropping Filters

M. Levy, L. Eldada, R. Scarmozzino, R. M. Osgood, Jr., P. S. D. Lin, and F. Tong

Abstract—**In this letter we describe the first fabrication and demonstration of narrow-band channel-dropping filters which have recently been proposed for use in high-bit-rate communication systems. The devices use waveguide couplers combined with quarter-wave shifted DFB resonators and can, in principle, produce resonant transfer of 50% of incident power with sub-angstrom bandwidths. Our results show resonant transfer of power at the expected wavelength and within the expected range of efficiency and bandwidth for our designs.**

Introduction

THE increased interest in dense wavelength division multiplexing for optical broadcast networks has generated the need for a narrow-band optical filter which can be used to extract a single wavelength signal from a multiple wavelength optical bus. Wavelength division multiplexing can be used to increase the network capacity by partitioning the large fiber bandwidth into narrow channels spaced appropriately [1], [2]. For example, if the communication is at a wavelength of 1.55 μm and each channel is given a bandwidth of say 5 GHz, one needs optical filters of the order of 0.5 Å bandwidth.

Recently, a novel design for a narrow-band channel-dropping filter (CDF) has been proposed by Haus [2]. The filters use waveguide couplers combined with quarter-wave shifted DFB resonators, and are capable of selecting channels significantly narrower than 1 Å bandwidth, by appropriate choice of the coupling parameters in the device. In this letter we demonstrate the fabrication and operation of such a device for the first time. The waveguide coupler and other waveguide components are produced using a technique we have developed for prototyping integrated optical devices by maskless laser etching of GaAs [3]; once tested, these components can be made by more conventional planar processing. The grating is patterned in photoresist using *e*-beam writing and etched using chemically assisted ion beam etching. The device has been tested and the results show resonant transfer of power at the expected wavelength and within the expected range of efficiency and bandwidth for our designs.

Manuscript received August 17, 1992. This work was supported by the Defense Advanced Research Projects Agency/Air Force Office of Scientific Research and the National Center for Integrated Photonic Technology and the U.S. Army Research Office.

M. Levy, L. Eldada, R. Scarmozzino, and R. M. Osgood, Jr. are with Columbia University Microelectronics Sciences Laboratory, New York, NY 10027.

P. S. D. Lin is with Bellcore, Red Bank, NJ 07701.

F. Tong is with IBM T. J. Watson Research Center, Yorktown Heights, NY 10598.

IEEE Log Number 9204690.

CDF Principle and Design

A diagram of the CDF described in this work is shown in Fig. 1(a). The device basically consists of two coupled waveguides, one of which has a quarter-wave shifted DFB resonator in the coupling region. This device produces resonant coupling of light to the receiver arm in an extremely narrow wavelength region, while allowing the remaining wavelength signals to pass unperturbed through the transmission bus. This narrow bandwidth results from the high Q of the resonant DFB cavity, and can be controlled by adjusting cavity losses through the inter-waveguide coupling between the bus and the resonator, the position of the quarter-wave step and the magnitude of the grating coupling constant. While it is possible, in principle, to incorporate amplification into the CDF, we confine our efforts here to a demonstration of the basic passive device.

The design of our device was based on several requirements. In order to have the device operate at a resonant wavelength near 1.55 μm, the grating spacing was chosen to be $\Lambda = 232.5$ nm ($\lambda_{res} = 2\Lambda n_{eff}$). The grating fabrication process produces rectangularly shaped gratings, and is limited to an etch depth of the order of the grating spacing. To be conservative, we chose a grating depth of 180 nm, giving a grating coupling constant, κ, of the order of 70 cm^{-1} for our waveguides. Next, several physical constraints were used to determine the waveguide coupling constant, μ, and the length of the coupling/grating region. Maximum power transfer to the resonator arm is achieved when [2]

$$L_b = \frac{1}{2\kappa} \ln\left(\frac{1}{2}\left|\frac{\kappa}{\mu}\right|^2\right), \qquad L_a \gg L_b \tag{1}$$

where L_a and L_b are, respectively, the lengths of the grating before and after the quarter-wave step in the asymmetric DFB cavity. In order to minimize the difficulty of fabricating the grating over too long a length, we chose to limit the total length of the coupling/grating region to 1 mm to reduce potential registration problems between the 80 μm long fields of the *e*-beam writing system. Given the above constraint on the total length, along with calculations which showed that reasonable transfer requires $L_a > \sim L_b$, this limited L_b to $< \sim 400$ μm, and implied

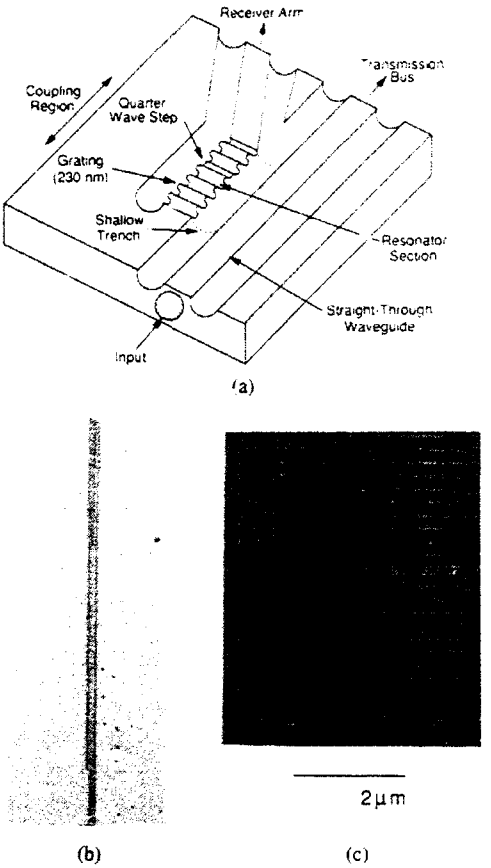

Fig. 1. (a) Schematic diagram of a channel-dropping filter design. (b) Optical photograph of a channel-dropping filter fabricated in GaAs. (c) SEM photograph of a short length of the grating showing the quarter-wave (half-period) step.

$\mu > \sim 3\ \text{cm}^{-1}$ by (1). Studies of interwaveguide coupling showed that μ's of 1–50 cm^{-1} were obtainable with our waveguide design. To achieve a narrow filter width we kept μ small, since the ratio of the bandwidth to the stop band is proportional to $(\mu/\kappa)^2$. Due to the logarithmic dependence of L_b on μ expressed in (1), a significant reduction in device length, while maintaining narrow bandwidth, would not be possible without a much larger κ than was available to us. The final design parameters and the theoretical performance of the device are shown in Fig. 2. This response is obtained from numerical solution of the coupled mode equations presented in [2], with the addition of the effects of waveguide loss and of different waveguide propagation constants at the resonant wavelength. The figure shows a broad spectrum including the stopband and the inset shows the detail of the resonant peak. The graph indicates that for an ideal device matching the design parameters, nearly 50% power can be transferred, with an expected FWHM bandwidth of 0.3 Å.

Fabrication

The device was fabricated on a GaAs slab waveguide heterostructure. This structure consisted of a 1.3 μm thick GaAs waveguiding epilayer, silicon doped to an impurity level of $n = 10^{16}\ \text{cm}^{-3}$, and a 2.7 μm thick

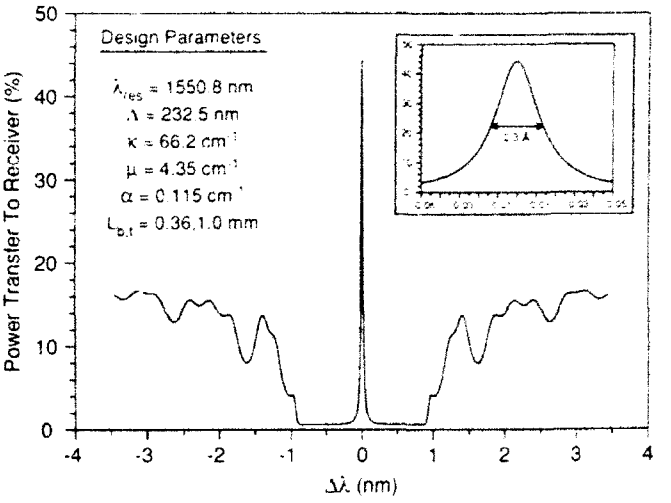

Fig. 2. Theoretical response of the channel-dropping filter diagramed in Fig. 1(a) for the design parameters shown in the figure.

$Al_{0.1}Ga_{0.9}As$ cladding layer, doped to the same impurity level. The substrate was n-type GaAs. The device illustrated in Fig. 1(a) was etched in the top GaAs epilayer as follows.

The waveguide components were produced using a maskless fabrication technique developed in our laboratories and described in detail elsewhere [3]. The process uses a focused laser beam to etch photoelectrochemically shallow, micrometer-scale grooves in GaAs [4]. These grooves serve to lower the effective refractive index in the region under the grooves and thus guide light in the epilayer region between the trenches. The technique produces single-mode waveguides with losses as low as 0.6–0.9 dB/cm [3].

The above technique was particularly useful in prototyping the channel-dropping filters since it allowed simple controlled adjustment of the coupling coefficient for each of several devices fabricated on a single sample. The coupling adjustment was made primarily by varying the depth of the central trench.

After the waveguides were fabricated, registration marks were etched in the sample to allow precision alignment of the grating with respect to the waveguide coupling region. The gratings were then patterned in photoresist using an *e*-beam writing system. As noted earlier, the field length of this apparatus is only 80 μm, thus the field pattern had to be repeated many times to cover the 1 mm coupling region, which included the quarter-wave step. Finally, the gratings were etched using a chemically assisted ion beam etching system.

An optical photograph of the fabricated device showing the coupling region and part of the input and output waveguides is given in Fig. 1(b). An SEM photograph of a short length of the grating showing the quarter-wave (half-period) step is given in Fig. 1(c).

Results and Discussion

The device was tested as follows. The output from an HP 8168A tunable laser source was sent through a polar-

ization maintaining fiber, and TE light was launched into the input waveguide by butt coupling the fiber to the cleaved end facet of the device. The output of the device was imaged onto an IR camera or detector using a microscope objective, and an aperture was used to select the light emanating from either the receiver arm or the transmission bus. A chart recorder was used to record the signal in the receiver arm as a function of wavelength.

The measured response in the receiver arm is shown in Fig. 3. Fig. 3(a) shows the resonant response and the response outside the stopband. Detail of the resonant response is shown in Fig. 3(b). All six of the CDF devices fabricated exhibit the two main peaks which appear in the stopband. These peaks are entirely repeatable and reproducible from scan to scan for each device. The narrow peak at about 1552 nm is the fundamental resonant response for the device, and is discussed in the following paragraph. The nonzero background signal in the stopband may result from leakage of light from the transmission bus into the receiver arm in regions outside the effective range of the grating (e.g., in the *Y*-branch). The large lobes at the edges of the stopband are characteristic of this type of filter (as shown in Fig. 2), but their medium scale structure depended on the particular device and is not a permanent feature of the response. The response outside the range shown in Fig. 3(a) eventually levels off and becomes independent of wavelength. The high frequency variations present throughout the entire signal are due to Fabry–Perot resonances from the end facets of the device, and are observable with this measurement apparatus when looking at the transmission of a simple straight waveguide. This is shown in the inset to Fig. 3(b). These high frequency variations would be eliminated in a practical device through the use of antireflection coatings on the waveguide facets.

The most important feature of the response is the pronounced narrow peak at about 1.5518 μm, which exhibits a FWHM bandwidth of 0.8 Å and a power transfer of about 30%. The peak position is in good agreement with the expected resonant wavelength of 1.5508 μm, and the power transfer is also in the predicted range. Further, it was found that this peak was accompanied by a corresponding decrease in the power observed in the transmission bus. The shift of the peak from the center of the stopband can be shown by theoretical calculations to result from a few degree error in the quarter-wave phase. The bandwidth is somewhat larger than expected, but this may be due to several factors including fabrication error in the etch depths which determine the coupling coefficients, misregistration in the fabrication of the grating, or higher than expected waveguide loss.

The response also shows a much broader peak at 1.5500 μm, with a FWHM bandwidth of about 4 Å and a power transfer of $>30\%$. The presence of this additional peak can be anticipated from the presence of waveguide modes other than the fundamental. For example, a higher order mode in either the individual waveguides or the combined coupler structure would have a lower effective index yielding an additional resonance at a wavelength ~ 1–3 nm less than the fundamental. These modes could be eliminated by refinements in the waveguide design. In addition, since the light from the fiber is launched close to the grating/coupling region (~ 1 mm), a band of radiation modes may still be present at the input to the coupler structure, and these would couple through the grating into the output. In a practical integrated structure, these modes would have already been stripped from the input beam.

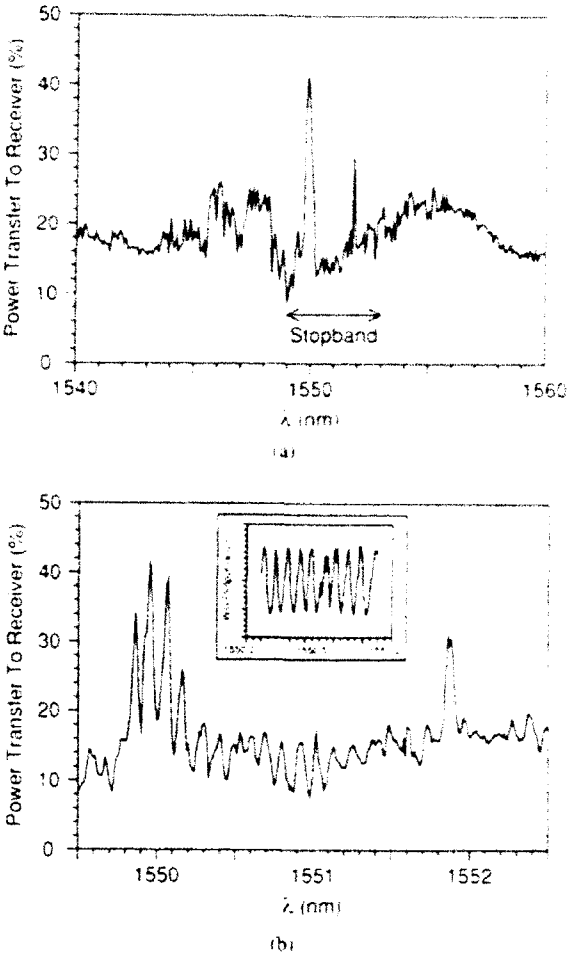

Fig. 3. Measured response of the CDF shown in Fig. 1(b), (c) over the wavelength ranges (a) 1540.0–1560.0 nm and (b) 1549.5–1552.5 nm. The inset gives the response of a straight waveguide, and shows Fabry-Perot peaks similar to those exhibited by the CDF.

Conclusion

In summary, we have fabricated the first channel-dropping filter of the type proposed in [2], and have demonstrated the basic principle of operation. The results show resonant transfer of power at the expected wavelength and within the expected range of efficiency and bandwidth for our designs. Further work is underway.

Acknowledgment

The authors would like to express their appreciation for many helpful and illuminating discussions with H. A. Haus and J. Damask at MIT. We would also like to thank

P. Chapman and R. Tiberio of the National Nanofabrication Facility at Cornell University for their assistance in etching the gratings.

REFERENCES

[1] H. Toba, K. Oda, K. Nakanishi, N. Shibita, K. Nosu, N. Takato, and M. Fukuda, "A 100-channel optical FDM transmission/distribution at 622 Mb/s over 50 km," *J. Lightwave Technol.*, vol. 8, p. 1396, 1990.

[2] H. A. Haus and Y. Lai, "Narrow-band optical channel-dropping filter," *J. Lightwave Technol.*, vol. 10, p. 57, 1992.

[3] I. Eldada, M. N. Ruberto, R. Scarmozzino, M. Levy, and R. M. Osgood, Jr., "Laser-fabricated low-loss single-mode waveguiding devices in GaAs," *J. Lightwave Technol.*, to be published.

[4] M. N. Ruberto, X. Zhang, R. Scarmozzino, A. E. Willner, D. V. Podlesnik, and R. M. Osgood, Jr., "The laser-controlled micrometer-scale photoelectrochemical etching of III-V semiconductors," *J. Electrochem. Soc.*, vol. 138, p. 1174, 1991.

Submitted to Photonics Technology Letters 10/27/92.
Accepted 12/92

Thin-Film-Magnet Magneto-Optic Waveguide Isolator

M. Levy, I. Ilic, R. Scarmozzino, and R.M. Osgood, Jr.
Columbia University Microelectronics Sciences Laboratory
New York, NY 10027

R.Wolfe
AT&T Bell Laboratories
Murray Hill, New Jersey 07974

C.J. Gutierrez,* and G.A. Prinz
Naval Research Laboratory
Washington, D.C. 20375

ABSTRACT

Recent advances in thin-film-magnet and Bi-YIG film technologies have opened up the possibility of fabricating very compact magneto-optic structures. In this paper we demonstrate for the first time that these new technologies can be brought together to make a thin-film-magnet magneto-optic isolator for use in optical packaging and integrated optical circuits. The device operates at a 1.55 μm wavelength and uses a waveguide etched into a Bi-YIG film whose linear birefringence has been tuned to near zero at this wavelength. The Bi-YIG's magnetization is saturated by a thin ferromagnetic film. Isolation ratios of -21 dB have been obtained.

* Present address: Department of Physics, Southwest Texas State University, San Marcos, TX 78666

There is a persistent need for a compact optical isolator in optical packaging and integrated optical circuits. Current isolator technology is limited by the requirement for bulk magnets to induce Faraday rotation in YIG or Bi-YIG crystals. A thin-film magnet would allow a considerable reduction in size relative to current designs, and, more important, it would also open up the possibility for fully integrating optical isolators on a single wafer.

Within the last decade there have been significant advances in both thin-film magnets and bismuth-yttrium-iron-garnet (Bi-YIG) film technology. For example, it is now possible to fabricate single-crystal films of iron or iron alloys.[1,2] These films are grown by molecular beam epitaxy on GaAs substrates and have large magnetization densities and good coercivities. High-magnetization polycrystalline films of samarium-cobalt or neodymium-iron-boron with coercivities as large as 15 kilogauss can also be grown by electron beam evaporation.[3] In addition, recent advances in Bi-YIG film technology have made it possible to fabricate ridge-waveguide Faraday-rotation isolators having zero linear birefringence and isolation ratios of -35 dB.[4]

The availability of metallic films, which could serve as miniature permanent magnets, opens up the possibility of fabricating very compact magneto-optic structures. In this paper we demonstrate for the first time that these new technologies can be used to make a thin-film-magnet optical isolator. The basic structure of this device, as shown in Fig.1a, consists of a magnetic film on top of a Bi-YIG waveguide, separated by an appropriate buffering material. Alternatively, the film may be placed on the sides of the waveguide ridge, as shown in Fig.1b.

Our tests use a 1.5-μm-thick epitaxial iron-cobalt film, but the results are applicable to the other magnetic films mentioned above, or to high-magnetization ribbons of sintered magnetic

powders. The results presented here demonstrate that these very small magnets can be used in a working waveguide magneto-optic isolator. The tests are carried out on the first type of structure shown in Fig.1a, but they also apply to the other structure since the magnetic field induced in either case is approximately the same within the optical channel of the isolator.

There are several characteristics of Bi-YIG and metal-film technology that make this isolator workable. First, the easy axes of magnetization for the Bi-YIG are nearly in-plane.[6] Therefore the unavoidable small vertical components in the magnetic field which are necessary to close the flux loops do not disturb the saturation of the Bi-YIG magnetization. Second, the saturation field for the Bi-YIG is relatively small - as low as 10 Oersted or lower. Third, the iron-cobalt film has a large magnetization and can generate a return flux capable of saturating the Bi-YIG, even though the magnet's thickness is only of the order of 1 μm.[7] Fourth, the specific Faraday rotation of the Bi-YIG is large enough to provide the needed 45° rotation in the small distances over which the metal film can saturate the Bi-YIG.

In order to determine the feasibility of utilizing iron-cobalt alloy films with waveguide YIG structures, we calculated the magnetic field induced by a typical film along the length of the waveguide. For the geometry shown in Fig.2a, the field can be written as a surface integral involving the normal component of the magnetization.[5] The expression for the total magnetic field separates into two terms, one from each of the two magnetically-charged pole faces of opposite sign, normal to the direction of magnetization. The field term due to a single face is given by

$$H(x) = \iint_S dx_2' dx_3' \; n \cdot M \sum_{i=1}^{3} \frac{(x_i - x_i')\ell_i}{\left[\sum_{j=1}^{3} (x_j - x_j')^2\right]^{m}} \qquad \text{Eq.(1)}$$

where the integration is over the face area, S, and the expression is in Gaussian units. M is the magnetization density, n is the unit vector normal to the face, and the Cartesian coordinates are as shown in Fig.2a. The dimensions of the magnetic film are L × 2b × h. In order to solve this integral exactly it is necessary to resort to numerical methods. For the case where b >> L, however, Eq.1 can be expressed in closed form. Letting b → ∞, we obtain,

$$H_1(x_1,0,x_3) = 2M \cdot n \left(\arctan\frac{x_3 - h}{x_1} - \arctan\frac{x_3}{x_1}\right) \qquad \text{Eq.(2)}$$

$$H_3(x_1,0,x_3) = M \cdot n \ln\left[\frac{x_1^2 + (x_3 - h)^2}{x_1^2 + x_3^2}\right] \qquad \text{Eq.(3)}$$

for a face at x = 0.

Figure 2b shows the magnitude of the horizontal field as a function of L, at a position 8 μm below the surface of the magnet and at the midpoint between the two magnetically charged ends. This is the point where the horizontal component of the magnetic field is smallest in the waveguide, except for a small region directly below the faces. The calculation is for the case

where h = 1.5 μm and $4\pi M$ = 21,000 Oersted, which are typical of our experiments. The vertical field component is always a small fraction of the horizontal component, except very near the pole faces. To avoid domain formation near the ends of the waveguide due to large vertical fields, the magnet should overhang the ends of the waveguide by a small distance of the order of 10 μm. The inset to Fig.2b shows the horizontal and vertical components along the length of the magnet for the case of L = 3 mm.

Since saturating fields of 10 Oersted or even lower are routinely attainable for Bi-YIG samples with in-plane easy axes of magnetization,[4,6] the calculation shows that these iron-alloy films induce enough magnetic flux to saturate the isolator. Figure 2b shows that to maintain a minimum field in the range of 5 to 10 Oersted requires a magnet with a maximum length between 2 mm and 4 mm.

For the tests reported in this letter, the iron-cobalt alloy film, together with its GaAs substrate, was placed film-side down on top of the Bi-YIG isolator. We anticipate that full integration can be achieved, however, by either detaching the magnetic film by means of epitaxial liftoff techniques,[8] evaporating polycrystalline films directly on the YIG crystal, or bonding thin sintered magnetic powders onto the Bi-YIG surface. We are presently investigating these possibilities.

The iron-cobalt alloy films used in our experiments are single-crystal films, grown by molecular beam epitaxy on (110) GaAs substrates. Their alloy composition was 30% iron and 70% cobalt. These novel films[2] have a single easy axis of magnetization along the $<\bar{1}10>$ direction of the GaAs and a higher coercivity than pure iron films. Hysteresis studies of these films show a flat rectangular response to an applied magnetic field and a coercivity of about

50 Oersted, with a remanent $4\pi M$ of about 21,000 Oersted.[9] The GaAs substrates were cut into rectangular shapes of different lengths, with the variable-length short side along the $<\bar{1}10>$ direction and the long side equal to 1 cm in length. The iron-cobalt films were then grown on the GaAs such that the easy axis of magnetization was along the short side in the rectangular film. For the experiments described here, the iron-cobalt alloy film was an assembly of two or three samples joined to form a length of 4.0 mm. The results did not depend strongly on which film set was used.

The waveguides used in these experiments were triple-layer Bi-YIG films[4] designed to support single TE and TM modes. The films were grown by standard liquid phase epitaxy on (111)-oriented gadolinium-gallium-garnet substrates. The top two epilayers have a nominal composition $(Bi_{0.5}Y_{2.5})(Fe_{3.7}Ga_{1.3})O_{12}$. The films were subjected to annealing procedures described in References 4 and 10 to ensure near-planar magnetization anisotropy of the upper layers. The linear birefringence was reduced to zero at a wavelength near 1.5 μm by etching the top surface in phosphoric acid.[4,10] This novel etch-tuning method makes use of the opposite signs of stress-induced birefringence and the thickness dependent shape birefringence in the top layer to ensure a linear increase of the Faraday rotation angle with distance when the magnetic field is parallel to the light-propagation direction. Ridge waveguide patterns were then etched into the surface, parallel to one of the easy axes of magnetization of the Bi-YIG sample, and a thin silica overlayer was sputtered over it to tune the zero birefringence to a wavelength near 1.55 μm.[4] This silicon oxide layer acted as a buffer between the metallic iron-cobalt film and the waveguides.

The Faraday rotation in the Bi-YIG films was measured to be 127°/cm at a wavelength

of 1.55 μm. The sample was therefore cut to a length of 3.55 mm to provide 45° of rotation, and the edges were optically polished.

Linearly polarized light at 1.55 μm from a DFB diode laser was then coupled into one end of a ridge waveguide through a polarization-maintaining single-mode fiber. The light emerging from the other end was collimated with a microscope objective, passed through a metallic thin-film near-infrared analyzer, and detected with a germanium photodetector coupled to a multimeter. Magnetization with a bulk magnet showed 45° Faraday rotation, as expected.

A fully-magnetized 4 mm iron-cobalt alloy film together with its GaAs substrate was then placed film down on top of the Bi-YIG sample, its magnetization parallel to the waveguiding ridges, as shown in Fig. 1a. The iron-cobalt film was found to induce a large Faraday rotation. However, the typical rotation was smaller than 45°, showing that the film magnet did not fully saturate the magnetization along the whole length of the waveguide. Therefore the Faraday rotation measured depends on the previous magnetization state of the Bi-YIG. If the Bi-YIG sample is poled by an external magnet for clockwise Faraday rotation and the iron-cobalt film is then placed over the optical channel so as to induce a counterclockwise rotation, we obtain a counterclockwise Faraday rotation of about 30°. This implies that the iron-cobalt alloy film saturates nearly 80 to 90 percent of the length of the waveguides in the above sample. According to the mathematical model presented at the beginning of this paper, the above result implies that the saturation field is about 5 to 6 Oersted for our Bi-YIG sample.

If, on the other hand, the iron-cobalt alloy film is oriented so as to produce a clockwise rotation, the same as that of the original poling magnet, the Faraday rotation induced in the Bi-YIG waveguide is about 40°, after the poling magnet is removed. In this case, the full 45°

rotation is not achieved, as end effects near the edges of the Bi-YIG waveguide require a larger saturating field than in the main body of the optical channel. Since the strength of the magnetic field generated by the iron-cobalt film increases rapidly near its pole faces, as shown in the inset to Fig.2b, one can adjust the overhang of the film beyond the ends of the waveguide to saturate the Bi-YIG magnetization near the edges. We demonstrated this by placing a 3.3 mm long iron-cobalt film at an angle to the waveguide axis so as to produce an overhang of about 50 to 100 μm at each end of the waveguide. This resulted in a 45° Faraday rotation, indicating that the field generated by the iron-cobalt alloy film is sufficient to keep the Bi-YIG magnetization saturated over the whole length of the waveguide, parallel to the optical channel axis.

The above results demonstrate the feasibility of the thin-film-magnet magneto-optical isolator proposed in this paper. For a practical device, one would need shorter Bi-YIG waveguides and iron-cobalt films, say 3 mm or less, so as to fully saturate the magnetization in the optical channel, assuming the same saturation field as for the present sample. Care must also be taken to obtain an appropriate overhang of the iron-cobalt film beyond the Bi-YIG waveguide. Bi-YIG samples with higher specific Faraday rotations capable of generating 45° rotations in 1 mm to 3 mm can be produced by increasing the bismuth content in the waveguiding epilayer and are fully within the realm of present Bi-YIG growth technologies.

In order to measure an effective isolation ratio for our device, the iron-cobalt piece was placed with its direction of magnetization parallel to the length of the waveguide ridge, and the analyzer was set at the extinction angle for this geometry. After measuring the power transmitted through the analyzer, the iron-cobalt film was rotated 180° so that its magnetization was oriented antiparallel to the original direction of magnetization, and the transmitted power was measured

again. With the magnetic field reversed, the light through the analyzer was then close to a maximum. Following R. Wolfe *et al.*,[4] the ratio of the detected intensities for the two magnetization directions was taken as the isolation ratio for the ridge waveguide isolator. The value obtained was 120 to 1, corresponding to an isolation ratio of -21 dB. Attenuation due to the less than 45° Faraday rotation was measured at about -1dB. However, this attenuation can be eliminated by shortening the length of the isolator, as explained above.

The factor currently limiting the isolation ratio to -21 dB in our isolator is the presence of residual linear birefringence at 1.55 μm. Etch-tuning the birefringence to zero at this wavelength and eliminating any magnetic linear birefringence by shortening the length of the device so as to fully saturate the magnetization along the waveguide axis should result in isolation ratios of -30 dB or better.[4]

M. Levy, I. Ilic, R. Scarmozzino, and R.M. Osgood, Jr. gratefully acknowledge AFOSR/DARPA for supporting this project and the NCIPT (DARPA) program at Columbia for providing instrumentation support. C.J. Gutierrez and G.A. Prinz thank the Office of Naval Research for program support. Also C.J.G. gratefully acknowledges support from the NRC/NRL Postdoctoral Associate program.

References

1. Gary A. Prinz, Science **250**, 1092 (1990).

2. C.J Gutierrez, J.J. Krebs and G.A. Prinz, Appl. Phys. Lett. , November 1992.

3. Typically $4\pi M \geq 21{,}000$ Oersted and coercivities of 50 Oersted are measured for iron-cobalt alloy films grown on (110) GaAs. High-magnetization films grown by electron beam evaporation require a 400°C to 500°C anneal in a magnetic field.

4. R. Wolfe, R.A. Lieberman, V.J. Fratello, R.E. Scotti, and N. Kopylov, Appl. Phys. Lett. **56**, 426 (1990).

5. J.D. Jackson, Classical Electrodynamics, 2nd Ed., John Wiley & Sons, p. 192.

6. M. McGlashan-Powell, R. Wolfe, J.F. Dillon, Jr., and V.J. Fratello, J. Appl. Phys. **66**, 3342 (1989).

7. The iron-cobalt films used in these experiments are closer to 1.5 μm thick.

8. E. Yablonovitch, W.K. Chan and A. Yi-Yan, Epitaxial Liftoff Technology for OEIC's, AIP, American Vacuum Society Series 10, Conference Proceedings, p.154 (1991).

9. D.I. Bardos, J. Appl. Phys., **40**, 1371 (1969)

10. R. Wolfe, V.J. Fratello, and M. McGlashan-Powell, J. Appl. Phys. **63**, 3099 (1988)

Figures

Fig.1 Basic structure of thin-film-magnet magneto-optic isolator. The iron-cobalt alloy film must overhang the input and output ends by a few tens of microns to avoid large vertical fields on the waveguide. Figure 1a shows placement on top of the waveguide and Fig.1b shows lateral placement.

Fig.2 a) Shaded areas show the magnetically charged end faces of the iron-cobalt alloy film normal to the $<\bar{1}10>$ direction. b) Magnitude of the magnetic field as a function of magnet length, L, 8 μm below the iron-cobalt film's bottom surface and midpoint between the two magnetically charged ends. The field is calculated for a 1.5-μm-thick film magnet with $4\pi M$ = 21,000 Oersted. The horizontal broken lines denote typical saturating fields. The inset to Fig.2b shows the magnitudes of the horizontal and vertical components of the field as a function of distance from one of the faces for a film 3 mm in length, and 8 μm below the iron-cobalt film's bottom. The solid line is the longitudinal component, parallel to the waveguide ridge. The broken line is the component normal to the plane of the film.

Fig. 1

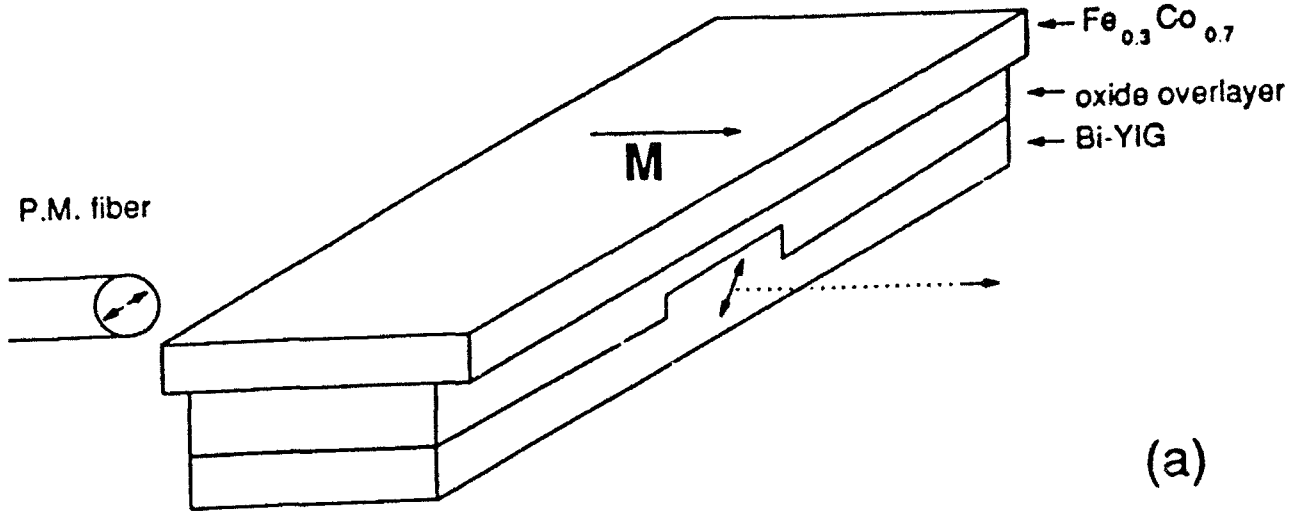
$Fe_{0.3}Co_{0.7}$
oxide overlayer
Bi-YIG
M
P.M. fiber

(a)

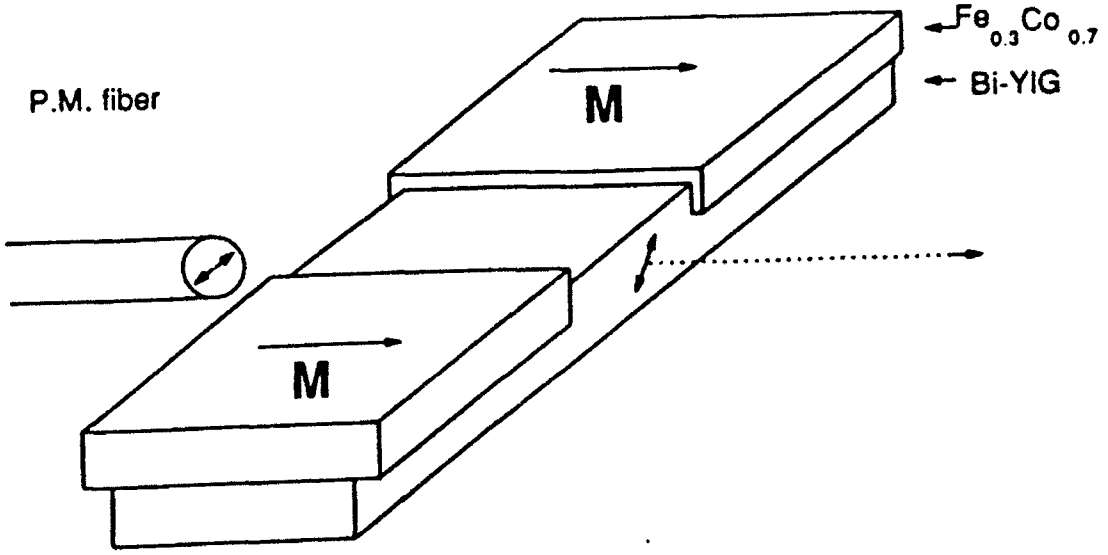
$Fe_{0.3}Co_{0.7}$
Bi-YIG
M
P.M. fiber
M

(b)

Fig. 2

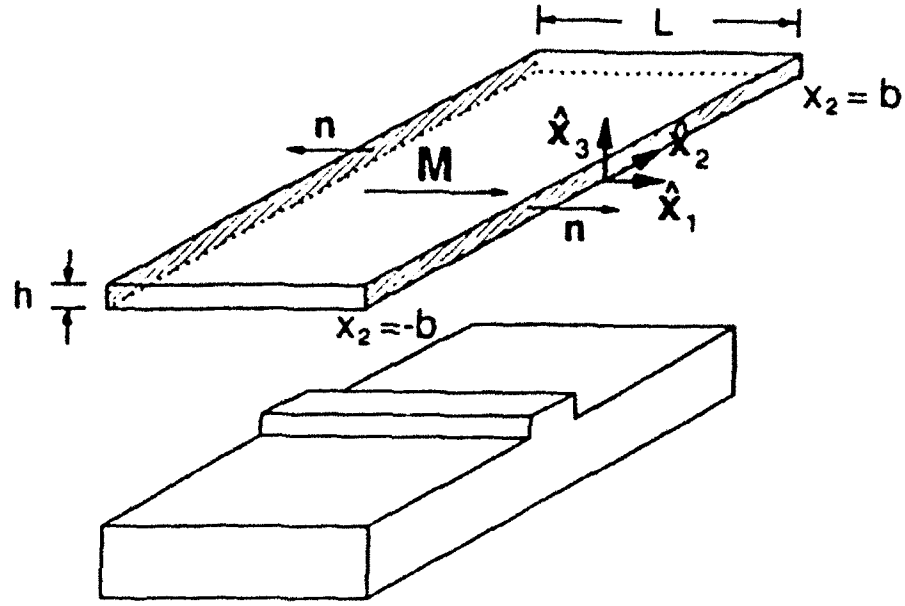
L
$x_2 = b$
n
M
$\hat{x}_3$
$\hat{x}_2$
$\hat{x}_1$
n
h
$x_2 = -b$

(a)

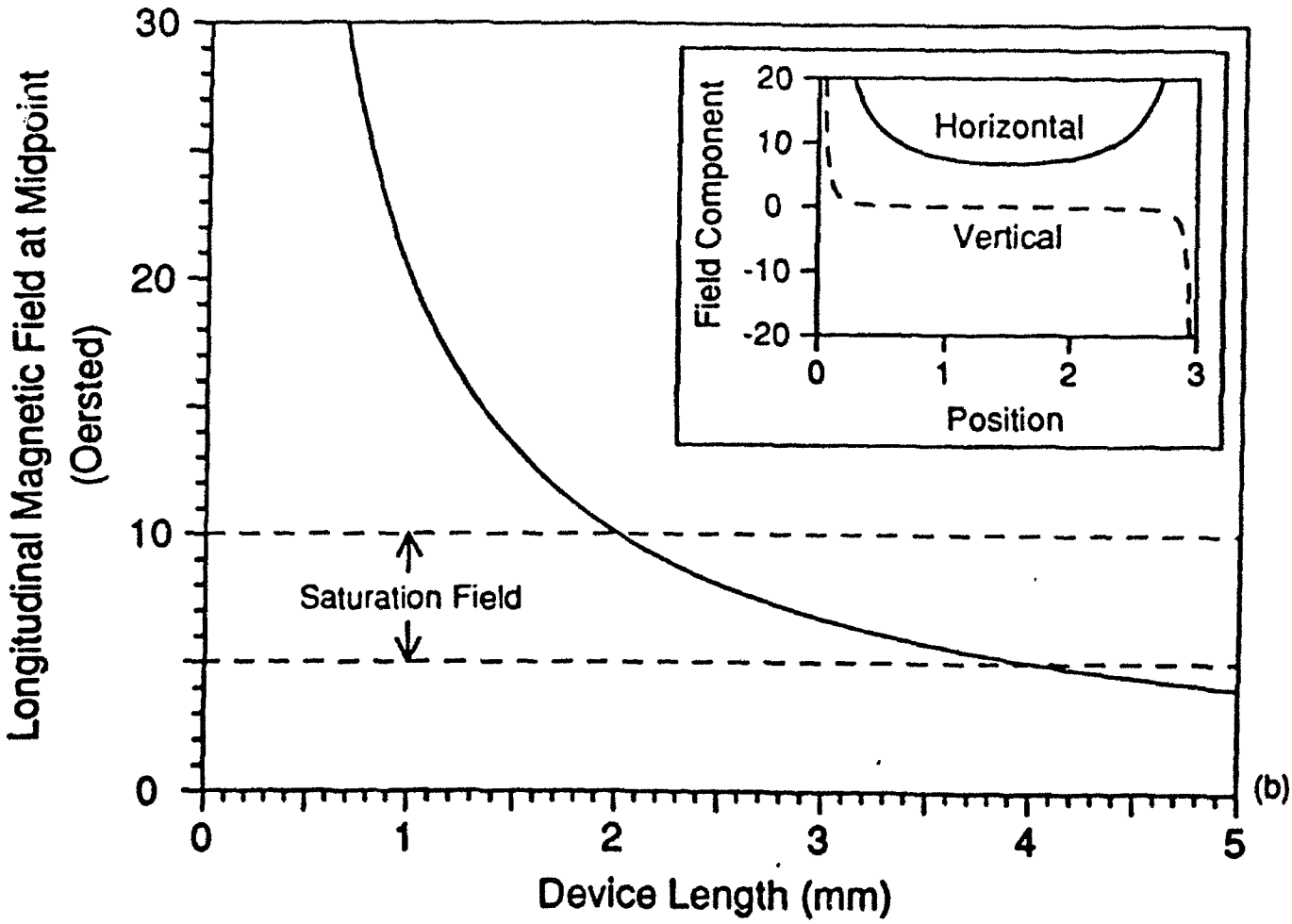
Longitudinal Magnetic Field at Midpoint (Oersted)
30
20
10
0
Saturation Field
0
1
2
3
4
5
Device Length (mm)
Field Component
20
10
0
-10
-20
Horizontal
Vertical
0
1
2
3
Position

(b)

Rapid Direct Fabrication of Active Electro-Optic Switches in GaAs

L. Eldada, N. Zhu, M.N. Ruberto, M. Levy, R. Scarmozzino, and R.M. Osgood, Jr.

Microelectronics Sciences Laboratories

Columbia University, New York, NY 10027, USA

Phone: (212) 854-6585

FAX: (212) 932-9421

ABSTRACT

We have developed several direct-write laser processing techniques to masklessly fabricate prototypes of waveguiding devices in GaAs/AlGaAs substrates. These are highly precise techniques that allow the rapid and cost-efficient fabrication and refinement of novel devices. Once tested and found satisfactory, designs can then be used for mass-fabrication by conventional means. We have used in the past our maskless laser-based technology to fabricate low-loss single-mode passive waveguiding structures and devices.[1,2] In this paper, we report new developments in our technology that allow the fabrication of active electro-optic switches. An electro-optic polarization modulator coupled with an external analyzer yielded an extinction ratio of 17 dB and a V_π of 4 V. An integrated amplitude modulator consisting of a polarization modulator and an on-chip polarizer exhibited an extinction ratio of 13 dB and a V_π of 6 V. An integrated Mach-Zehnder interferometer demonstrated an extinction ratio of 15 dB and a V_π of 5 V.

1. INTRODUCTION

The fabrication of integrated waveguide circuits, such as optical delay lines, arrays of switching devices, and multiple wavelength taps on a single waveguide bus, has requirements of layout and geometry which are considerably different from those of electronic integrated circuits. Patterning must be done over large areas and the spatial resolution required is relatively modest for the waveguides themselves. In addition, at present, the production volume for these circuits is relatively modest in comparison to those of commodity integrated circuits. Further, since computer simulation is not as advanced as for electronic circuits, it is important to have the ability to rapidly prototype integrated optical circuits onto a testable chip as a step in the design process.

These considerations have led us to develop a rapid, direct fabrication process for integrated optical circuits. The fabrication is based on a type of laser direct etching that uses a focussed scanned laser beam which is computer driven. Previously, using this technique, we demonstrated the fabrication of several passive integrated optical building blocks in GaAs;[1] namely, linear waveguides, bends, and Y-branches. From these, we were able to form simple passive devices including splitters and couplers. These devices had low optical loss, were single-mode, and could be accurately modelled using effective index calculations.

Because the fabrication technique is maskless and is locally controllable in real time, it can also be used to fabricate novel device structures.[3] Thus we have recently used it to make a channel-dropping filter.[2] In the process, we utilized the ability to locally vary the local effective index of refraction through control of the local etch depth to define the coupling region in the device.

In this paper, we report the use of this technique to make several active devices including polarization, amplitude, and Mach-Zehnder modulators. The etching for these devices is done by the direct process described above. In addition in one case we have used laser-defined local CVD to metallize a portion of the device. We have characterized the optical performance of these devices as well and found that they exhibit excellent characteristics.

Finally, while the materials used in this work are all GaAs/AlGaAs based, the techniques used are clearly extendable to other material systems as well such as InP and silicon. In addition, recent experiments in polymeric materials indicate that these materials may be amenable to a similar approach for prototyping.

2. LASER ETCHING TECHNIQUE

A detailed description of the experimental procedure and physical mechanism of laser-induced photoelectrochemical etching can be found elsewhere.[4] Briefly, a laser beam is focused on a GaAs/AlGaAs heterostructure sample immersed in an electrolyte which is contained in a small quartz cell. As a result, electron-hole pairs are generated and the holes are swept to the surface, causing the anodic dissolution of the semiconductor in the vicinity of the laser spot. By scanning the laser beam over the sample via computer-controlled translation stages, micrometer-scale trenches can be formed in the GaAs layer in any desired pattern. The resolution of the process is determined by the optical beam size and by the transport of the minority carriers in the semiconductor. The light source used in these experiments was an argon-ion laser operating at 275 nm and was focused with a microscope objective (16×, NA = 0.25) to a spot size of about 2 μm (full width at $1/e$ intensity).

An important consideration in device fabrication with this new technology is to have sufficient control of processing to build useful devices. For example, in order to allow flexible design of single-mode waveguides and the optoelectronic devices based on them, it is necessary to have sufficiently high resolution to allow close positioning of the trenches. This requirement presents a potentially serious problem since for waveguide applications free-carrier absorption limits the doping to low values ($\leq 10^{16}$ cm^{-3}). In addition, for the active devices discussed here, very low doping ($\approx 10^{14}$ cm^{-3}) is necessary in order to have a depletion width sufficiently large to allow penetration of the electric field into the region of the optical mode. This low doping level results in a long diffusion length for carriers in the solid (≥ 7 μm), thus making it difficult to obtain high resolution. In connection with our waveguide device research, we have studied electrochemical factors which influence the resolution of our process[5] and have been able to obtain high resolution at low doping. This result was achieved through the discovery of appropriate electrolytes which have sufficiently high chemical reaction rates without the use of an applied bias. The latter point is significant since the ability to perform electroless etching using these electrolytes greatly simplifies the fabrication process. The etchant we selected was $HCl:HNO_3:H_2O::4:1:50$.

3. FABRICATION AND CHARACTERISTICS OF RIB-LIKE WAVEGUIDES

The samples used in these experiments consisted of a vertically single-mode GaAs/$Al_{0.1}Ga_{0.9}As$ heterostructure grown by MOCVD on the (100) plane of a GaAs substrate. The thicknesses of the GaAs and AlGaAs layers were 1.3 and 2.7 μm, respectively, and their n-type doping concentrations were 10^{14} and 10^{16} cm^{-3}, respectively. In such a GaAs/AlGaAs

heterostructure, near infrared light is confined vertically within the higher refractive index of the GaAs layer. By etching two grooves partway through the GaAs layer on our sample, we laterally confine the light in the region between the grooves by virtue of the greater effective index of the unetched region compared with that of the etched region,[6,7] as in a conventional rib or ridge waveguide. The IR light used for testing was that of a 1.3-μm diode laser. At this wavelength, $n_{GaAs} = 3.4049$ and $n_{AlGaAs} = 3.3566$.

We have fabricated such rib-like waveguides and have measured their modal and loss properties as a function of geometric parameters.[1] We also described the basic characteristics of these unconventional groove-defined waveguides by simple analytical models using effective index theory.[1,8]

Observations of the mode structure were made by imaging the waveguide output onto an IR camera and viewing it on a TV monitor. In order to analyze the modal properties of these structures, several waveguides were fabricated with different trench depths and trench separations, and were classified as single-mode or multimode. We found that, as expected from theory, for shallow trench depth or small trench separation, single-mode operation is achieved. We found that for all but the deepest trenches, a trench separation of 6-8 μm generally yields a single-mode guide. Therefore, the trench separation was fixed at 7 μm, and several guides of different trench depths were fabricated in order to determine the waveguide loss versus etch depth for single-mode guides. By using the cutback method, we obtained the power transmitted by the waveguide as a function of waveguide length. This was done for several laser etching powers, yielding different trench depths. As the laser power is increased, yielding deeper trenches, the light is better confined. The waveguide loss decreased with deeper trenches and eventually reached a

minimum of 0.9 dB/cm, which is a suitably low value for integrated optics applications. For shallow trenches, the loss is dominated by radiation due to light tunneling through the finite-width etched region and propagating laterally into the exterior of the guide, while for sufficiently deep or wide trenches, the loss is limited by scattering due to surface roughness at the air/GaAs interface. In computing the scattering loss, it is necessary to consider potential contributions related to both vertical and lateral confinement. For our waveguides, simple estimates show that the vertical scattering loss dominates. This is essentially due to the fact that the index difference at the air/GaAs interface, which confines the light vertically, is much larger than the effective index difference between the etched and unetched regions, which produces lateral confinement. The calculation of the vertical scattering loss is complicated by the fact that at the air/GaAs interface, portions of the wave near the center of the guide see a surface roughness which is different from that near the etched trenches.

Furthermore, theoretical calculations showed that a wider etched region should yield lower radiation loss. Therefore, waveguides were fabricated using pairs of trenches (separated by 2 μm) on either side of the rib in order to create a wider etched region. The loss for such dual-trench waveguides was found to be reduced to only 0.6 dB/cm, in agreement with the trend predicted above. Note that an alternative means of creating the wider etched region might be to use appropriate optics to form a broader, rectangularly-shaped beam profile. Any further attempts to reduce the waveguide distributed loss would probably be limited by scattering at the air/GaAs interface; thus the deposition of a higher index overlayer on the GaAs would be expected to be important to further reduce losses.

Thus, low-loss lateral single-mode operation can be obtained by proper choice of etch

depth, etch width, and trench separation.

Several electro-optic devices, such as Mach-Zehnder-interferometer-based amplitude modulators and directional coupler switches, require various passive waveguiding structures such as tapers, bends, branches, and directional couplers. Such devices can easily be fabricated with our novel maskless technique.[1] Waveguide bend and branch loss has been measured and was found to be less than 1 dB for bend and branch angles less than 2°.

4. FABRICATION AND OPERATION OF ELECTRO-OPTIC DEVICES

A. Polarization Modulator

The first active device we fabricated was an electro-optic polarization modulator. The linear electro-optic effect is utilized in this device. The electrode configuration we used is that of a coplanar strip where the electrodes are 7 μm apart on either side of the waveguide, allowing an electric field to be applied within the waveguide core along the <011> direction.

The etched portion of the device was an 8.5-mm groove-defined straight waveguide. The separation between the etched trenches was 8 μm and the depth of the trenches was 0.8 μm. This waveguiding structure is single-mode and has a propagation loss less than 0.9 dB/cm without the metal electrodes.

The waveguide metallization was fabricated by a conventional deposition with laser direct patterning. The first step was the evaporation of a 1500-Å blanket of aluminum on the sample. This metal was then spin-coated with a layer of positive photoresist. By using low power (1 μW) UV laser-writing to pattern the photoresist, we were able to generate conveniently the electrode structure. In this step, an exposed line was formed along the center of the waveguide rib.

Developing the photoresist uncovered a 7 μm-wide strip of aluminum. The exposed aluminum was etched with heated H_3PO_4 without affecting the GaAs, and the remaining photoresist was stripped. An optical photograph showing a top view of the device and an SEM photograph of its cross section are shown in Fig. 1.

In order to test the device, we used a polarization-maintaining fiber to launch light polarized at 45° to the TE direction into the waveguide structure by butt-coupling the cleaved output facet of the fiber to one of the cleaved ends of the sample. By analyzing the output with an IR polarizer set at 90° to the input polarization, amplitude modulation was obtained. The experimental setup used to characterize the device is shown in Fig. 2. Figure 3 shows the transmission as a function of applied voltage, and demonstrates an extinction ratio of 17 dB and a V_π of 4 V. These characteristics are excellent, knowing that in general an extinction ratio of ~10 dB is considered sufficient[10] and that polarization modulators fabricated by more conventional means in GaAs do not exhibit better values for these operational characteristics.[11]

B. Amplitude Modulator Using an Integrated Polarizer

We can use the device described above in conjunction with an on-chip polarizer to build a simple, integrated amplitude modulator. Such a device has never been reported before.

The first fabrication steps of this device were similar to those that led to the polarization modulator described in the above paragraphs. The overall device length was 1 cm, 8 mm of which had electrodes for the polarization modulator, and the remaining length was for the positioning of a polarizer. The polarizing element was a thin metal film which is known to exhibit strong polarization-sensitive optical loss. In particular, the presence of the aluminum strip

allows selective TE_0 mode transmission, while the TM_0 mode and higher-order modes (which are not present in this single-mode structure) do not transmit through the guide. This filter action is explained by modal repulsion from the metal wall.[12] For our device, this element consisted of a 1-mm-long 20-μm-wide strip of aluminum positioned on top of the waveguide, in the center of the area with no electrodes.

In our experiments, laser-defined CVD[13,14] was used to form the polarizer. This technique was selected because it is maskless and discretionary. Thus the metallized region may be defined and adjusted without exposing the device to a second photopatterning step. It is a two-step process which allows the growth of aluminum films from a metallorganic source gas. In particular, the 275-nm light of the Ar^+ laser described above is used to generate a seed layer for selective chemical vapor deposition of aluminum at a temperature lower than that required for blanket growth. For this seeding step, the sample was mounted in a vacuum chamber filled to 1.0 Torr with dimethylaluminum hydride (DMA1H), and a very thin 1-mm-long aluminum line was direct-written by a process which is based on UV photolysis of the DMA1H adlayer. Subsequently, a pad of aluminum was grown in the desired area by exposing the sample, which had been elevated to 140°C, to a flowing stream of the organometallic gas. The electrodes were protected during this process with photoresist. Figure 4 shows a schematic diagram of the finished device.

Prior to fabricating this device, we studied the polarization-sensitive attenuating properties of the laser-defined aluminum lines. For this study, aluminum lines of various lengths (0.5-2.0 mm) were direct-written on straight waveguides, and the output intensity was measured as a function of the pad length and normalized to that of a straight waveguide with no aluminum.

This measurement was made for both TE and TM and the results are plotted in the inset of Fig. 5.

In order to test the device, we launched light polarized at TM into the waveguide structure. Fig. 5 shows the transmission as a function of applied voltage, and exhibits an extinction ratio of 13 dB and a V_π of 6 V. Again, those operational characteristics are more than adequate for integrated optical applications.[10] The extinction ratio obtained is in accordance with the value we expected from the preliminary studies of the attenuating properties of the aluminum lines, as can be seen in the Fig. 5 inset where the difference between the TE and TM attenuations is about 13 dB for a 1 mm aluminum line.

Furthermore, improvements could be achieved in the above characteristics if a dielectric were used for the on-chip polarizer instead of aluminum. An example of such a dielectric is calcite ($CaCO_3$) which has been used as a polarizing element on top of K^+ ion-exchanged glass waveguides.[15] The effective index of the guided mode is lower than the calcite index for ordinary waves and higher than the calcite index for extraordinary waves. With the optical axis of calcite lying along the polarized direction of the TE mode, the TE mode can propagate in the waveguide without leakage, while the TM mode leaks into the calcite. This type of polarizer has the advantage of a smaller insertion loss when compared with the aluminum polarizer. Moreover, a higher extinction ratio can be expected.

C. Mach-Zehnder Modulator

Mach-Zehnder interferometers (or Y branch modulators) have been very popular amplitude modulators in integrated optics because of their apparent simplicity compared to other common

modulator structures such as balanced bridge and directional-coupler-based modulators.[9] In addition, since they rely on the interference between two beams to produce modulation, they do not cause unnecessary attenuation in the signal the way on-chip polarizers can. However, a much complex and accurate writing sequence is required in the fabrication process.

The principle of operation of this modulator is quite simple. Basically, an input wave splits into equal components which propogate along the two arms of the interferometer. If no phase shift is introduced between the arms, the two components combine in phase at the output Y-branch 3-dB combiner and continue to propagate undiminished in the output waveguide; this corresponds to a maximum in the transmitted light. For a π phase shift, the field distribution after the output Y-branch corresponds to the second-order mode of the output single-mode waveguide, and hence the light is radiated into the substrate; this corresponds to a minimum in the transmitted light.

The electrode configuration we used is again that of coplanar strips where the electrodes are 7 μm apart on either side of each of the two parallel arms, allowing an electric field to be applied along the <011> direction within the waveguide core of each arm. Since a central electrode can be shared by both guides, a total of three electrodes are required for this device.

Again, we used our computer-controlled direct-writing technique to fabricate the passive part of the device. The structure consisted of a 2-mm input waveguide, a 1-mm 4°-full-angle Y-branch 3-dB splitter, two 6-mm parallel waveguide arms which are sufficiently separated to prevent evanescent coupling between them, a 1-mm 4°-full-angle Y-branch 3-dB combiner, and finally a 2-mm output waveguide. The waveguides were etched with 7-μm separation between the trenches to insure single-mode operation. Subsequently, a 1500-Å layer of aluminum was

evaporated through a shadow mask that defined the region of the sample where we wanted the electrodes to be positioned. Special attention was paid to providing a bonding pad to the electrode positioned in between the two arms, although that would cause the presence of a small aluminum "bridge" over one of the arms, which would introduce some undesirable but unavoidable loss in that arm due to fast carrier absorption. However, the width of that "bridge" can easily be minimized. We decided to position the pad for the central electrode at the lower-right corner of the sample.

Subsequently, the sample was spin-coated with a layer of positive photoresist. Again, we used our UV laser-writing apparatus to pattern the photoresist. We exposed a line along the center of the top waveguide rib, a line along the center of the bottom waveguide rib which stops just short of the end of that guide (leaving space for the "bridge"), and another line from the end of the bottom line to the lower end of the sample perpendicularly to the two previous lines. The photoresist was subsequently developed, uncovering the strips of aluminum to be etched. We again used heated H_3PO_4 to selectively etch the aluminum. Finally, after stripping the photoresist, we obtained three electrodes allowing an electric field to be applied within the waveguide core of both arms. A schematic showing clearly the fabrication steps is shown in Fig. 6, and an optical photograph of the device is shown in Fig. 7.

In order to test the device, we launched light polarized at 45° to the TE direction into the input waveguide. The two outer electrodes were connected to ground and the central electrode was connected to a positive voltage. The application of a voltage across the two arms lead to the expected modulation of the amplitude. Fig. 8 shows the transmission as a function of applied voltage, and demonstrates an extinction ratio of 15 dB and a V_π of 5 V. These values are

comparable to or better than those exhibited by Mach-Zehnder interferometers fabricated by more conventional techniques in GaAs,[16-18] in Ti:$LiNbO_3$,[19] and in polymers.[20]

5. CONCLUSION

In summary, the technique of laser-induced photoelectrochemical etching which has been shown in the past to be useful in the fabrication of low-loss single-mode passive devices and structures is shown here to be very effective in the fabrication of active waveguiding devices. In particular, we fabricated a polarization modulator, an amplitude modulator consisting of a polarization modulator and an integrated polarizer, and a Mach-Zehnder interferometer. These devices show high extinction ratios and low values of V_π. These results indicate that our process offers a novel means for rapidly fabricating integrated optic device structures, and its maskless nature makes it a useful tool for prototyping integrated optic circuits.

Finally, the techniques and devices discussed in this paper are being used to fabricate large scale integrated optic circuits including optical delay lines, switching arrays, and wavelength demultiplexers.

This work was supported by the Defense Advanced Research Projects Agency under the Air Force Office of Scientific Research, the National Center for Integrated Photonic Technology, and the Army Research Office.

6. REFERENCES

1. L. Eldada, M.N. Ruberto, R. Scarmozzino, M. Levy, and R.M. Osgood, Jr., "Laser-Fabricated Low-Loss Single-Mode Waveguiding Devices in GaAs," IEEE J. Lightwave Technol. LT-10, 1610 (1992).

2. M. Levy, L. Eldada, R. Scarmozzino, R.M. Osgood, Jr., P.S.D. Lin, and F. Tong, "Fabrication of Narrow-Band Channel-Dropping Filters," Photonics Technol. Lett. 4, 1610 (1992).

3. R. Scarmozzino, D.V. Podlesnik, and R.M. Osgood, Jr., "Losses of Tapered Dielectric Slab Waveguides with Axial Variations in Index of Refraction," IEEE Trans. Microwave Theory Tech. MTT-38, 141 (1990).

4. M.N. Ruberto, X. Zhang, R. Scarmozzino, A.E. Willner, D.V. Podlesnik, and R.M. Osgood, Jr., "The Laser-Controlled Micrometer-Scale Photoelectrochemical Etching of III-V Semiconductors," J. Electrochem. Soc. 138, 1174 (1991).

5. S. Li, G. Scelsi, M.N. Ruberto, R. Scarmozzino, and R.M. Osgood, Jr., "Factors controlling the resolution in the laser-induced aqueous etching of semiconductors using a focused cw beam," Appl. Phys. Lett. 59, 1884 (1991).

6. A.E. Willner, M.N. Ruberto, D.J. Blumenthal, D.V. Podlesnik, and R.M. Osgood, Jr., "Laser Fabricated GaAs Waveguiding Structures," Appl. Phys. Lett. 54, 1839 (1989).

7. M.N. Ruberto, R. Scarmozzino, A.E. Willner, D.V. Podlesnik, and R.M. Osgood, Jr., "Graded-Effective-Index Waveguiding Structures Fabricated with Laser Processing," SPIE Proc. 1215, 538 (1990).

8. R. Scarmozzino, D.V. Podlesnik, A.E. Willner, and R.M. Osgood, Jr., "Modeling of rib-

like waveguides with isolation trenches of finite width," Appl. Opt. 28, 5203 (1989).

9. R. Alferness, "Waveguide Electrooptic Modulators," IEEE Trans. Microwave Theory Tech. MTT-30, 1121 (1982).

10. R. Alferness, "Guided-Wave Devices for Optical Communication," IEEE J. Quantum Electron. QE-17, 946 (1981).

11. S. Wang and S. Lin, "High Speed III-V Electrooptic Waveguide Modulators at λ = 1.3 μm," IEEE J. Lightwave Technol. LT-6, 758 (1988).

12. Y. Suematsu, M. Hakuta, K. Furuya, K. Chiba, and R. Hasumi, "Fundamental Transverse Electric Field (TE_0) Mode Selection for Thin-Film Asymmetric Light Guides," Appl. Phys. Lett. 21, 291 (1972).

13. T. Cacouris, G. Scelsi, P. Shaw, R. Scarmozzino, R.M. Osgood, Jr., and R.R. Krchnavek, "Laser Direct Writing of Aluminum Conductors," Appl. Phys. Lett. 52, 1865 (1988).

14. N. Zhu, T. Cacouris, R. Scarmozzino, and R.M. Osgood, Jr., "Patterned Metal Growth from Dimethylaluminum Hydride," J. Vac. Sci. Technol. B 10, 1167 (1992).

15. S. Uehara, T. Izawa, and H. Nakagome, "Optical Waveguide Polarizer," Appl. Opt. 13, 1753 (1974).

16. M.A. Khan, A. Naumaan, and J.M. Van Hove, "Integrated Optics Intensity Modulators in the GaAs/AlGaAs System," SPIE Proc. 1396, 753 (1990).

17. R.G. Walker, "High-Speed III-V Semiconductor Intensity Modulators," IEEE J. Quantum Electron. QE-27, 654 (1991).

18. M. Erman, P. Jarry, R. Gamonal, P. Autier, J. Chané, and P. Frijlink, "Mach-Zehnder Modulators and Optical Switches on III-V Semiconductors," IEEE J. Lightwave Technol.

LT-6, 837 (1988).

19. J. Jackel, P. Perlmutter, and J. Johnson, "High-Speed Low-Voltage Modulation with a Nonsymmetric Mach-Zehnder Interferometer," IEEE J. Lightwave Technol. LT-7, 937 (1989).

20. G. Möhlmann, W. Horsthuis, J. Mertens, M. Diemeer, F. Suyten, B. Hendriksen, C. Duchet, P. Fabre, C. Brot, J. Copeland, J. Mellor, E. Van Tomme, P. Van Daele, and R. Baets, "Optically Nonlinear Polymeric Devices," SPIE Proc. 1560, 426 (1991).

Figure Captions:

1. Polarization modulator seen (a) under an optical microscope (top view) and (b) under a scanning electron microscope (cross section).
2. Setup used for the characterization of electro-optic devices.
3. Transmission factor vs. applied voltage for the polarization modulator (extinction ratio = 17 dB, V_π = 4 V, length = 8.5 mm).
4. Schematic diagram of the integrated amplitude modulator consisting of a polarization modulator and an on-chip polarizing element. The polarizer is a 1-mm-long 20-μm-wide strip of aluminum which allows selective TE_0 mode transmission.
5. Transmission factor vs. applied voltage for the integrated amplitude modulator (extinction ratio = 13 dB, V_π = 6 V, electrode length = 8.0 mm). The inset shows the results of a study of the polarization-dependent attenuating properties of laser-defined aluminum lines; the attenuation of both TE and TM-polarized light is plotted vs. the length of the aluminum pad.
6. Steps of fabrication of the Mach-Zehnder interferometer.
7. Optical photograph of the Mach-Zehnder interferometer.
8. Transmission factor vs. applied voltage for the Mach-Zehnder interferometer (extinction ratio = 15 dB, V_π = 5 V, electrode length = 5.5 mm).

Figure 1

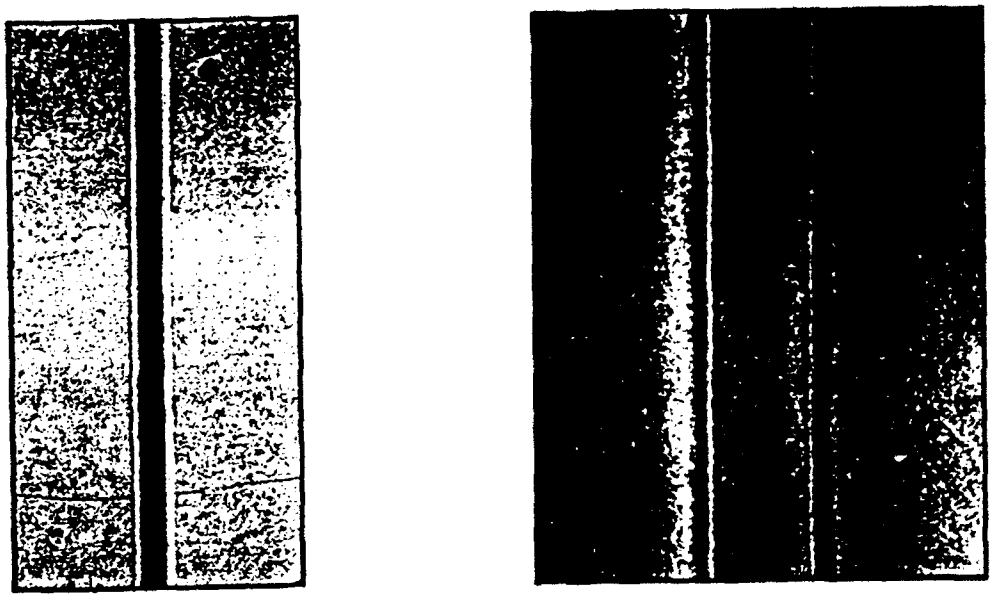

(a)

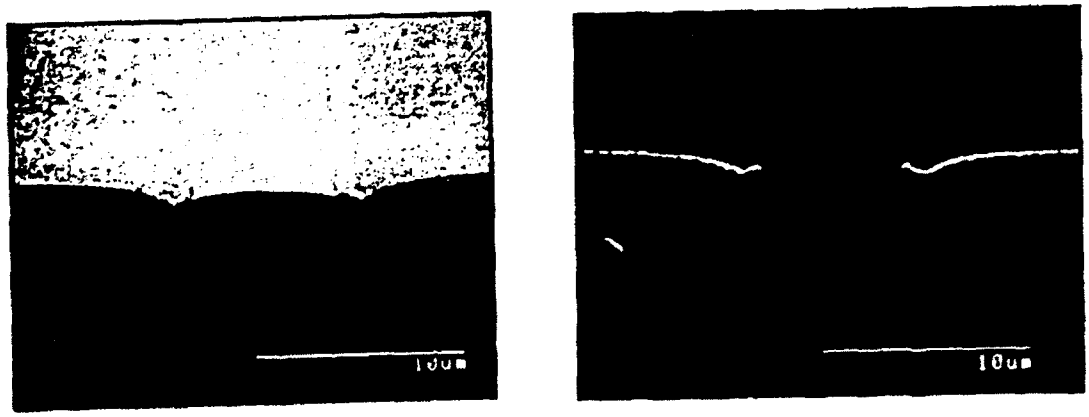

(b)

Figure 2

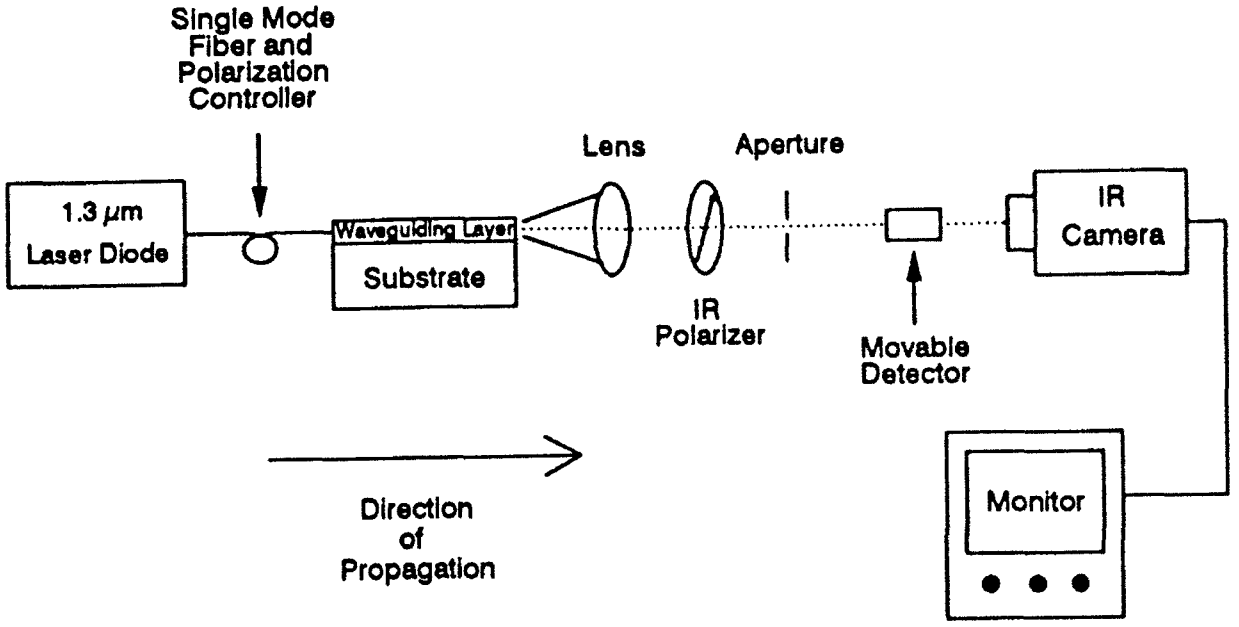
Single Mode
Fiber and
Polarization
Controller
1.3 μm
Laser Diode
Waveguiding Layer
Substrate
Lens
Aperture
IR
Polarizer
Movable
Detector
IR
Camera
Monitor
Direction
of
Propagation

Figure 3

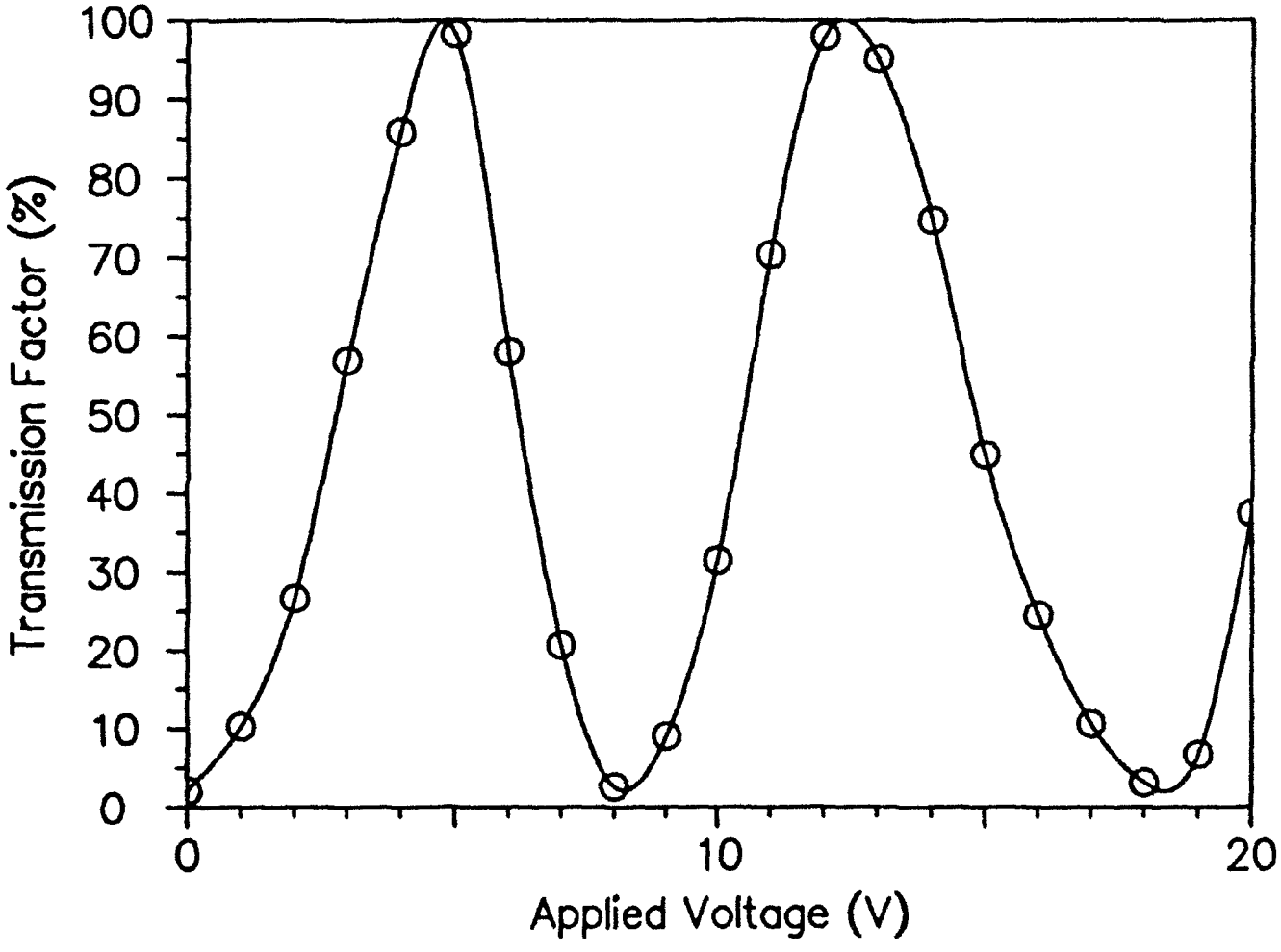
Transmission Factor (%)
100
90
80
70
60
50
40
30
20
10
0
0
10
20
Applied Voltage (V)

Figure 4

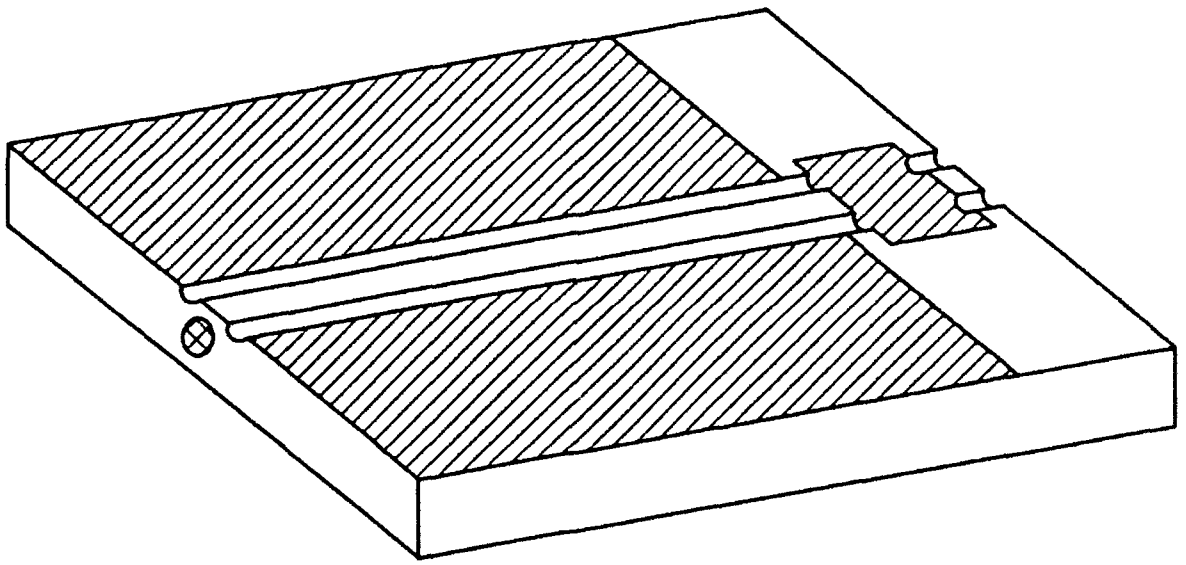

Al

Figure 5

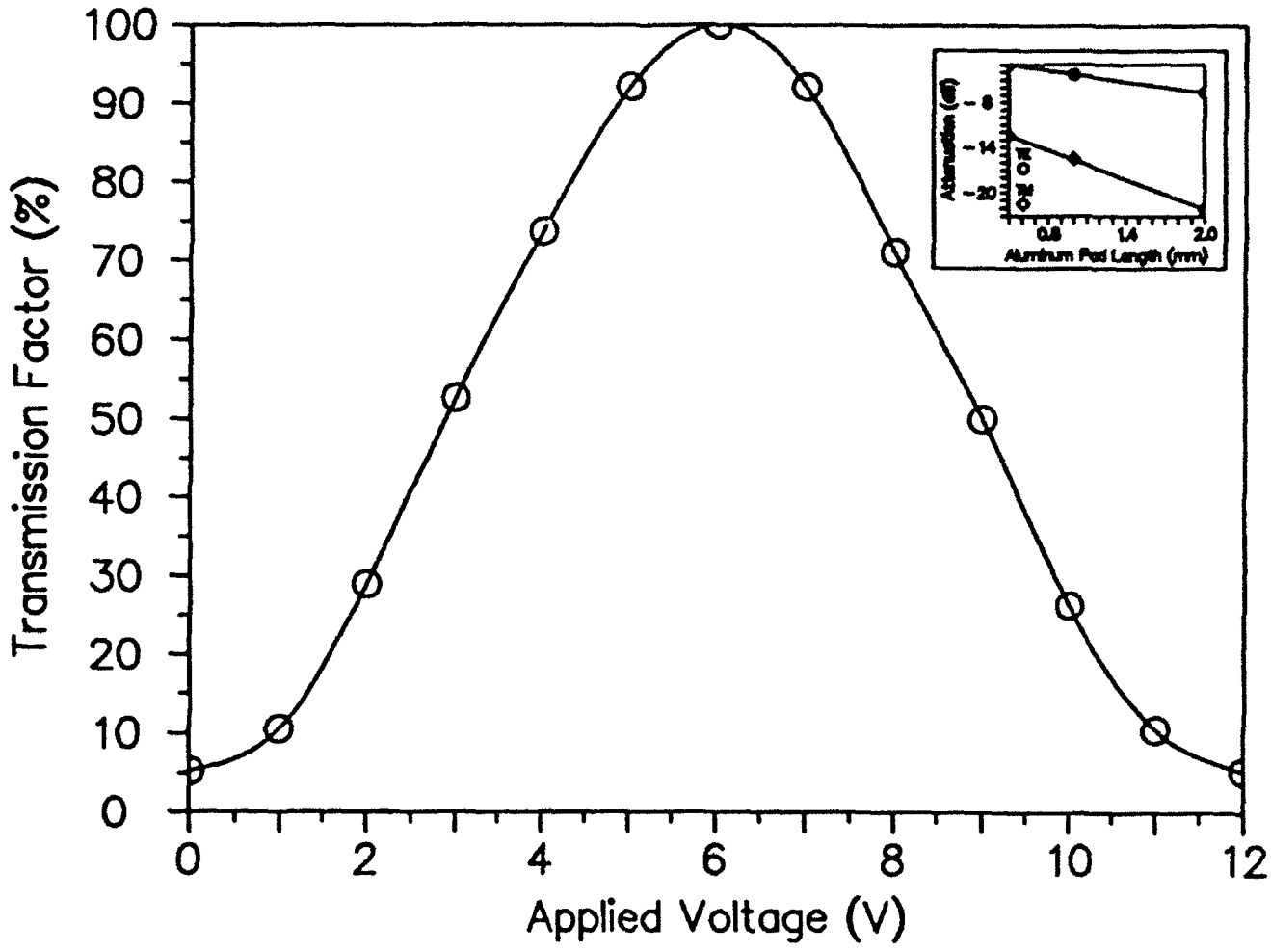
Transmission Factor (%)
100
90
80
70
60
50
40
30
20
10
0
0
2
4
6
8
10
12
Applied Voltage (V)
Attenuation (dB)
-8
-14
-20
0.8
1.4
2.0
Aluminum Pad Length (mm)

Figure 6

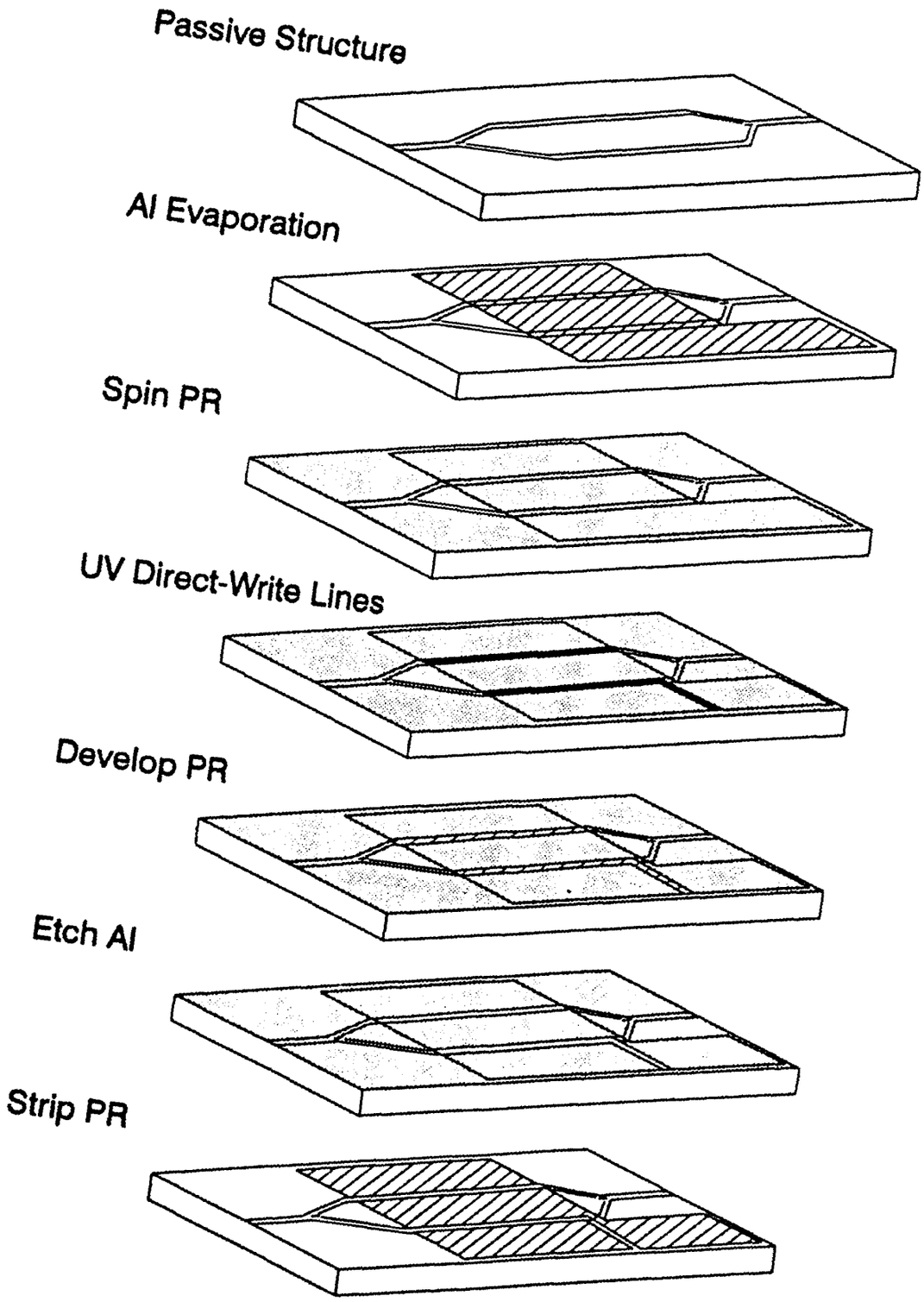
Passive Structure
Al Evaporation
Spin PR
UV Direct-Write Lines
Develop PR
Etch Al
Strip PR

Figure 7

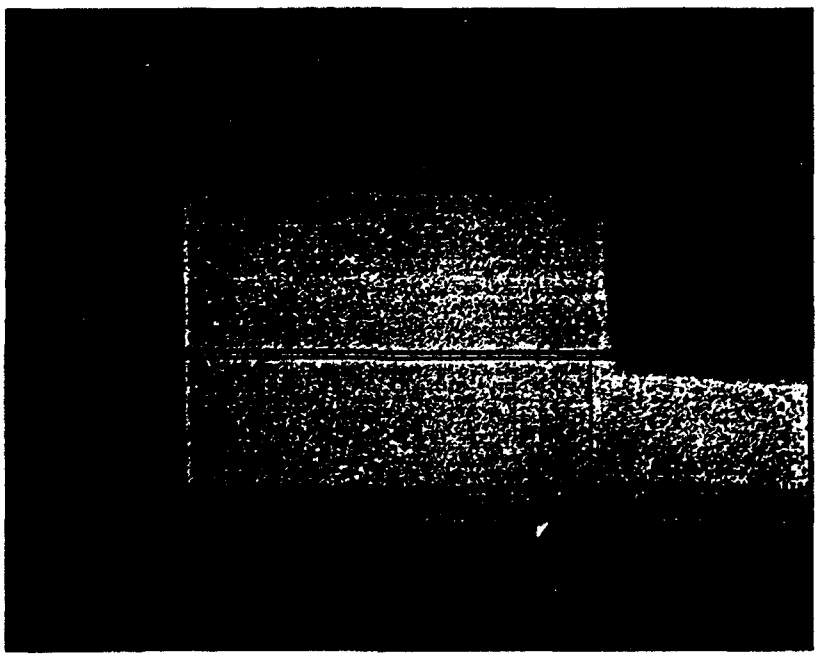

Figure 8

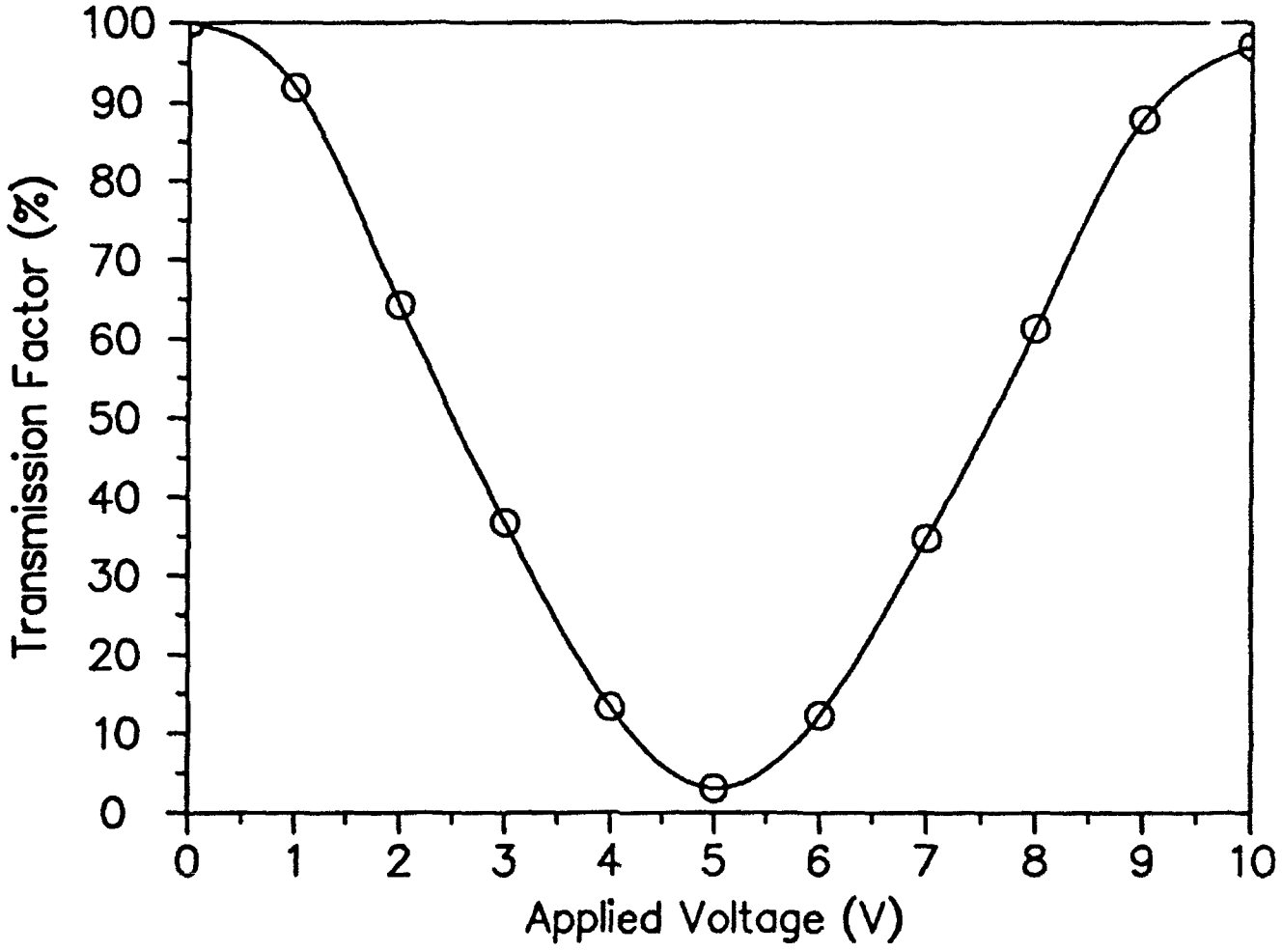
Transmission Factor (%)
100
90
80
70
60
50
40
30
20
10
0
0
1
2
3
4
5
6
7
8
9
10
Applied Voltage (V)

EXCIMER LASER INDUCED CRYOETCHING OF GaAs AND RELATED MATERIALS

Michael B. Freiler, Ming Chang Shih, R. Scarmozzino, R. M. Osgood Jr., Ie Wei Tao, and Wen I. Wang

Microelectronics Sciences Laboratories, Columbia University, New York, NY 10027

ABSTRACT

We report highly resolved, damage-free etching of GaAs and related materials. The etching is activated by excimer laser irradiation at 193 nm of samples maintained at low temperatures (~140 K) in a chlorine atmosphere (~5 mTorr). Since the etching is chemical in nature, structural damage to the substrate should not be present. Submicrometer resolution has been achieved by the use of electron beam lithography to pattern a Si_3N_4 contact mask. We have also successfully used our etching in the fabrication of a single-quantum-well, ridge-waveguide semiconductor laser.

INTRODUCTION

In-situ, anisotropic, damage-free etching techniques are becoming increasingly important for advanced device technology. Plasma etching techniques such as reactive ion etching, ion beam etching, and chemically assisted ion beam etching all have a significant amount of damage due to energetic particle bombardment of the sample surface. This bombardment causes structural and chemical damage to the underlying substrate material, degrading its electrical and optical properties.[1-3] Studies of these techniques indicate the extent of this damage may be minimized, but not totally eliminated, without severely reducing the device etch rate. Damage-free, anisotropic wet etching techniques may also used, but they tend to be crystallographically determined, thus severely limiting geometries of etched structures.

Our etching process is based on a study of the interaction of physisorbed chlorine and GaAs (110) samples at low temperatures.[4] In this study, it was found that there was no spontaneous etching between adsorbed Cl_2 and GaAs at 85 K, but irradiation with an excimer laser at low fluences caused the appearance of reaction products ($AsCl_3$ and Ga) in Temperature Programmed Desorption (TPD) spectra. They also showed that 193 nm radiation was more efficient by a factor of 20 in the creation of products than 248 nm or 350 nm wavelength radiation, which is consistent with the absorption spectrum of condensed chlorine as measured by Cousins and Loene,[5] which showed a significant absorption peak centered at about 200 nm. This strong absorption peak has been interpreted as being due to the formation of a charge transfer complex between neighboring condensed chlorine molecules.[4]

Our etching technique has been previously reported.[6] Briefly, a GaAs sample is maintained at low temperature in a chlorine atmosphere. These conditions result in the physisorption of chlorine in the monolayer regime. The sample is irradiated at 193 nm, causing the dissociation of the chlorine molecules into reactive chlorine atoms, by the mechanism mentioned above. The laser pulse also induces desorption of the etching products, resulting in material removal. Each laser pulse removes a small fraction of a monolayer from the surface. Anisotropic etching has been observed and the etch rate characterized as a function of the sample temperature, chlorine pressure, and laser fluence and repetition rate and related to the a model of multilayer physisorption using the BET (Brunauer-Emmett-Teller) formulation.

The anisotropy results from many factors. Primarily, it is due to the reduction or

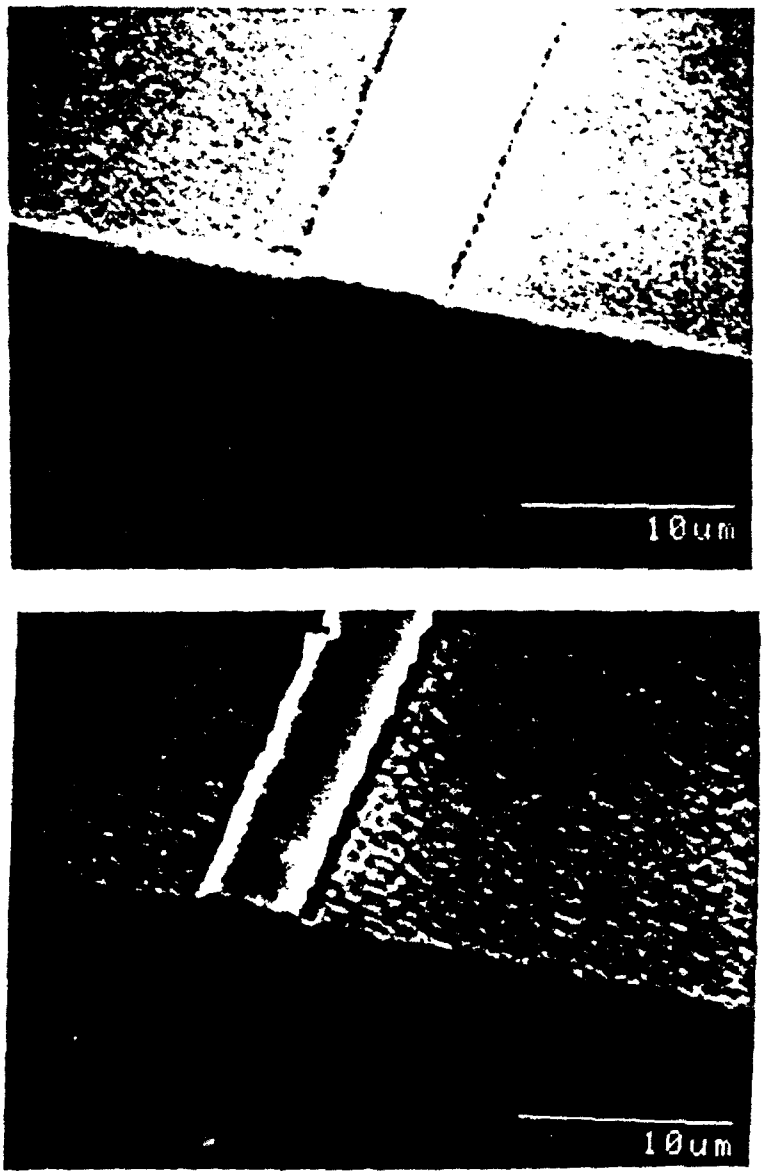

Figure 1. Etching of GaAs (100) with gold surface mask; 140 K, 5 mTorr Cl_2; Approximate etch depth: 0.25 μm (Top); 0.5μm (Bottom).

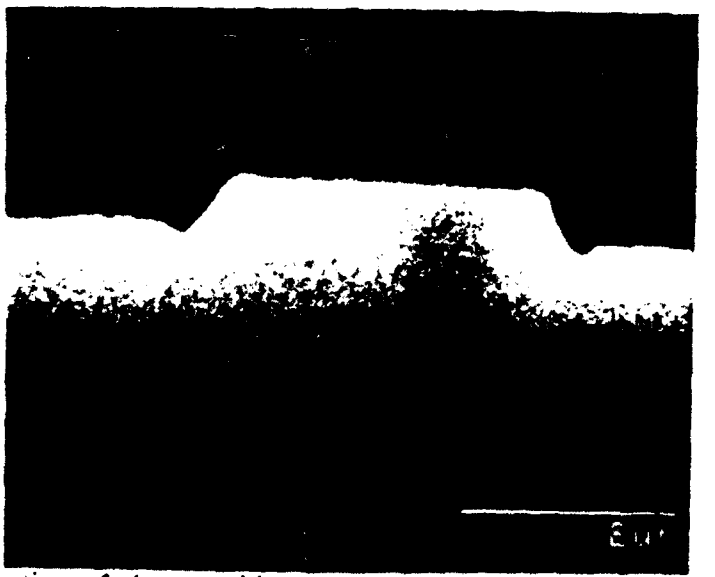

Figure 2. Cross Section of above etching: Larger etched depth sample

elimination of spontaneous etching by gas phase molecules at low temperatures, which would cause etching of the sidewalls, leading to undercutting. This effect has been shown for etching processes stimulated by ion,[7] electron,[8] and photon[6] beams. Anisotropy also results from the confinement of both the reactive species production and reaction product desorption to the illuminated zone, and from the fact that the laser intensity is weaker on the sloped sidewalls due to the oblique angle of incidence.

EXPERIMENT

Our etching apparatus has been previously described.[6] The chamber attains a base pressure of 10^{-7} Torr, but during etching was operated with a Cl_2 gas flow. During experiments, the sample was maintained at temperatures of 120 K to 200 K in a atmosphere with a chlorine partial pressure of 0 - 20 mTorr. The sample was introduced by a load-locking system, which enables the rapid transfer of our samples without exposing the etch chamber to atmospheric moisture. This moisture resulted in a rougher surface morphology, especially in the etching of $Al_xGa_{1-x}As$. After the sample was loaded into the exchange chamber, it was heated to 473 K for 10 minutes to melt the indium foil which is used to achieve good thermal contact between the GaAs sample and the cooling block. This preheating process also helped to remove moisture on the surface to be etched.

In our experiments, we used a Lambda Physik 130i excimer laser running with an ArF (193 nm) mix. The laser beam was concentrated along the horizontal axis by using cylindrical optics placed near the laser. An aperture was used to select a uniform area of the beam, and this aperture was imaged onto the sample surface with a long focal length spherical lens using 1:1 projection. By imaging the beam profile near the laser output, this arrangement allows us to achieve uniform illumination. For our experiments, fluences in the range of 10 - 30 mJ/cm^2 were used. These fluences result in a moderate temperature rise of the sample surface and thermal effects were minimal.[6] In these experiments, we were able to achieve etch rates of 0.25 Å/pulse (0.9 μm/min. at 60 Hz.)[6]. There is no measurable etching in areas not exposed to the laser light.

To demonstrate the pattern transfer capability of this etching technique, we initially used a gold surface mask patterned by optical lift-off lithography. Figure 1 shows the surfaces of n-type (~3 x $10^{17}/cm^3$) GaAs (100) samples etched with a sample temperature of 140 K in a Cl_2 pressure 5 mTorr and at a laser fluence of 20 mJ/cm^2. The sample in the top photo has an etch depth of about 0.25 μm and the one in the bottom photo has an etch depth of about 0.5 μm. Notice that the etched surface starts out with a smooth finish, then roughens noticeably as the etch depth increases. Figure 2 shows a cross section at the deeper etch depth. The sidewalls are sloped outward and there is a small trench at the bottom of these walls. We believe that this trench is due to a combination of Fresnel diffraction with guiding of the light down the sidewalls. We have explored the etching of features with various orientations on the GaAs (110) surface and found that they all show similar sidewall slopes, which are also close to the slopes for GaAs (100) samples. Such sidewalls, which typically have a fluence dependent angle, are generally characteristic of laser etching.

Gold surface masking by optical lift-off lithography is not suitable for high resolution studies of this etching. It is limited in the resolution it can obtain due to the limits of optical lithography and the difficulty of executing submicrometer patterning using lift-off methods for masks as thick as we require (> 0.1 μm). Another problem with Au surface masks appears to be mask integrity, since the gold mask often erodes near the edges.

To achieve high-resolution patterning, we used a Si_3N_4 surface mask patterned by electron beam lithography followed by reactive ion etching. The material is chemically inert in a chlorine atmosphere and strongly adsorbs in the deep ultraviolet. Also, it can be deposited

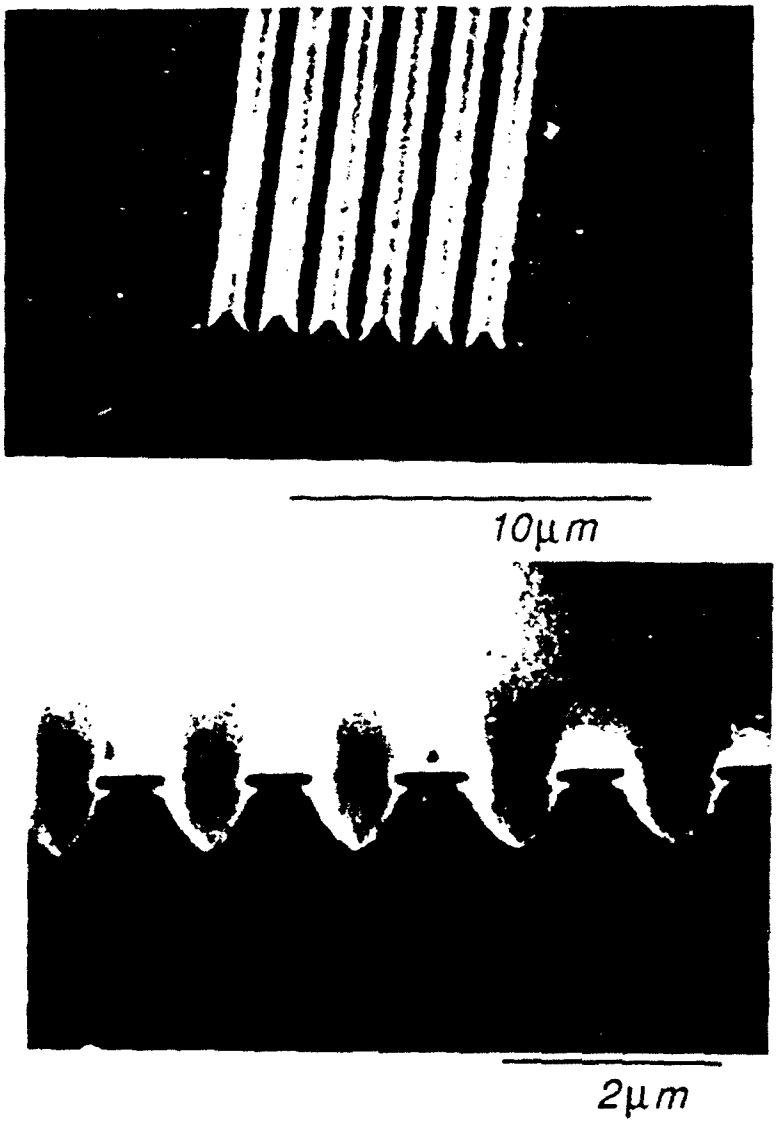

Figure 3. Submicrometer etching of GaAs (110) with Si_3N_4 mask; 140 K, 5 mTorr Cl_2.

on our substrates using plasma enhanced chemical vapor deposition; high resolution pattern transfer is by reactive ion etching using commercially available equipment with a resist mask. The samples used in the submicrometer etching reported here were patterned by the National Nanofabrication Facility at Cornell University, Ithaca, NY.

Figure 3 shows submicrometer etching of GaAs (110) surfaces. The etch depth is 0.85 μm and the line and space widths are 0.6 μm. The submicrometer pattern has been successfully transferred to the substrate and that the etch mask is largely intact. The walls are sloped outward and there is a bit of an undercut. The origin of this undercut is not well understood and it currently being investigated. Recent experiments indicate that this undercut may be reduced by lowering the sample temperature during etching. In other experiments, GaAs (100) samples etched to submicrometer dimensions with Si_3N_4 masks show almost the same behavior.

To demonstrate the capability of using this etching technique for device fabrication, we fabricated a mesa for a single-quantum-well, ridge-waveguide laser. The structure of the laser material is shown in Figure 4. Figure 5 is a top view and a cross-sectional view of the structure, showing sharp sidewall slope. The morphology is good enough for post processing steps such as SiO_2 and ohmic contact deposition. Because it is necessary to etch to within 0.1

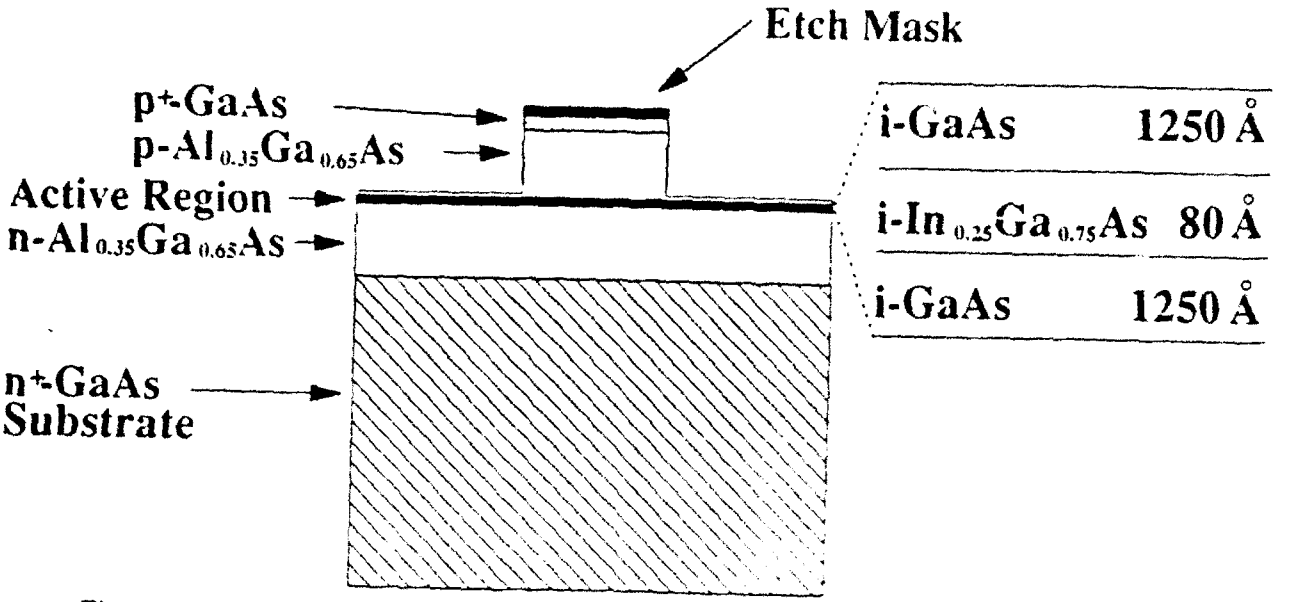

Figure 4. Structure of single-quantum-well, ridge waveguide semiconductor laser.

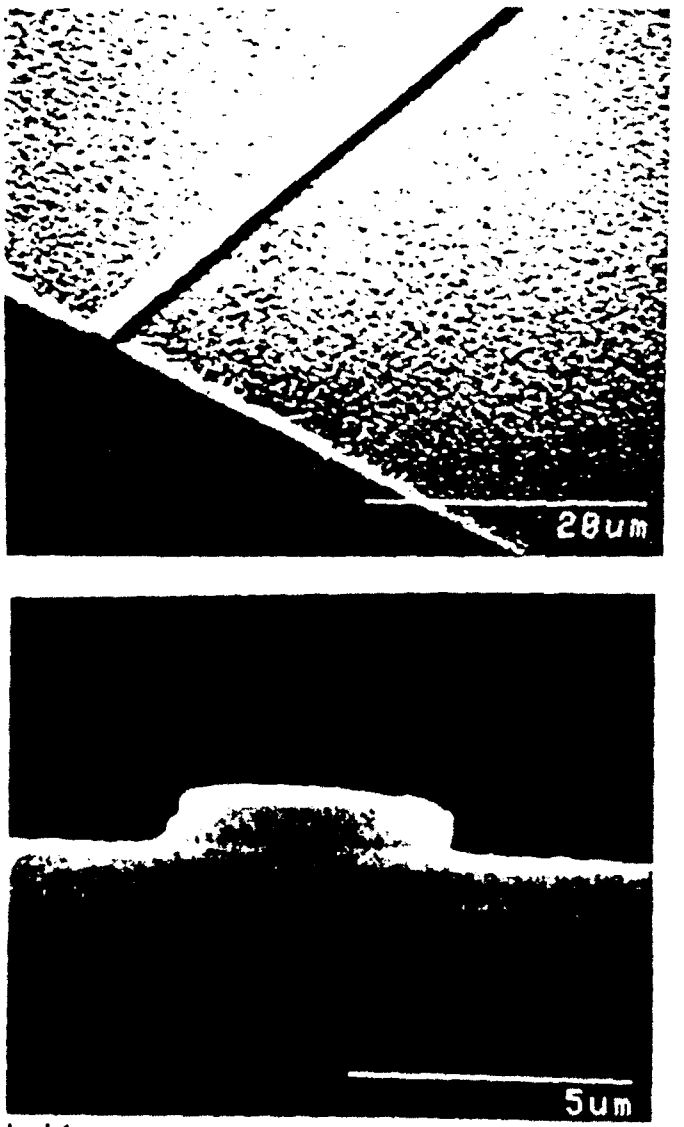

Figure 5. Etched laser structure; 140 K, 5 mTorr Cl_2.

μm above the 2580 Å active region, it is also important the etch depth be very uniform and well controlled. From our experiments, we found that the most important factor influencing the uniformity of the etch depth is the uniformity of the laser beam. Since the laser width is 4 μm, sidewall damage may play a critical role in device performance. The L-I (light out - current in) characteristics of the laser etched by this method are comparable the those obtained for lasers etched using conventional wet processing.

CONCLUSIONS

We have demonstrated smooth etching with submicrometer resolution. Since this technique does not use energetic particle bombardment, we anticipate that it will not damage the substrate material, causing the degradation of the sample's electrical or optical properties. Because of the ability to remove a small fraction of a monolayer per laser pulse, we have achieved excellent etch depth control, repeatedly etching to within 1000 Å of the desired etch depth for depths of over 1 μm. We have shown etching of the (110) and (100) surfaces of GaAs as well as $Al_{0.3}Ga_{0.7}As$, and, in recent experiments, of $Al_{0.7}Ga_{0.3}As$. The first device application for this etching was for fabrication of a mesa for a ridge waveguide laser. Current studies on this technique include probing for damage to the etched surface through characterization of a Shottky barrier grown on the etched surface and further exploration of factors influencing sidewall geometry.

ACKNOWLEDGMENTS

This research is funded by DARPA/AFOSR. The authors appreciate the valuable help we received from the National Nanofabrication Facility for patterning these samples.

REFERENCES

1. A. Sherer, H. G. Craighead, M. L. Roukes, and J. P. Harbison, J. Vac. Sci. Technol. **B6**, (1988).
2. S. Pang, G. A. Lincoln, R. W. McClelland, P. D. DeGraff, W. M. Geis, and W. J. Piacentini, J. Vac. Sci. Technol. **B1**, 1334 (1983).
3. H. F. Wong, D. L. Green, T. Y. Liu, D. G. Lishan, M. Bellis, E. L. Hu, P. M. Petroff, P. O. Holtz, and J. M. Mertz, J. Vac. Sci. Technol. **B6**, 1906 (1988).
4. V. Liberman, G. Haase, and R. M. Osgood, Jr., J. Chem. Phys. **96**, 1590 (1992).
5. L. M. Cousins and S. R. Leone, Chem. Phys. Lett. **155**, 162 (1989).
6. M. B. Freiler, Ming Chang Shih, G. Haase, R. Scarmozzino, and R. M. Osgood, Jr., Mater. Res. Soc. Proc. **236**, 15 (1991) and M. C. Shih, M. B. Freiler, G. Haase, R. Scarmozzino, and R. M. Osgood, Jr., Appl. Phys. Lett. **61**, 828 (1992).
7. S. Tachi, K. Tsujimoto, and S. Okuddaira, Appl. Phys. Lett. **55**, 91 (1989).
8. Heiji Watanabe and Sinji Matsui, Jpn. J. Appl. Phys. **31**. L810 (1992).

subm. to
J. Electrochem. Soc
8/14/92

Photoelectrochemical Etching of GaAs/AlGaAs Multilayer Structures

Th. Fink and R. M. Osgood, Jr.

Microelectronics Sciences Laboratories, Columbia University,

500 West 120th Street, New York, NY 10027

Abstract

A study of photoelectrochemical etching of AlGaAs/GaAs multilayers under conditions of constant potential or constant current is presented. It is shown that the etch rate changes as the process proceeds vertically through the layered sample. In addition, when the etching front crosses the interface between two epilayers a transient reduction in the etch rate is seen. These observations can be explained by the energy band structure of the heterojunction interface, including the presence of the quasi-two-dimensional electron gas at such an interface. The changes in potential or current at the interface can be used to form in-situ process diagnostics during the etching of multilayer samples. Finally, the morphology of the etched area and the profile of the etch feature have been investigated. The results show that etch-induced roughness is an important limitation on processing structures with very thin layers.

1. Introduction

Various techniques have been developed for fabricating optoelectronic and microelectronic devices and circuits including wet-chemical, ion beam and plasma etching [1,2]. Photoelectrochemical etching is a relatively new technique in semiconductor processing [3-8] which possesses many of the advantages of wet etching, including lack of etch-induced damage and material selectivity. In addition to conventional wet-etching techniques which have uniform etch rates across the wafer and thus require a photoresist mask for patterning, photoelectrochemistry allows resistless light-defined patterning as well as light-contoured etching. In addition, highly localized etching can be achieved by illuminating, with patterned light, only those parts of the surface where etching is desired. Important applications of light-induced etching in device fabrication have been demonstrated for microlenses, waveguides and waveguide devices, diffraction gratings, lasers, and through-wafer via formation [9-16].

Although the electrochemistry of semiconductors under illumination is well understood [17,18], and photoelectrolysis [19], photovoltaic behavior [20], photocorrosion and photodecomposition [21] as well as light-sensitive etching of semiconductors [22-24] have been studied in great detail, only a few reports of wet-chemical etching of heterostructures are available, and these reports deal almost exclusively with the selectivity of the process for layers of different semiconductors [2,14,25-27]. In addition, there appears to be no clear understanding of the electrochemical behavior of heterojunctions in contact with an etching electrolyte. In particular, the electrochemistry is complicated not only by the different materials on both sides of the junction but also by the effects of interfacial mobile charge and potential barriers [26].

This work presents experiments on the light-induced etching of various GaAs/AlGaAs heterostructures that give insight into the electrochemical processes near a heterojunction interface. Our experiments show that the band structure of the interface strongly affects the etching of the sample. In addition, we found that the uniformity of the etch profile can be optimized when the etching is performed with strong anodic potential. Fast etching of relatively low conductivity epilayers could be achieved by means of a side contact to the multilayer sample which uses the two-dimensional electron gas at the heterojunctions and produces increased etch currents. Finally, our results suggest that electrochemical methods can be used for *in situ* process diagnostics of the etching of multilayer structures. For such thin, layered structures it is important to etch a sample uniformly layer by layer and thus an *in situ* monitoring technique is essential.

2. Experimental

The experiments were performed in a typical electrochemical cell using a three-electrode configuration (Fig. 1). The multilayer samples were contacted with an evaporated AuGe film on the backside and encapsulated in black wax (Apiezon Type W) to ensure that only the exposed surface was in contact with the electrolyte. External voltages were applied between the sample and a counter electrode made from a platinum wire. The potential of the sample was measured versus a saturated calomel reference electrode, which was connected to the electrochemical cell via a salt bridge. A potentiostat allowed photoetching of the sample in two modes: at constant potential and at constant current. The time constant of the potentiostat was less than 0.1 s, which was adequate for following voltage or current changes for the etch rates examined here. Under

typical experimental conditions, i. e. photoanodic etching with external voltage, the response time of the electrochemical cell to potential changes was less than 0.5 s. Again, this time constant is sufficiently short to allow the etching process to be monitored.

Local illumination of the sample was achieved by imaging a homogeneously illuminated aperture of typically 400-µm diameter onto the surface by means of a single lens. The light source was a 150-W halogen lamp which allowed intensities of up to 250 mW/cm^2. This setup had the advantage that the light intensity within the illuminated spot is spatially uniform and, thus, produced a homogeneous etch rate over the entire spot. Moreover, by using differently shaped apertures, any desired pattern could easily be projected onto the surface.

The multilayer samples were MBE grown and consisted of several epilayers of n-GaAs and n-$Al_{0.3}Ga_{0.7}As$ ($n = 10^{16}$ cm^{-3}) on top of a n$^+$-GaAs substrate ($n = 10^{18}$ cm^{-3}). An electrolyte of dilute nitric acid (HNO_3:H_2O = 1:20) was used which had no measurable effect on GaAs without illumination [8].

3. Results and discussion

a. Current-potential-curves

In order to find the best conditions for highly localized light-induced etching, the behavior of the two materials n-GaAs and n-$Al_{0.3}Ga_{0.7}As$ was investigated under various applied potentials and light intensities. For the measurements, samples with 1-µm-thick single epilayers of AlGaAs or GaAs on top of a substrate of n$^+$-GaAs were used. The light intensity was chosen to be low

enough to ensure that the amount of etching during the measurement was negligible. Also the potential was scanned slowly enough for a steady-state current to be established in the cell.

Typical examples of our measured current-potential curves are shown in Fig. 2 for GaAs and AlGaAs samples; the GaAs curve agrees well with curves reported in the literature [5,22,28]. In the absence of light, both materials behave electrochemically essentially the same way. At an overvoltage of about +0.5 V, the anodic dissolution of the sample with the following reaction [29-31],

$$GaAs + 6\ h^+ + 5\ H_2O \rightarrow Ga^{3+} + HAsO_2 + 3\ H_3O^+, \qquad (1)$$

becomes important. At the other end of the potential scale, starting at -0.5 V, the cathodic reaction of hydrogen evolution is seen,

$$2\ H_3O^+ + 2\ e^- \rightarrow H_2 + 2\ H_2O. \qquad (2)$$

In the potential range between -0.4 and +0.4 V no measurable current is seen and, in fact, in this region the dissolution reaction (1) is limited by the thermal rate of generation of electron-hole pairs. With illumination, carrier generation within the semiconductor is increased sharply and a substantial current can then flow. Notice that the bands of an n-type semiconductor in contact with the electrolyte are bent upward (cf. Figs. 4 and 5) which is a necessary condition for holes to be driven to the surface for enhancement of the dissolution reaction (1) after charge separation [17,19,21].

Thus, in the potential range from -0.4 V to +0.4 V, etching occurs only within the illuminated spot. Additional experiments at various light intensities showed that for values up to the highest possible illumination, i. e. 250 mW/cm^2, the measured current and, correspondingly, the etch rate remain linearly proportional to the intensity. Similar results for a high intensity study of laser-induced etching of GaAs have been reported already by Ruberto *et al.* [8]. The following linear relationship between current and etch rate for GaAs and $Al_{0.3}Ga_{0.7}As$ was determined in our case:

$$\text{Etch Rate [nm/min]} = (15 \pm 5) * \text{Current Density [mA/cm}^2\text{]} \qquad \text{(GaAs, AlGaAs)}$$

where the current density is linearly dependent on the intensity of the incident light via:

$$\text{Current Density [mA/cm}^2\text{]} = (0.17 \pm 0.03) * \text{Light Intensity [mW/cm}^2\text{]} \qquad \text{(GaAs)}$$

$$\text{Current Density [mA/cm}^2\text{]} = (0.12 \pm 0.02) * \text{Light Intensity [mW/cm}^2\text{]} \qquad \text{(AlGaAs)}$$

These relations are consistent with the etch rates of 0.5 µm/min (GaAs) and 0.4 µm/min (AlGaAs) at 200 mW/cm^2 in our experiments. Also they are in agreement with the rates obtained in high-intensity laser etching of n-GaAs using the same electrolyte, although those experiments were performed under open-circuit conditions and with different light sources [8,25]. Laser etching experiments under conditions similar to ours, i. e. etching of n-GaAs with an applied potential in the plateau region of the I-V-curves (cf. Fig. 2), but with a different electrolyte, showed, after normalization of the light intensity, an etch rate which is of the same order of magnitude as our value [5].

The most important conclusion of the measurement of the current-potential curves is the difference in etch rate for GaAs and AlGaAs. Throughout the entire region where localized etching can be achieved, the etch current with AlGaAs is about 80% of the value for GaAs, which means that, for a given constant potential, AlGaAs is typically etched slower than GaAs. There are several possible explanations for the difference in etch rate in the two materials. Due to its larger band gap, AlGaAs will absorb a smaller percentage of the lamp's spectral flux than GaAs, thus generating a smaller carrier number per watt lamp output. In addition, $Al_xGa_{1-x}As$ has a lower carrier mobility due to alloy scattering which reduces the carrier collection efficiency in comparison to GaAs [32]. Finally, the surface oxide formed during photodecomposition of AlGaAs may possibly be harder to dissolve in the electrolyte due to its aluminum content than the GaAs decomposition products. A more definite conclusion must await a detailed chemical study of the decomposition of $Al_xGa_{1-x}As$.

b. Etching of single-layer structures

Figure 3 shows the result of an experiment in which a single AlGaAs epilayer on a n^+-GaAs substrate was etched. Under constant anodic potential, the current between sample and counter-electrode goes through a minimum as the etching proceeds through the interfacial region. The calibration of etch depth versus time in this experiment was done by determining the depth using a stylus profilometer for various exposure times.

One consequence of this experiment is that it is possible to determine which layer of a heterostructure is actually etched by simply measuring the current in the electrochemical cell.

Heterojunction interfaces show up as current minima and the exact depth within a certain layer can be calculated by integrating the current curve using the proportionality constants between cell current and etch rate from the previous section.

The overall increase in current with time which is observed in Fig. 3 can be explained simply by considering the resistance of the sample, e. g. during etching in the second layer: with time, the layer becomes thinner and thinner and, correspondingly, the ohmic resistance of the sample decreases thus causing the observed overall increase in current which appears in going from left to right in the figure.

In order to understand the factors which lead to the occurrence of a current minimum at the interface, one has to consider the energy band diagram for the AlGaAs/GaAs heterostructure (see Fig. 4). As a consequence of the different band gaps of GaAs and AlGaAs, a discontinuity in the conduction band and a potential step in the valence band occurs [33,34]; the width of the interface region is of the order of 0.2 μm [35]. Also, as already mentioned earlier, the semiconductor bands are bent upward at the interface with the electrolyte. When light illuminates the sample, charge carriers are produced within a region characterized by the photon absorption depth. In our case of white light from a halogen lamp, the photon energies are between 1 eV and 4 eV corresponding to absorption depths from 1000 to 20 nm, respectively [36]. The intensity maximum of the spectral distribution of this light source was at ~2 eV with a penetration depth of 230 nm for GaAs and 340 nm for $Al_{0.3}Ga_{0.7}As$ [36]. Thus the actual penetration is on average comparable to the depth of the interface.

The situation for three characteristic stages during etching of the AlGaAs/GaAs layered material is depicted schematically in Fig. 5 for a biased sample in contact with the solution. In A, the etch depth is still small and all charge carriers are produced within the AlGaAs epilayer. Due to the applied positive potential, the energy band diagram tilts in the direction of the substrate. Charge separation is easily effected, with holes transferring into solution and electrons in the conduction band gaining enough energy within the AlGaAs to overcome the small potential barrier (~0.1 eV) at the interface and to move further into the bulk. In B, the etch front has reached the interface region and now some charge carriers are generated within the GaAs substrate. However, those generated within the GaAs are prevented from reaching the liquid by the valence band offset, and are eventually lost via recombination. Thus in this region, the electrochemical current dips. Finally, in C, the etch front is fully within the GaAs substrate and, as in A above, charge separation and migration occurs in the usual way.

There are several factors which contribute to the broadness of the observed current minimum. First of all, any sharp features will be blurred as soon as the etch profile deviates from the ideal rectangular shape. If the edges of the etched hole are not vertical but sloped then the total etch current consists of contributions from a wide range of depths which are added to the signal from the bottom of the etched hole. Although the main part of the etched area (~70 %, see Figs. 11 and 12) has a uniform depth, the edges contribute significantly to the measured current and broaden the interface features because those regions of the etching front cross the heterojunction interface with a varying time delay. In addition, the use of white light illumination has the disadvantage that the absorption depths of the different wavelengths cover a much larger range

than in the case of a monoenergetic light source. Therefore, the transition from stage A to B in Fig. 5 will extend over a longer period of time when, as in our experiments, a broad wavelength spectrum is used.

c. Etching of multilayer structures

It was expected that etching of our multilayer structure consisting of four AlGaAs and GaAs epilayers with a back contact (Fig. 6a) would generally resemble the process seen for the single layer case, except that the larger number of layers would magnify the electrical effects seen above. In particular, since our epilayers were only weakly doped ($n=10^{16}$ cm^{-3}), their conductivity was relatively low and, as a result, only very small currents and etch rates could be achieved. This effect was obviously more important during etching the uppermost layers of the sample while for the deepest lying AlGaAs/GaAs interface the current was much larger (Fig. 6b). As was seen in the case of a single epilayer sample (Fig. 3), a current minimum occured when the etch front entered the interface. This effect was most pronounced for the lower pair of layers; however, weaker current minima also coincide with the other three interfaces which can be seen only when the sensitivity of the current measurement is increased (Fig. 6b). Moreover, as a consequence of the low current, very long times are needed to etch the upper layers.

In order to circumvent the current limitation due to the serial path through the layers, an additional side contact was attached to the multilayer sample (Fig. 7a). In this case, all layers as

well as the substrate have a conducting connection to the current source, along paths parallel to the interface. Fig. 7b shows the etching of the multilayer sample from Fig. 7a under constant potential; again, depth measurements at various points of the curve revealed the coincidence of current minima with the crossing of an interface during etching. Obviously, the sensitivity of the current signal for the interfaces has strongly increased, particularly for the topmost layers, compared to the results shown in Fig. 6b. Also the current density is much higher than in the experiment without side contact. As before, in the case of the single-layer structure (cf. Sect. 3b), the broadness of the observed features is mainly due to the deviations of the etch profile from a rectangular shape.

Etching can also be monitored by keeping the current at a constant value and measuring the potential changes of the sample; this experiment is done using a potentiostat which adjusts the potential by means of a feedback mechanism so that the current remains constant. The resulting potential changes during etching (Fig. 7c) are essentially a mirror image of the corresponding current curve: a potential maximum in Fig. 7c corresponds to a current minimum in Fig. 7b. The differences between Fig. 7b and c, i. e. the different shape and size of corresponding sections of the curve, are due to the non-ohmic character of the electrolyte-semiconductor junction which can best be seen from the nonlinear relationship between current and potential in Fig. 2.

For a detailed explanation of the results shown in Fig. 7b and c, the above simplified picture of charge carriers moving within an epilayer to the side contact has to be refined. The origin of the high conductivity to the side contact can be seen from the energy band diagram of the sample

(Fig. 8a). In particular, the "notches" in the conduction band in Fig. 8a trap electrons which are strongly localized perpendicular to the interface but can move freely in a plane parallel to it. This two-dimensional electron gas (2DEG) forms a low resistance electron path to the side contact.

If a positive potential is applied across a layered structure with no side contact, as shown in Fig. 8b for a simple four-layered example, the potential wells at AlGaAs/GaAs interfaces for the conduction band are depleted compared to the unbiased condition, whereas at the GaAs/AlGaAs junctions the local electron concentration increases. Compare, for example, the first two "notches" on the left side of Fig. 8b. Thus, in Fig. 8b, a 2DEG is present only at the first and third interface. When a side contact is applied to this layered structure, charge flow and potentials change dramatically. For example, electrons produced by incoming photons move first in vertical direction until they reach the 2DEG and then follow this low resistance path in their further movement towards the current source. Moreover, the 2DEG in combination with side and back contacts acts like a metallic shield around the deeper lying epilayers and the substrate of the sample, leaving these layers effectively unbiased. As a result of this shielding effect, the current flow through a multilayer sample with a side contact is very similar to the case of a two-layer structure of GaAs/AlGaAs or AlGaAs/GaAs.

The etching of the multilayer sample of Fig. 7a is depicted schematically in four stages together with the corresponding energy band diagrams (Fig. 9). Obviously, the etching of layers 1 and 3 and also layers 2 and 4 are equivalent situations. In layers 1 and 3 the electrons have to move

through less than one epilayer until they reach the 2DEG, whereas in layers 2 and 4 they have to cross an AlGaAs/GaAs interface as well as the next layer before they arrive at the electrical contact.

The sharp potential increase when the third interface is crossed (Fig. 7c) can be explained by the fact that the electrons now have to traverse the entire substrate (thickness: 380 μm) compared to the 1-μm-thick epilayers. Although the substrate is more heavily doped ($n=10^{18}$ cm^{-3}) than the epilayers ($n=10^{16}$ cm^{-3}), its total vertical resistance (0.05 Ω) is several times higher than that of the epilayers (0.01 Ω) due to the diffence in thickness, and therefore a higher potential is required to keep the current constant.

The occurrence of current minima (or potential maxima) at the interfaces between layers 2 and 3 and between layer 4 and the substrate can be explained in analogy to Fig. 5 for the single-layer structure: near the AlGaAs/GaAs interface, within the absorption depth of the photons, part of the generated electrons and holes are produced in the deeper layer. In particular, the holes on their way to the surface have to overcome a potential step in the valence band which impedes their current for the case of constant potential etching (Fig. 7b), or increases the applied potential in the case of constant current etching (Fig. 7c).

At the interfaces between layers 1 and 2 and between layers 3 and 4, the reason for the occurrence of a current or potential extremum is different. Due to the fact that the 2DEG at the interface shields the deeper layers, that is, reduces any voltage gradient in those layers, charge

carriers which are generated in layer 2 or 4, respectively, do not experience a voltage to separate the charges. Therefore, recombination is enhanced in this buried region causing a net loss in collected current when etching at constant potential (Fig. 7b). When etching at constant current (Fig. 7c) this loss of photocurrent is seen as an increase in the internal resistance of the sample; thus the voltage across the sample rises.

Finally, we note that, as in the case of single-layer structures (cf. Sect. 3b), it is possible to monitor the progress of light-induced multilayer etching by simple measurements of current or potential, since crossing of interfaces is clearly indicated by the occurrence of a current minimum or potential maximum, respectively.

d. Morphological aspects of the photoelectrochemical etching of multilayers

In the experiments presented so far, the morphology of the etched surface area was not taken into consideration. However, during etching, the surface does not maintain its initial smoothness but becomes rougher with increasing etch depth. This can best be seen in a series of corresponding optical micrographs and SEM photographs which show the etched spot and its profile in the four epilayers and the substrate (Fig. 10).

Starting from the polished surface with a roughness of less than 10 nm, one observes a gradual increase up to ~450 nm when the substrate is reached. During etching of the first GaAs layer, the illuminated area is still nearly as smooth as the unetched surface leading to a very weak

contrast between these areas in the optical micrograph. This is no longer the case as soon as the AlGaAs layer is entered. Strongly inhomogeneous etching occurs possibly due to the formation of nearly insolvable aluminum oxides which prevent the underlying surface from being affected by the electrolyte and cause the observed roughening. As mentioned, this phenomenon of slow dissolution of Al_2O_3 may in part be responsible for the fact that the etch rate in AlGaAs is lower than in GaAs; the presence of those oxides prevents the photogenerated holes from reaching the surface and from participating in the dissolution reaction (cf. Sect. 3a and Fig. 2). As a result of this roughness, the crossing of the etch front across an interface is distributed in time. This blurring of the current or voltage extrema is particular important for very thin layers or, also very thick layers lying deep in a multilayer stack, even if the etching beam is uniform.

In Fig. 10, care was taken to image the rectangular intensity distribution of the illumination to obtain a nearly rectangular profile of the eched area. Such a clear image was, however, not always observed, even with a good quality image. In fact, a detailed study revealed a dependence of the etch profile on the value of current (for constant-current etching) or voltage (for constant-potential etching) as shown in Figs. 11 and 12. For etching at a relatively low value of constant current density (9.3 mA/cm^2), a profile with a deep trench along the edge of the illuminated area is obtained. This trench gradually disappears when the current density is increased to 18.5 mA/cm^2 and 27.8 mA/cm^2 (Fig. 11). As a direct consequence of the etch profile, the shape of the corresponding potential curve is strongly altered when etching at different currents. This behavior is seen by comparing the voltage versus time curves (left in Fig. 11) with stylus profilometry data (right in Fig. 11). For 9.3 mA/cm^2, when, due to the deep trench, several epilayers are etched

concurrently, the observed features in the potential curve are very broad and partially undetectable, e. g. the crossing of the interfaces between layers 3 and 4 or between layer 4 and the substrate. The potential maxima become, however, well resolved and sharp for higher currents (18.5 and 27.8 mA/cm^2), corresponding to the rectangular etch profile, which causes the uniform crossing of a heterojunction interface over the entire illuminated area.

A similar result, although not with such large differences in the etch profiles, is obtained in etching experiments at constant potential (Fig. 12). For a fixed negative potential, inhomogeneous etching occurs resulting in a trench, as seen already in Fig. 11. For more positive values of applied potential, the etch profile is spatially homogeneous and nearly rectangular. Again, corresponding to the quality of the etch profile, the features in the current curves of Fig. 12 are more or less sharp. In particular, when etching the uppermost layer under conditions of spatially homogeneous etching, an additional fine structure appears which is possibly due to the energy band structure near the heterojunction. When etching the deeper layers such fine structures are not observed since the increasing roughness of the surface causes sufficiently inhomogeneous etching so that fine features cannot be resolved.

Finally, the evolution of an inhomogeneous etch profile in Figs. 11 and 12 can be explained by consideration of the potential distribution within the sample. In particular, a comparison with Fig. 2 shows that the potential range for which inhomogeneous etching occurs, ~ -0.5 V, is very near to zero current conditions. At this open-circuit potential no current flows between sample and counter-electrode; however, light-induced etching can exist under these conditions. This

etching is made possible by the fact that the illuminated areas of the surface act as local anodes and the dark areas as cathodes [8,17]. Incoming photons establish a gradient in concentration of charge carriers and voltage between dark and illuminated zones, consequently causing a current to flow within the semiconductor [17,22,23]. This situation is depicted schematically in Fig. 13a.

Obviously, the series resistance has its lowest value near the boundary of the illuminated area where the distance to the cathodic dark area is least. As a result, under open-circuit conditions preferential etching will occur at the edges of the hole and produce trenches [3]. Minority charge carriers from more distant regions, e. g. the center of the illuminated area, have to move over larger distances and are more likely to recombine. The formation of such trenches has also been discussed in several other reports [8,25,37]. At applied potentials only slightly more positive than the open-circuit value, the light-induced field gradient is superimposed onto the external potential value which locally enhances the etching (Fig. 13b). If the applied potential is increased further the relative importance of the light-induced potential is reduced; the current towards the sidewalls of the etched hole then decreases and the vast majority of the charge carriers follows the direction of the applied field (Fig. 13c). Therefore, the preferential etching of trenches along the sidewalls of the hole is not significant at more positive potentials.

e. Etching of multiquantum well structures

As a consequence of the increased roughness of the surface after etching several layers, the controlled layer-by-layer etching of samples with very thin epilayers is only possible as long as

the surface roughness does not exceed the layer thickness. Fig. 14 shows an experiment where a multiquantum well (MQW) sample with layers of 20 and 40 nm thickness has been etched at constant current and with a side contact (Fig. 14a). A sharp potential maximum is observed when the interface between the GaAs-caplayer and the multiquantum wells is crossed. Beyond this point, however, the maxima which correspond to quantum well interfaces are not detectable (Fig. 14b), except for a heavily damped peak in the second layer.

SEM investigations revealed that MQWs, etched to a depth of many layers, are removed very inhomogeneously, giving rise to a rough surface with a terrace-like microscopic structure (Fig. 14c). The step height of these terraces corresponds to the thickness of the MQW-epilayers. Moreover, when etching at constant current, within this rough surface deep holes are found which extend down to the substrate. With time, these holes coalesce resulting in a large area where the substrate is laid open (Fig. 14d). Further etching occurs preferentially in a lateral direction until the MQW material is removed within the entire illuminated spot (Fig. 14e). Possibly, the high degree of charge carrier confinement within the thin quantum wells is responsible for this effect. During the process of lateral etching, the etching in vertical direction proceeds at a considerably lower rate giving the substrate a much smoother surface than that of the MQWs.

4. Conclusions

By using electrochemical methods for the monitoring of light-induced etching it was possible to study the behavior of heterostructures in contact with an electrolyte. It was found that the energy band structure of a heterojunction strongly affects the etching process. The sensitivity of current and potential measurements can be strongly increased by attaching an ohmic side contact to the sample exploiting a layer of quasi-two-dimensional electrons at the GaAs/AlGaAs interface which acts as conducting path towards the side-contact and leads to a lower resistance of the sample and increased current.

In experiments at constant potential, the crossing of an interface during etching shows up as a current minimum. Correspondingly, in constant current etching, interfaces are indicated by potential maxima. Based on these results it is possible to apply current or potential measurements as *in situ* process diagnostics for the etching of multilayer structures. Without removing the sample from the electrochemical cell one can tell which layer is currently etched, and an integration of the etch current allows to determine the approximate etch depth.

A detailed study of the surface morphology during etching with a beam of uniform intensity revealed that generally the surface roughness increases with time, possibly due to the accumulation of insolvable aluminum oxides. Moreover, the magnitude of the applied potential was found to control the uniformity of the etching. This result could be explained by an additional field gradient between dark and illuminated areas which is present near open-circuit conditions and causes enhanced etching at the boundary between those areas. Since this

photopotential is superimposed onto the external voltage, its influence decreases when larger external potentials are applied. Due to the increasing roughness of the surface with exposure time it is presently impossible to etch very thin epilayers, such as MQWs, in a well-defined way layer-by-layer, except to remove the top layer.

Acknowledgements

We thank Dr. M. Levy for many helpful discussions and for assistance in preparing the samples. Also, we are indebted to Prof. Wen Wang for generously providing the multilayer samples. This work was supported by the Defence Advanced Research Project Agency (DARPA) and the U. S. Air Force Office of Scientific Research (AFOSR). In addition, Thomas Fink would like to thank the Deutsche Forschungsgemeinschaft (DFG) for support granted under a research fellowship.

References

[1] S. D. Mukherjee and D. W. Woodard, in: *Gallium Arsenide* (Eds.: M. J. Howes and D. V. Morgan), Wiley and Sons, New York (1985), p. 119.

[2] J. J. Kelly, J. E. A. M. van den Meerakker, P. H. L. Notten, and R. P. Tijburg, Philips Tech. Rev. 44, 61 (1988).

[3] F. Kuhn-Kuhnenfeld, J. Electrochem. Soc. 119, 1063 (1972).

[4] F. W. Ostermayer, Jr., and P. A. Kohl, Appl. Phys. Lett. 39, 76 (1981).

[5] H. J. Hoffmann, J. M. Woodall, and T. I. Chappell, Appl. Phys. Lett. 38, 564 (1981).

[6] G. C. Tisone and A. W. Johnson, Appl. Phys. Lett. 42, 530 (1983).

[7] R. M. Osgood, Jr., A. Sanchez-Rubio, D. J. Ehrlich, and V. Daneu, Appl. Phys. Lett. 40, 391 (1982).

[8] M. N. Ruberto, X. Zhang, R. Scarmozzino, A. E. Willner, D. V. Podlesnik, and R. M. Osgood, Jr., J. Electrochem. Soc. 138, 1174 (1991).

[9] F. W. Ostermayer, Jr., P. A. Kohl, and R. H. Burton, Appl. Phys. Lett. 43, 642 (1983).

[10] R. M. Lum, A. M. Glass, F. W. Ostermayer, Jr., P. A. Kohl, A. A. Ballman, and R. A. Logan, J. Appl. Phys. 57, 39 (1985).

[11] D. V. Podlesnik, H. H. Gilgen, R. M. Osgood, Jr., and A. Sanchez, Appl. Phys. Lett. 43, 1083 (1983).

[12] A. E. Willner, M. N. Ruberto, D. J. Blumenthal, D. V. Podlesnik, and R. M. Osgood, Jr., Appl. Phys. Lett. 54, 1839 (1989).

[13] M. N. Ruberto, R. Scarmozzino, A. E. Willner, D. V. Podlesnik, and R. M. Osgood, Jr., SPIE 1215 *Digital Optical Computing II*, 538 (1990).

[14] R. A. Logan and F. K. Reinhart, J. Appl. Phys. 44, 4172 (1973).

[15] J. E. Bowers, B. R. Hemenway, and D. P. Wilt, Appl. Phys. Lett. 46, 453 (1985).

[16] O. A. Ghandour, R. Scarmozzino, R. M. Osgood, Jr., and W. W. Hooper, submitted to Appl. Phys. Lett.

[17] Y. V. Pleskov and Y. Y. Gurevich, *Semiconductor Photoelectrochemistry*, Consultants Bureau, New York (1986).

[18] F. Williams and A. J. Nozik, Nature 312, 21 (1984).

[19] H. Gerischer, in: *Topics in Applied Physics, Vol. 31: Solar Energy Conversion* (Ed.: B. O. Seraphin), Springer, Berlin (1979), p. 115.

[20] J. Reichman, Appl. Phys. Lett. 36, 574 (1980).

[21] H. Gerischer, J. Vac. Sci. Technol. 15, 1422 (1978).

[22] J. van de Ven and H. J. P. Nabben, J. Electrochem. Soc. I: 137, 1603 (1990); II: 138, 144 (1991).

[23] J. van de Ven and H. J. P. Nabben, J. Appl. Phys. 67, 7572 (1990).

[24] F. W. Ostermayer, Jr., P. A. Kohl, and R. M. Lum, J. Appl. Phys. 58, 4390 (1985).

[25] R. T. Brown, J. F. Black, R. N. Sacks, G. G. Peterson, and F. J. Leonberger, Mat. Res. Soc. Symp. Proc. 75, 411 (1987).

[26] M. N. Ruberto, A. E. Willner, D. V. Podlesnik, and R. M. Osgood, Jr., Appl. Phys. Lett. 55, 984 (1989).

[27] R. Khare and E. L. Hu, J. Electrochem. Soc. 138, 1516 (1991).

[28] L. Hollan, J. C. Tranchart, and R. Memming, J. Electrochem. Soc. 126, 855 (1979).

[29] H. Gerischer, Ber. Bunsenges. Phys. Chem. 69, 578 (1965).

[30] W. W. Harvey, J. Electrochem. Soc. **114**, 472 (1967).

[31] P. Allongue and S. Blonkowski, J. Electroanal. Chem. I: **316**, 57 (1991); II: **317**, 77 (1991).

[32] S. Adachi, J. Appl. Phys. **58**, R1 (1985).

[33] T. L. Tansley, in: *Semiconductors and Semimetals* (Eds.: R. K. Willardson and A. C. Beer), Vol. 7: *Applications and Devices Part A*, Academic Press, New York (1971), p. 293.

[34] H. Kroemer, in: *VLSI Electronics Microstructure Science* (Ed.: N. G. Einspruch), Vol. 10: *Surface and Interface Effects in VLSI* (Eds.: N. G. Einspruch and R. S. Bauer), Academic Press, Orlando, Fla. (1985), p. 121.

[35] M. O. Watanabe, J. Yoshida, M. Mashita, T. Nakanisi, and A. Hojo, J. Appl. Phys. **57**, 5340 (1985).

[36] D. E. Aspnes, S. M. Kelso, R. A. Logan, and R. Bhat, J. Appl. Phys. **60**, 754 (1986).

[37] J. van de Ven, J. L. Weyher, J. E. A. M. van den Meerakker, and J. J. Kelly, J. Electrochem. Soc. **133**, 799 (1986).

Figure Captions

Fig. 1: Experimental setup for photoelectrochemical etching.

Fig. 2: Current-potential curves for GaAs and AlGaAs under illumination and in the dark (scan rate: 5mV/s).

Fig. 3: Photoelectrochemical etching of a single-layer sample:

a: Structure of the sample.

b: Current curve for etching at constant potential.

Fig. 4: Energy band diagram for the single-layer sample of Fig. 3a.

Fig. 5: Schematic plot of three different stages during the etching through the AlGaAs/GaAs interface of the single-layer sample of Fig. 3a. Also depicted are the corresponding energy band diagrams under an applied positive potential and the direction of the movement of photogenerated charge carriers.

Fig. 6: Photoelectrochemical etching of a multilayer sample:

a: Structure of the sample.

b: Current curve for etching at constant potential. In the upper part of the figure, a section of the same curve is shown ten times magnified.

Fig. 7: Photoelectrochemical etching of a multilayer sample with additional side contact:
a: Structure of the sample.
b: Current curve for etching at constant potential.
c: Potential curve for etching at constant current.

Fig. 8: Energy band diagram of the multilayer sample of Figs. 6a and 7a. The two-dimensional electron gas (2DEG) at the interfaces is marked.
a: *Equilibrium situation.*
b: Situation for an applied potential.

Fig. 9: Schematic plot of four stages during the etching of the multilayer sample of Fig. 7a together with the corresponding energy band diagrams under applied positive potential.

Fig. 10: Optical micrographs showing the increase in surface roughness during etching the multilayer sample of Fig. 7a.

Fig. 11: Photoelectrochemical etching of the multilayer sample of Fig. 7a at various values of constant current. The curves for 13.9, 18.5, 23.2, and 27.8 mA/cm^2 have offsets of 0.3, 0.6, 0.9, and 1.2 V, respectively. For three values also the resulting etch profile is shown.

Fig. 12: Photoelectrochemical etching of the multilayer sample of Fig. 7a at various values of constant potential together with the resulting etch profiles. The curves for V_{SCE} = -0.2, +0.2, +0.4, and +0.6 V have offsets of 20, 40, 60, and 80 μA, respectively.

Fig. 13: Schematic plot of field distribution during photoelectrochemical etching at various potentials together with the resulting etch profiles:

a: Open-circuit conditions (zero current).

b: Applied potential slightly more positive than the open-circuit value.

c: Large positive potential.

Fig. 14: Photoelectrochemical etching of a multiquantum-well sample with side contact:

a: Structure of the sample.

b: Potential curve for etching at constant current.

c: SEM micrograph showing the surface structure after entering the MQWs.

d: SEM micrograph showing the situation after reaching the substrate.

e: Etch profiles showing the sequential etching of the MQW stack at constant current. As explained in the text, in the interval between 8.3 and 13.3 min, the original etched hole to the substrate widens by lateral etching.

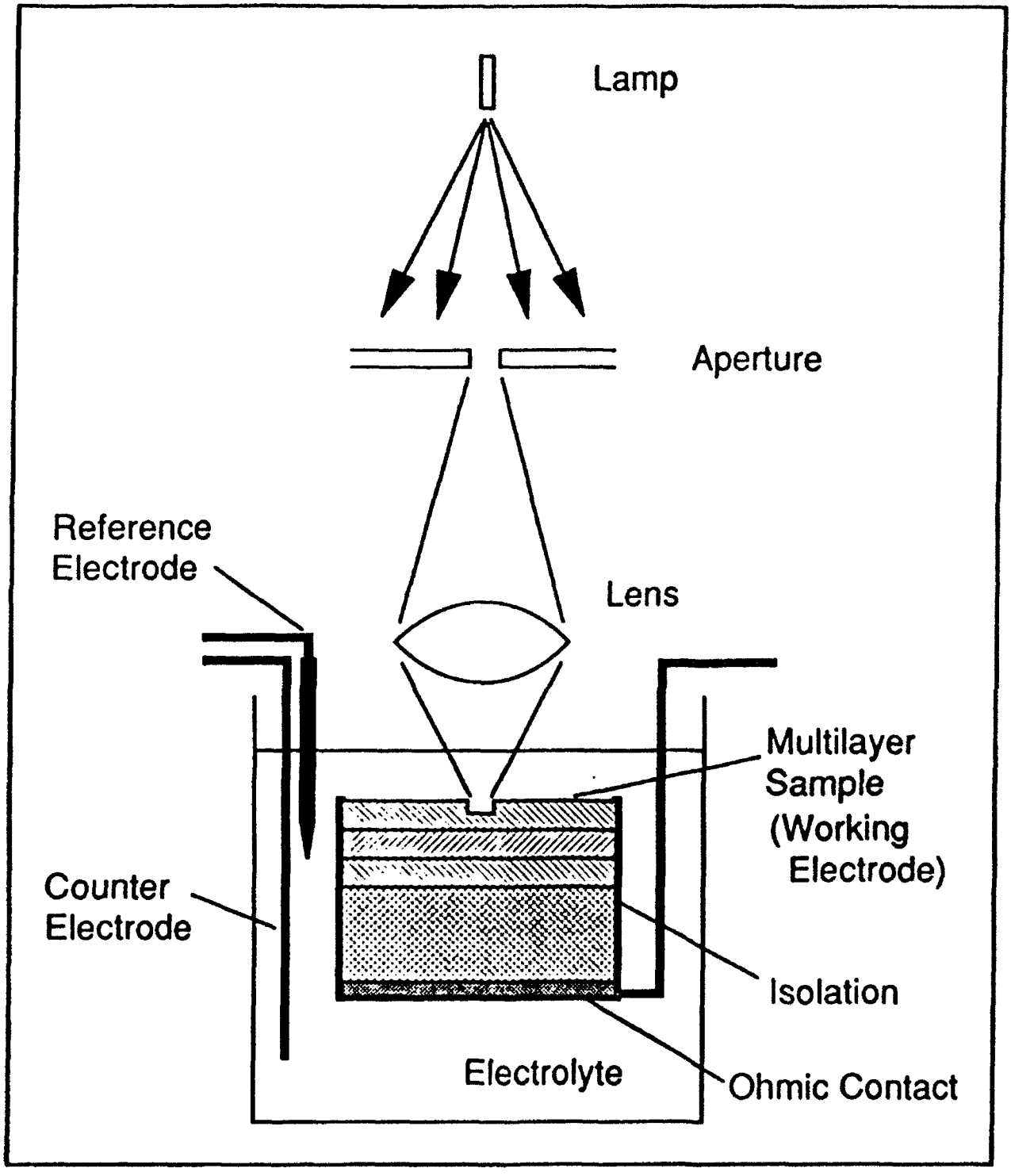
Lamp
Aperture
Reference Electrode
Lens
Multilayer Sample (Working Electrode)
Counter Electrode
Isolation
Electrolyte
Ohmic Contact

Fig. 1

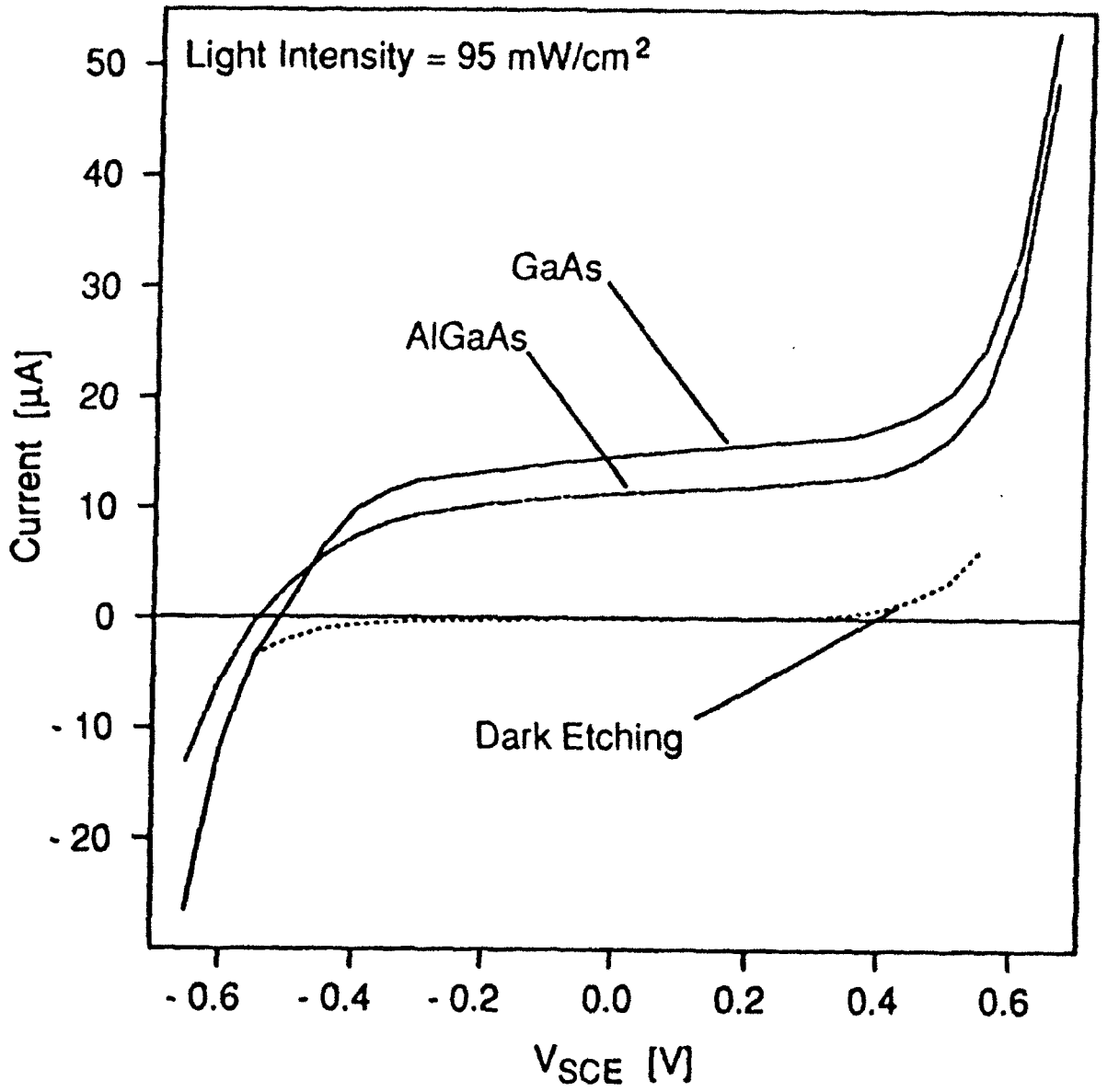
Light Intensity = 95 mW/cm²
50
40
30
20
10
0
- 10
- 20
Current [µA]
GaAs
AlGaAs
Dark Etching
- 0.6
- 0.4
- 0.2
0.0
0.2
0.4
0.6
V_SCE [V]

Fig. 2

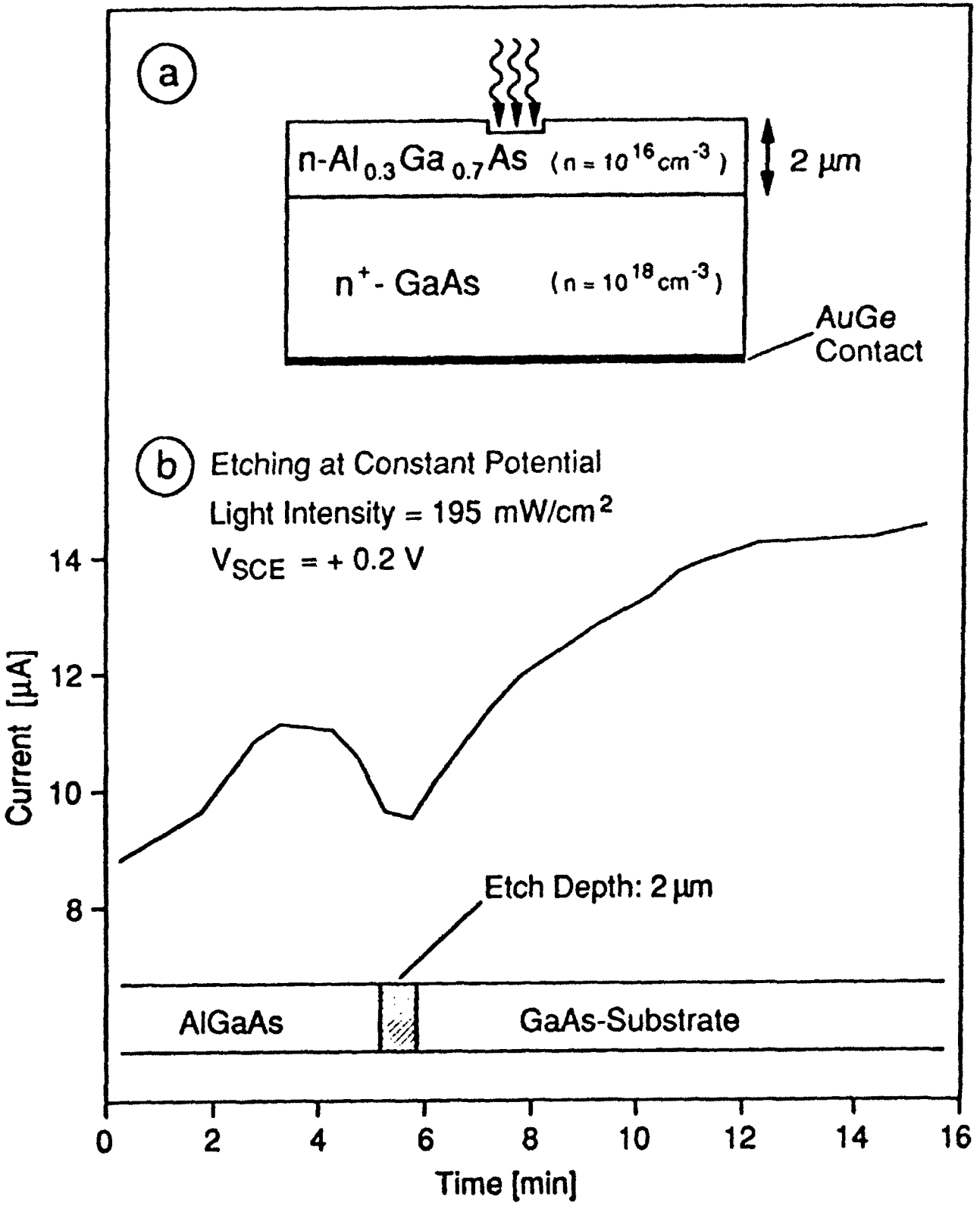
a
n-Al0.3Ga0.7As (n = 10^16 cm^-3)
2 µm
n+- GaAs (n = 10^18 cm^-3)
AuGe Contact
b
Etching at Constant Potential
Light Intensity = 195 mW/cm2
VSCE = + 0.2 V
Current [µA]
14
12
10
8
Etch Depth: 2 µm
AlGaAs
GaAs-Substrate
0
2
4
6
8
10
12
14
16
Time [min]

Fig. 3a/b

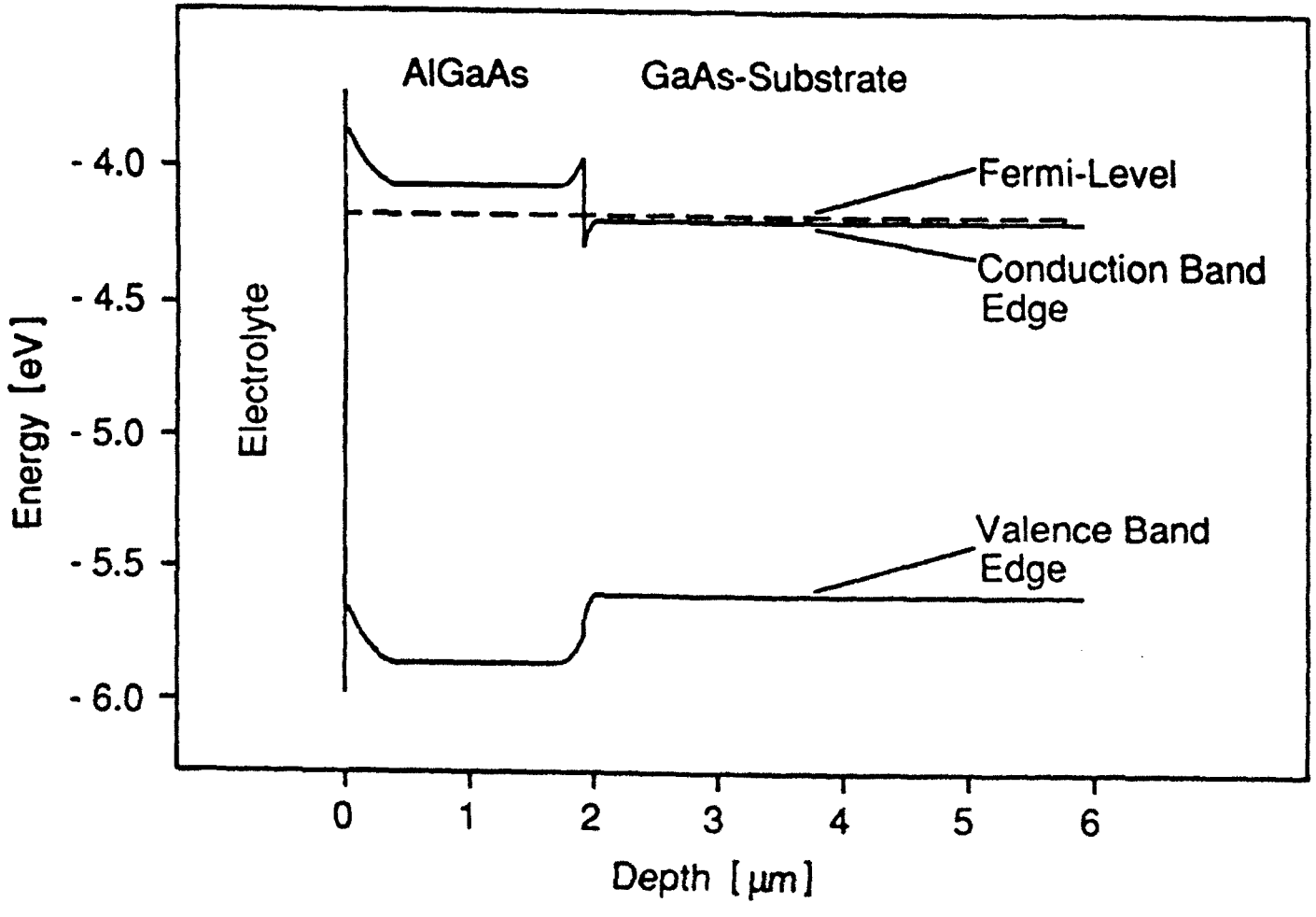
AlGaAs
GaAs-Substrate
Fermi-Level
Conduction Band Edge
Valence Band Edge
Electrolyte
Energy [eV]
- 4.0
- 4.5
- 5.0
- 5.5
- 6.0
0
1
2
3
4
5
6
Depth [µm]

Fig. 4

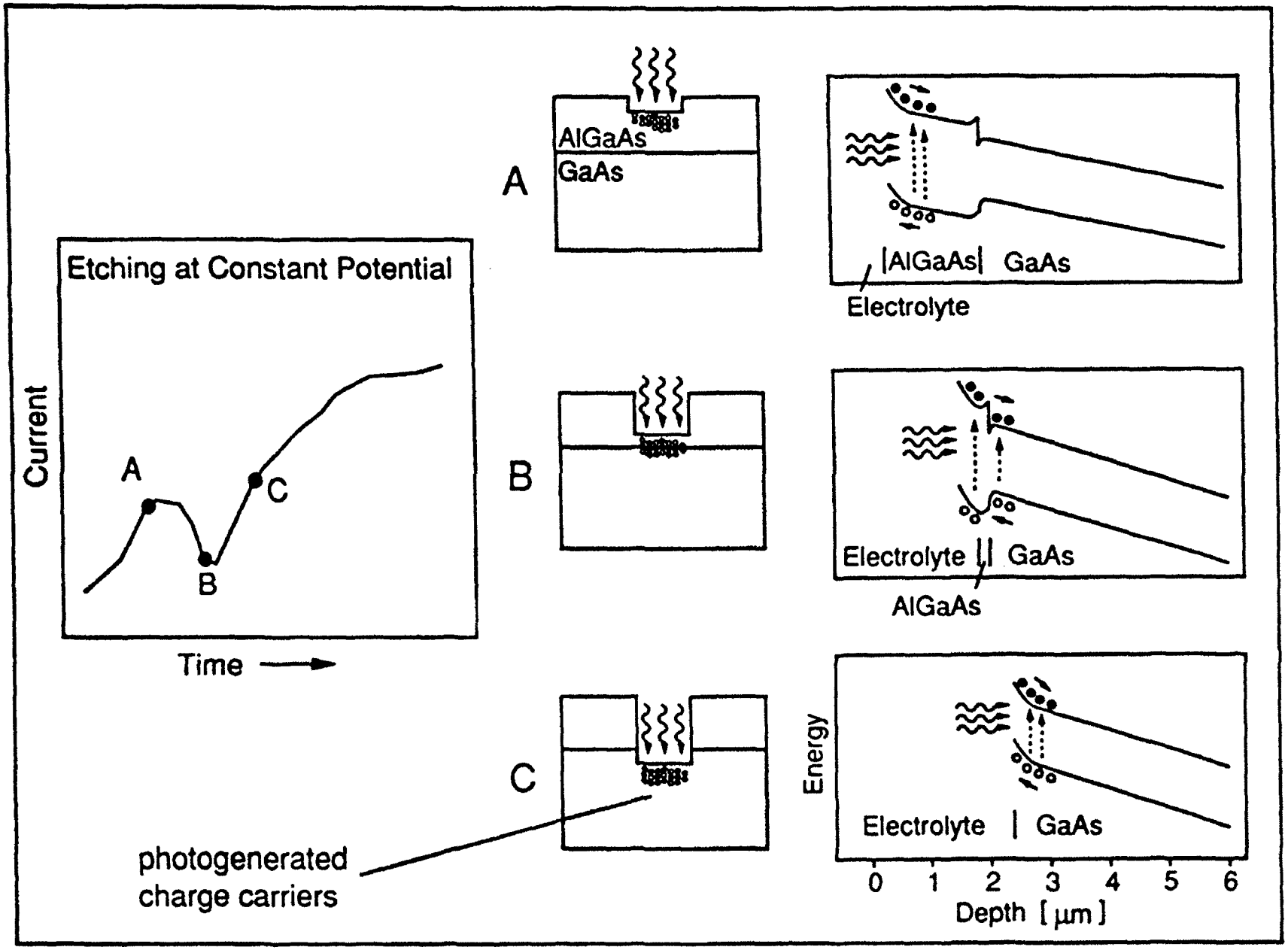
Etching at Constant Potential
Current
A
B
C
Time
A
AlGaAs
GaAs
B
C
photogenerated
charge carriers
|AlGaAs| GaAs
Electrolyte
Electrolyte || GaAs
AlGaAs
Energy
Electrolyte | GaAs
0 1 2 3 4 5 6
Depth [µm]

Fig. 5

(a)

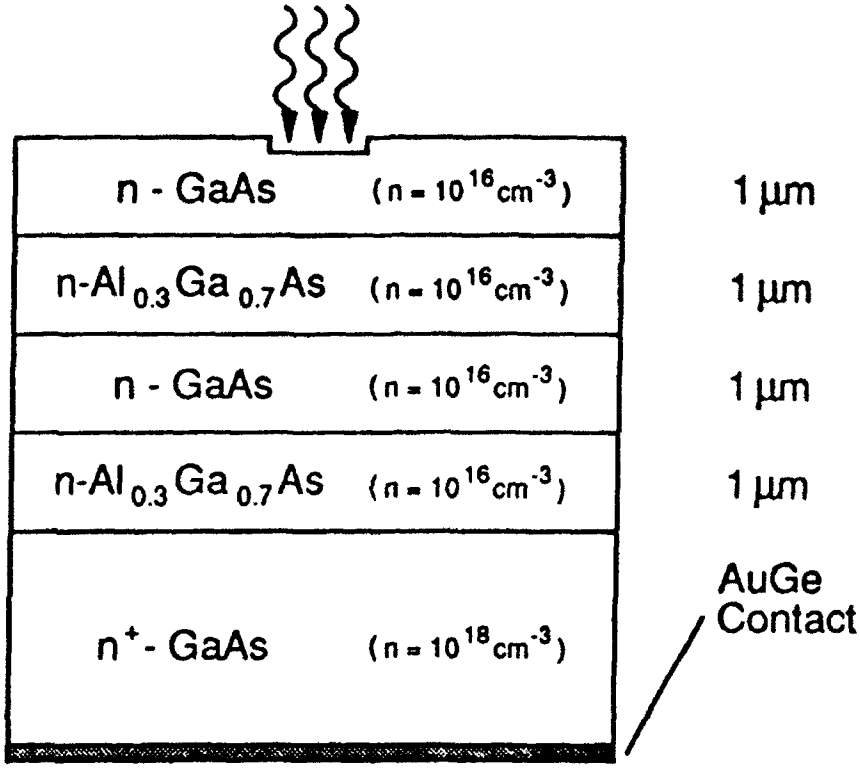
n - GaAs (n = 10^16 cm^-3) 1 µm
n-Al0.3Ga0.7As (n = 10^16 cm^-3) 1 µm
n - GaAs (n = 10^16 cm^-3) 1 µm
n-Al0.3Ga0.7As (n = 10^16 cm^-3) 1 µm
n+ - GaAs (n = 10^18 cm^-3)
AuGe Contact

Fig. 6a

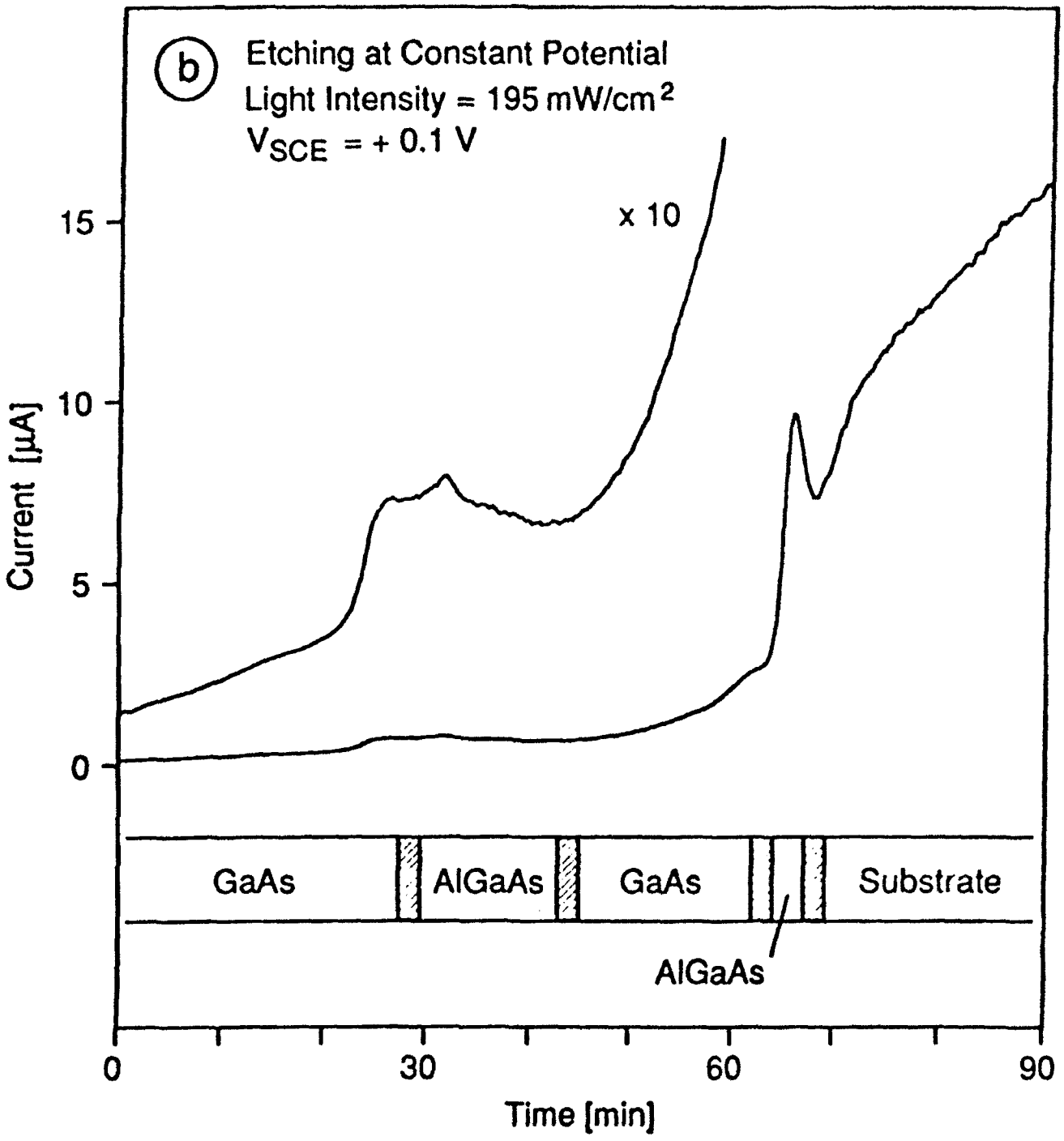
b
Etching at Constant Potential
Light Intensity = 195 mW/cm²
V_SCE = + 0.1 V
x 10
15
10
5
0
Current [μA]
GaAs
AlGaAs
GaAs
Substrate
AlGaAs
0
30
60
90
Time [min]

Fig. 6b

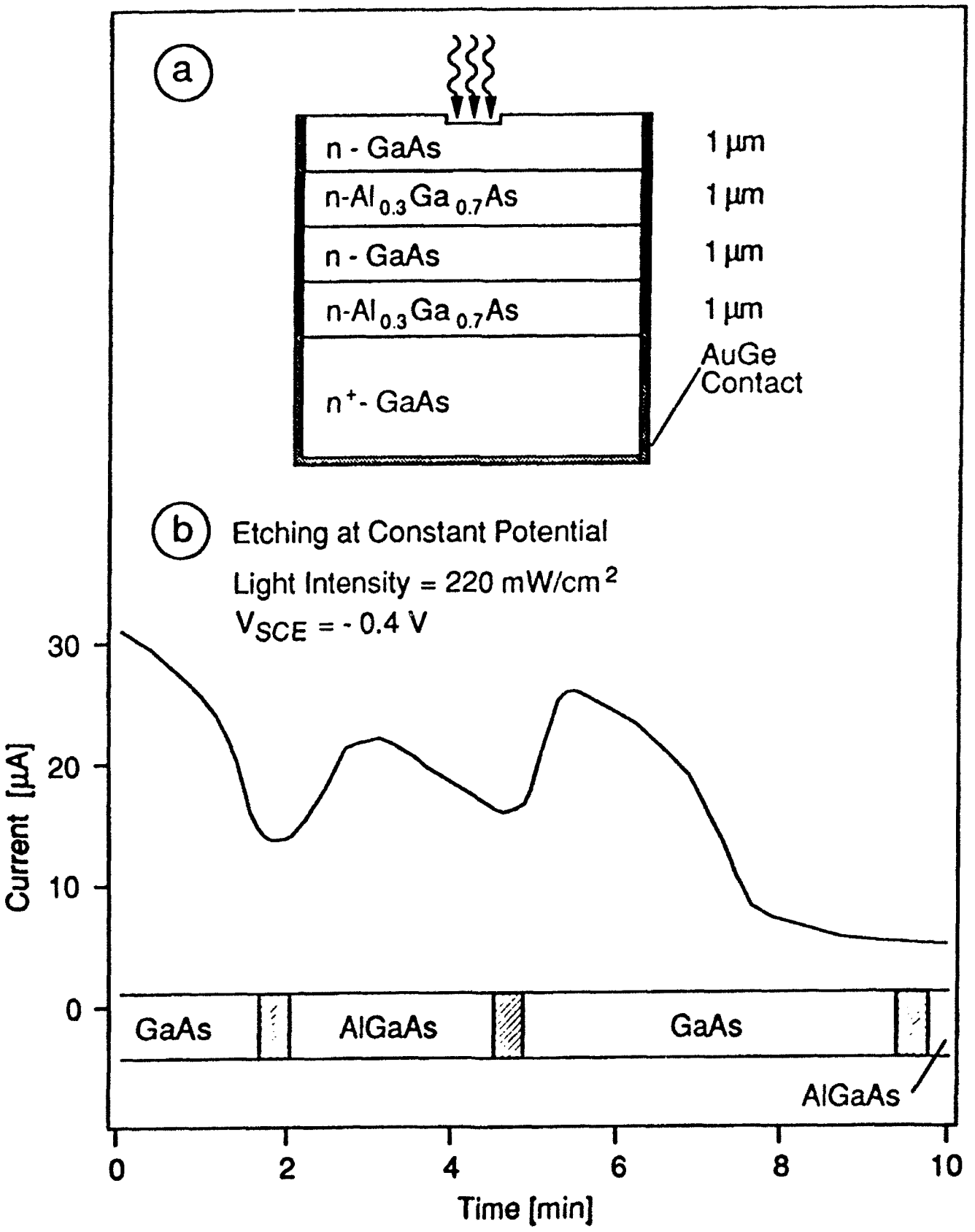
a
n - GaAs
n-Al0.3Ga0.7As
n - GaAs
n-Al0.3Ga0.7As
n+- GaAs
1 µm
1 µm
1 µm
1 µm
AuGe Contact
b
Etching at Constant Potential
Light Intensity = 220 mW/cm2
VSCE = - 0.4 V
Current [µA]
30
20
10
0
GaAs
AlGaAs
GaAs
AlGaAs
0
2
4
6
8
10
Time [min]

Fig. 7a/b

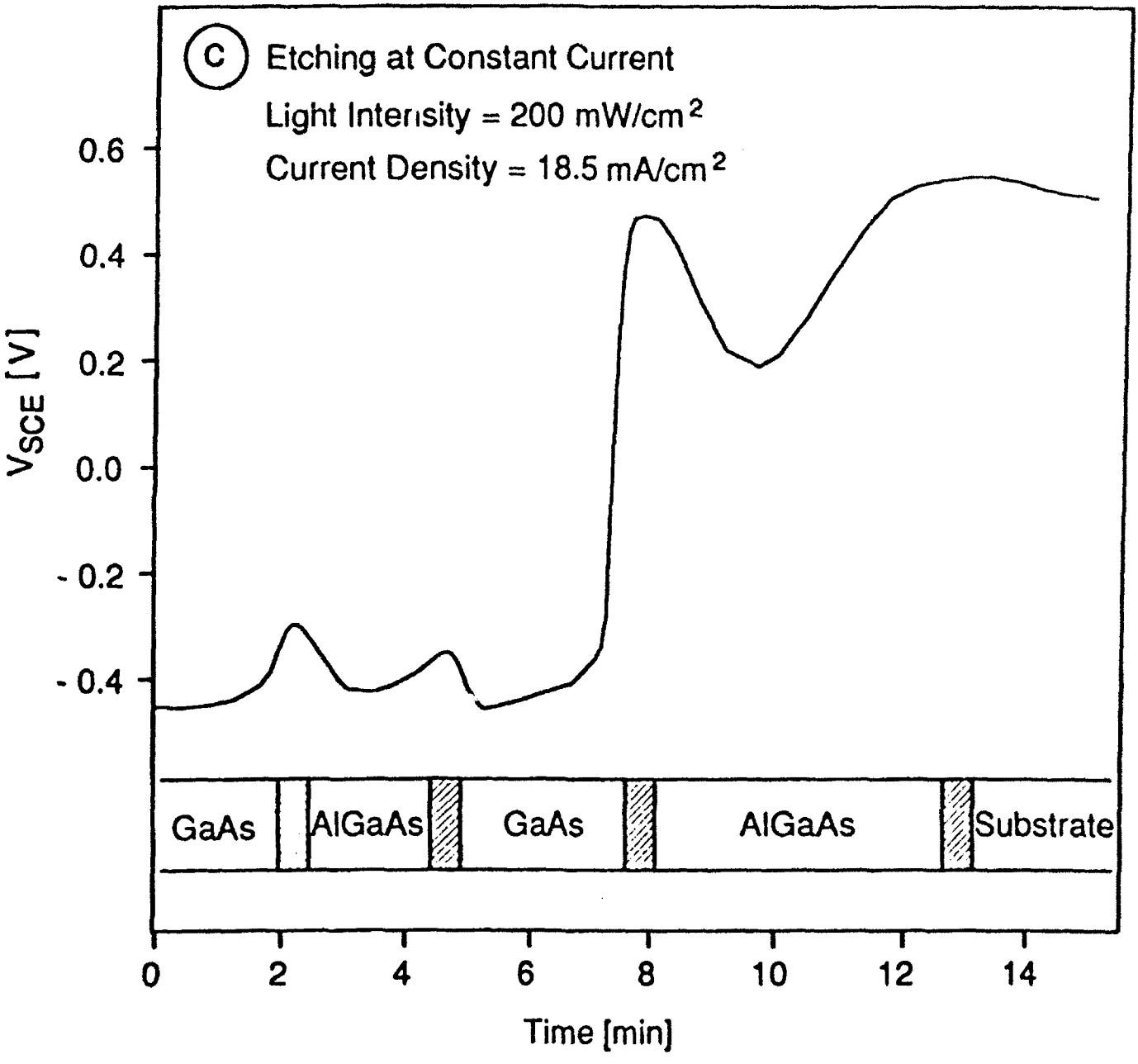
C
Etching at Constant Current
Light Intensity = 200 mW/cm 2
Current Density = 18.5 mA/cm 2
0.6
0.4
0.2
0.0
- 0.2
- 0.4
V_{SCE} [V]
GaAs
AlGaAs
GaAs
AlGaAs
Substrate
0
2
4
6
8
10
12
14
Time [min]

Fig. 7c

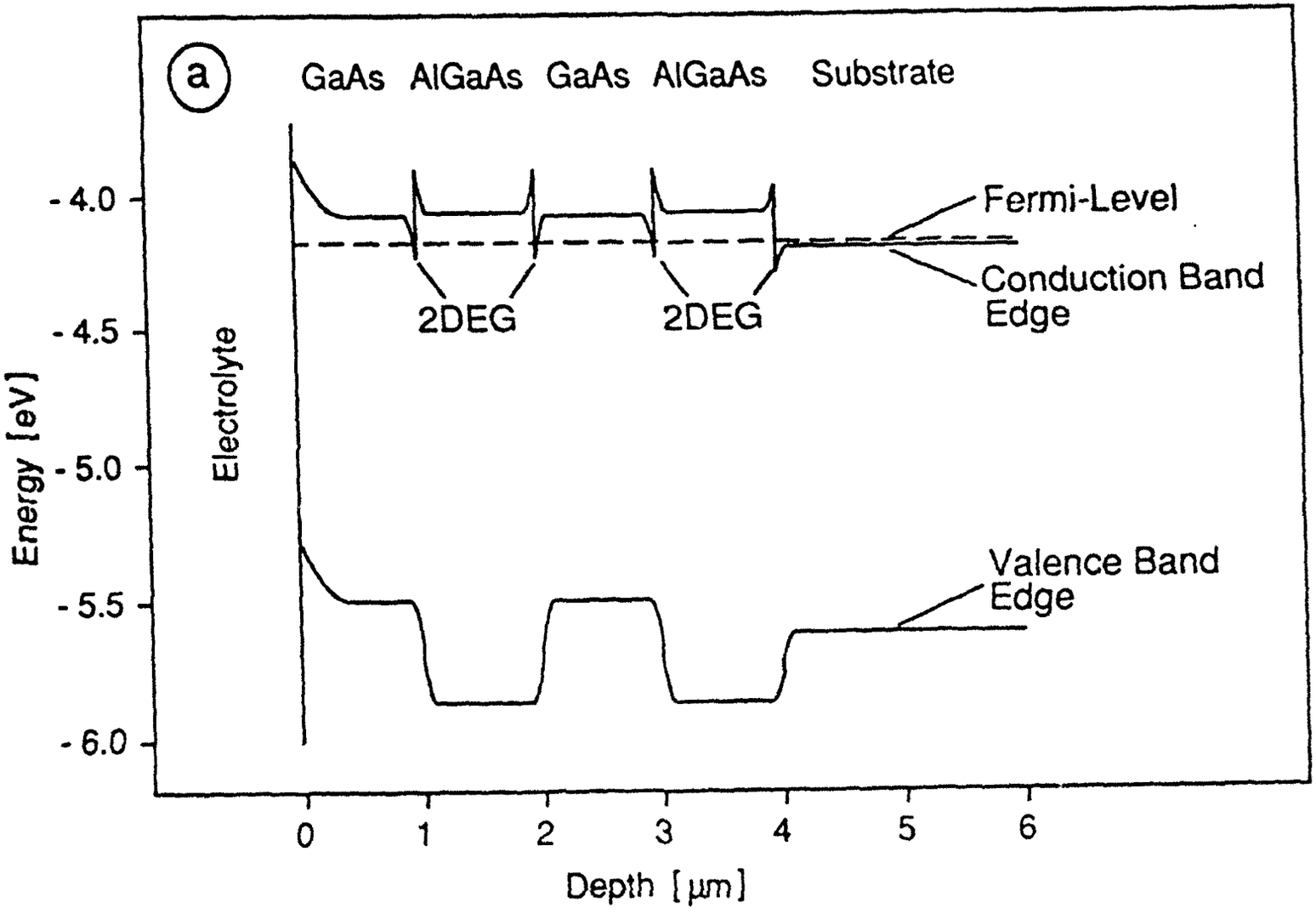
a
GaAs AlGaAs GaAs AlGaAs Substrate
Electrolyte
2DEG
2DEG
Fermi-Level
Conduction Band Edge
Valence Band Edge
Energy [eV]
- 4.0
- 4.5
- 5.0
- 5.5
- 6.0
0
1
2
3
4
5
6
Depth [µm]

Fig. 8a

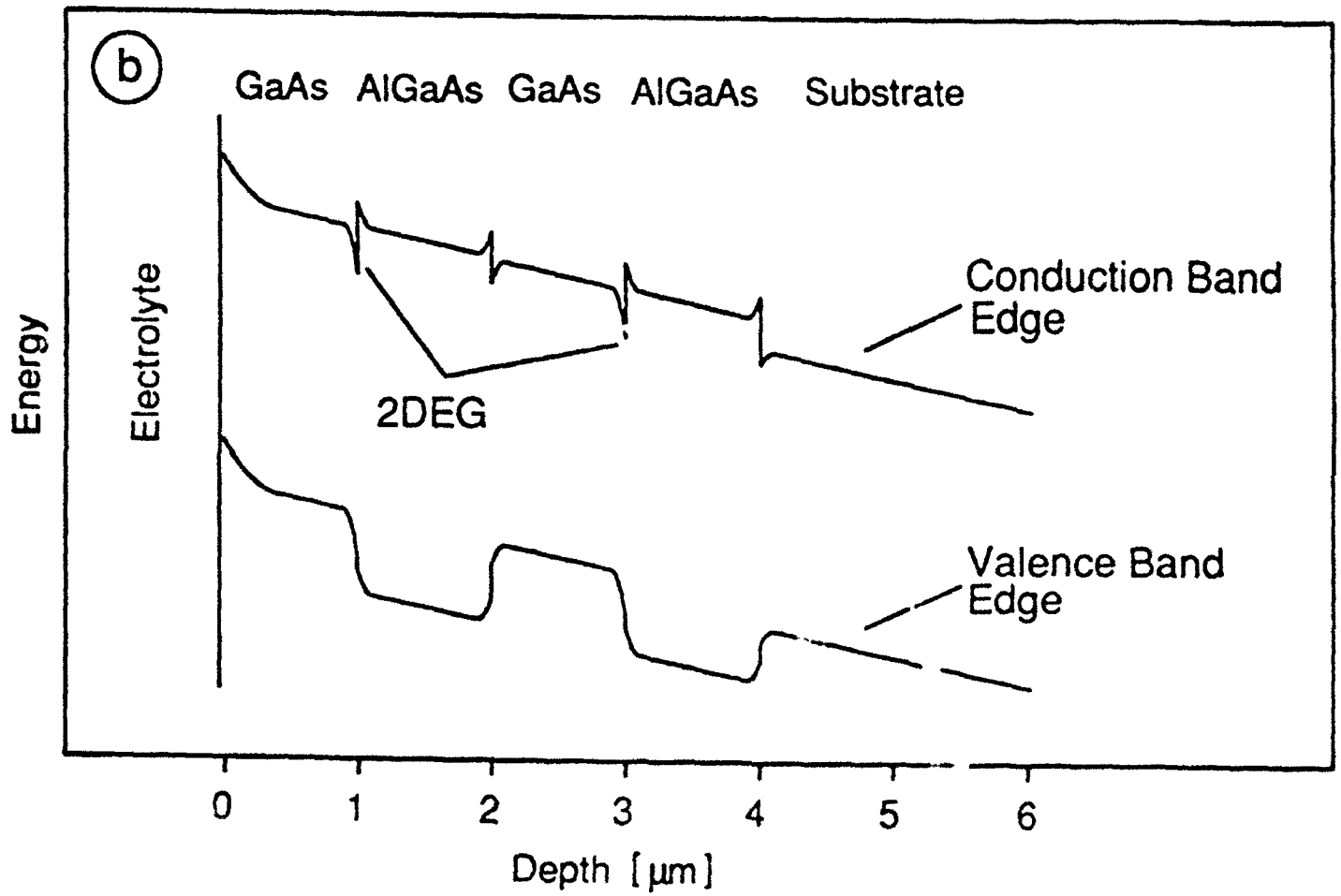
b
GaAs AlGaAs GaAs AlGaAs Substrate
Energy
Electrolyte
Conduction Band Edge
2DEG
Valence Band Edge
0
1
2
3
4
5
6
Depth [μm]

Fig. 8b

Layer 1:
GaAs

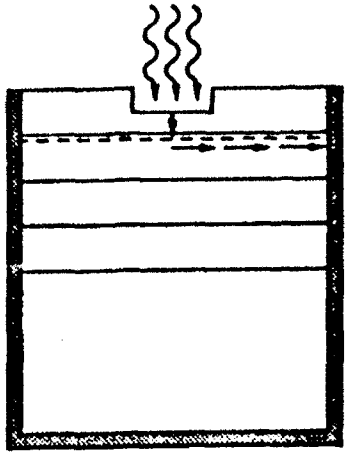

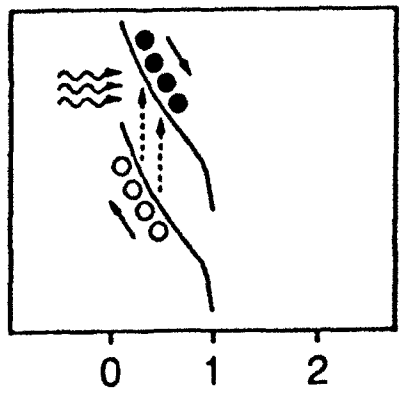

Layer 2:
AlGaAs

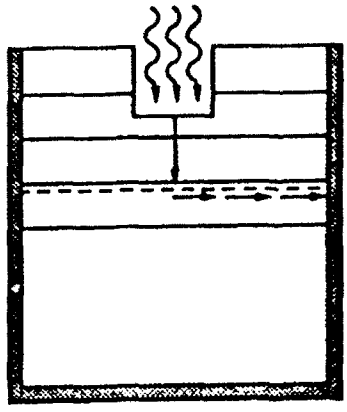

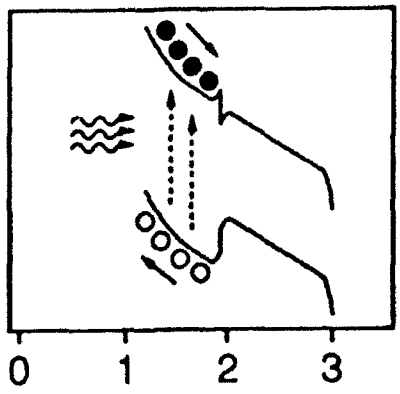

Layer 3:
GaAs

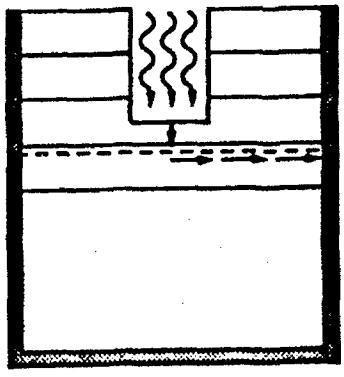

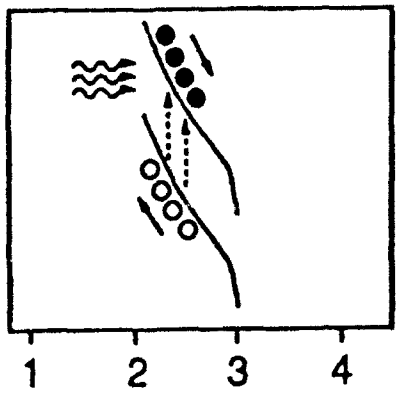

Layer 4:
AlGaAs

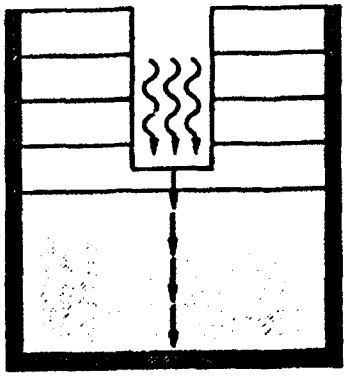

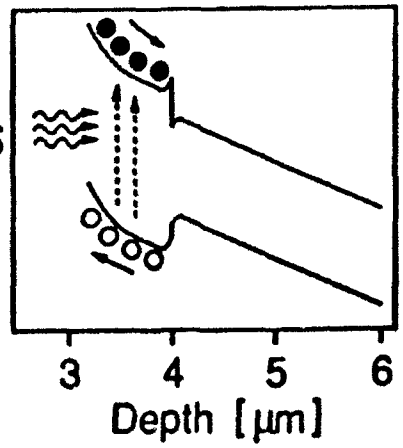

Fig. 9

Fig. 10 a,b

(a) Layer 1: GaAs

2 μm

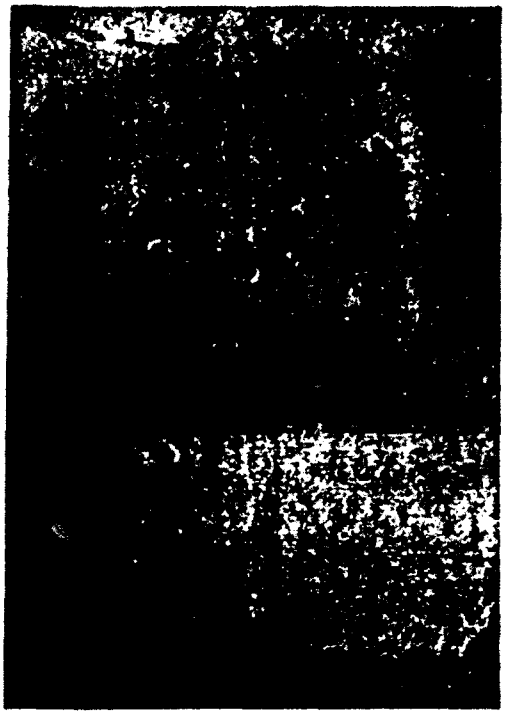

200 μm

(b) Layer 2: AlGaAs

2 μm

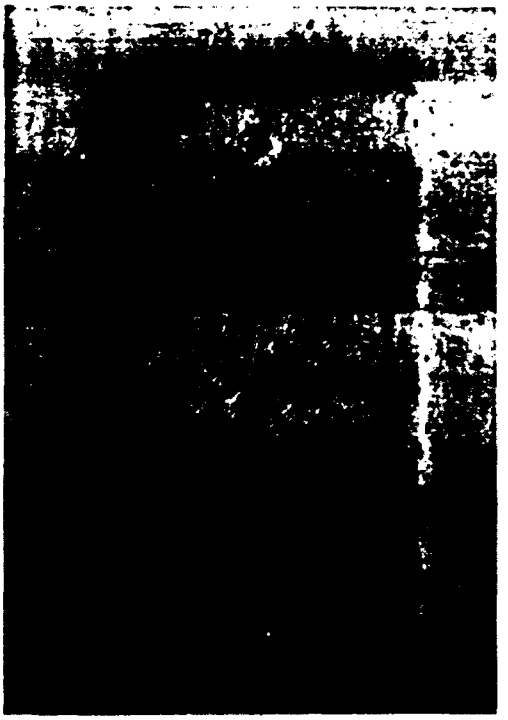

200 μm

Fig. 10 b,d

(c) Layer 3: GaAs

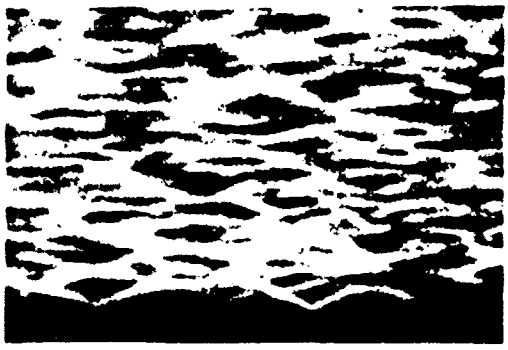

2 μm

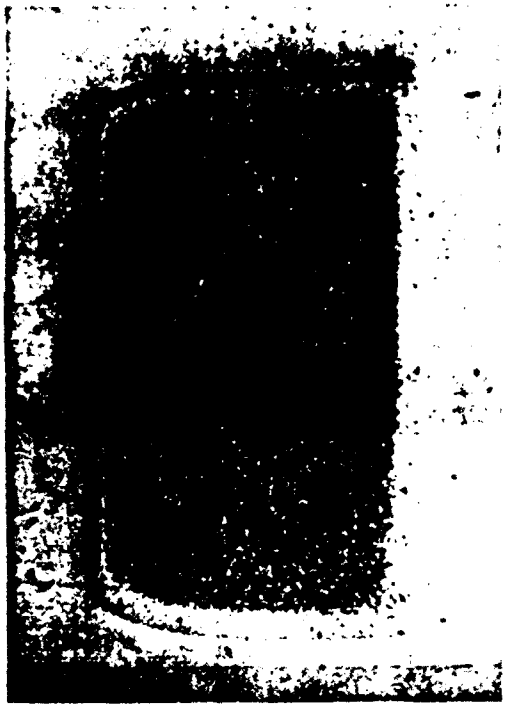

200 μm

(d) Layer 4: AlGaAs

2 μm

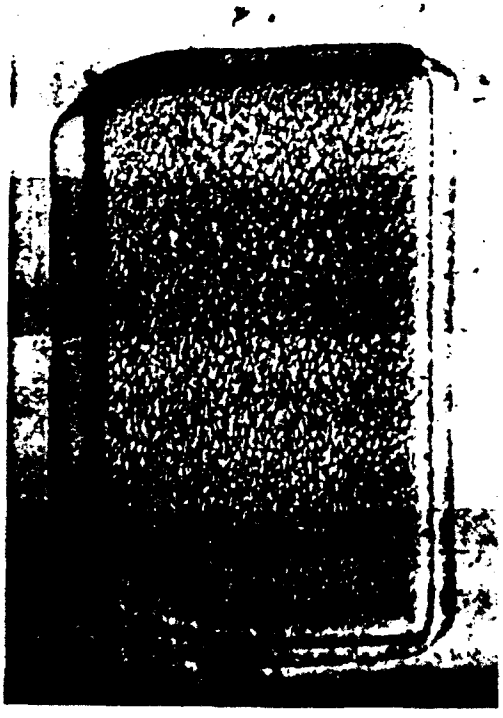

200 μm

Fig. 10 e

(e) Substrate: n^+- GaAs

2 μm

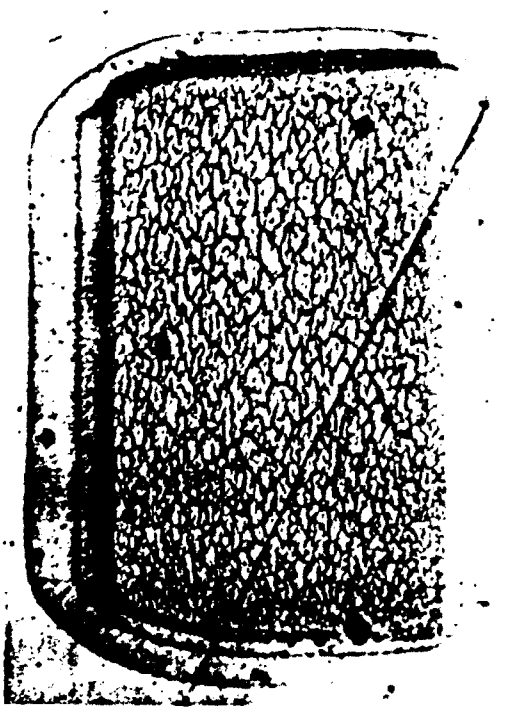

200 μm

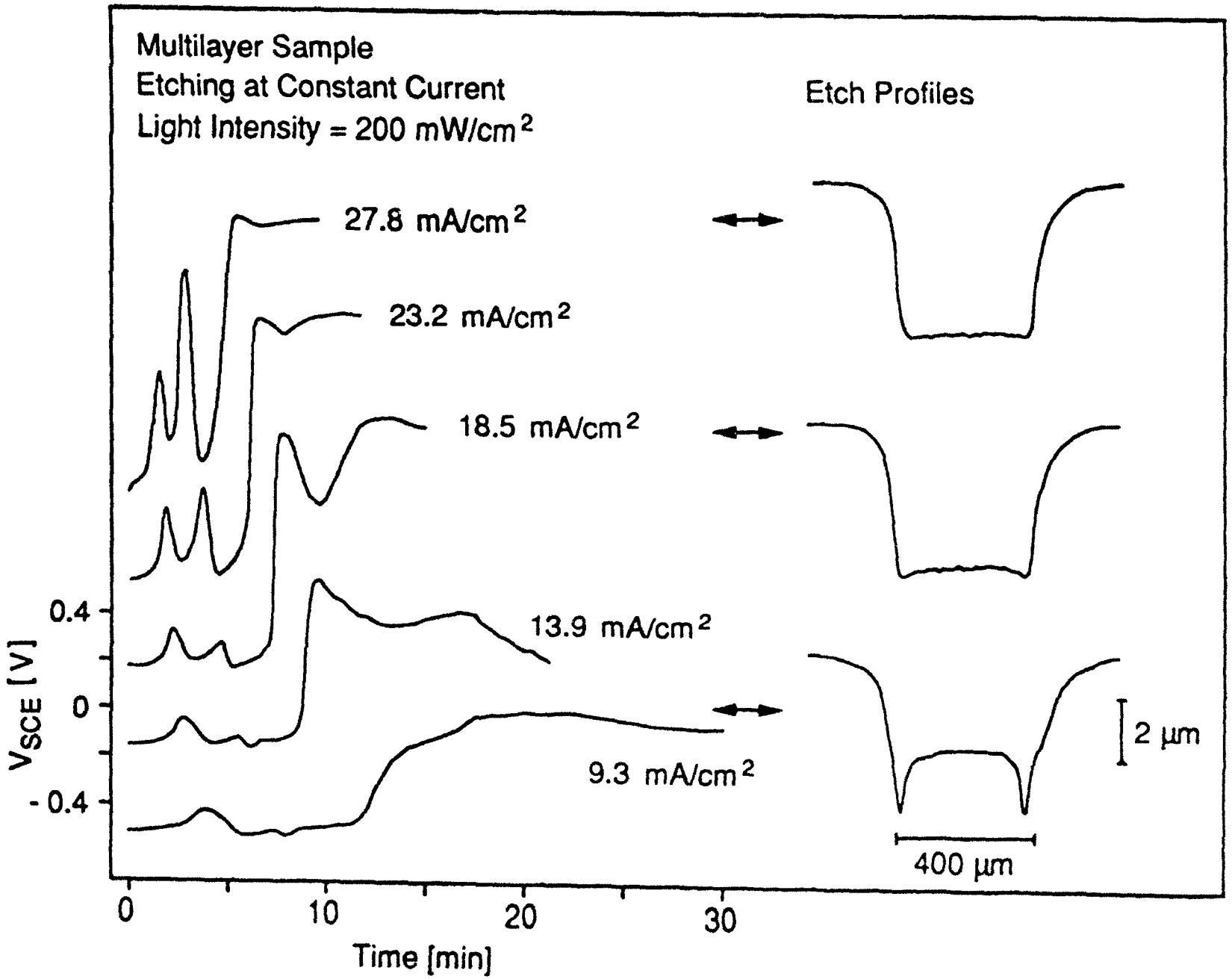
Multilayer Sample
Etching at Constant Current
Light Intensity = 200 mW/cm²
Etch Profiles
27.8 mA/cm²
23.2 mA/cm²
18.5 mA/cm²
13.9 mA/cm²
9.3 mA/cm²
0.4
0
- 0.4
V_SCE [V]
0
10
20
30
Time [min]
2 µm
400 µm

Fig. 11

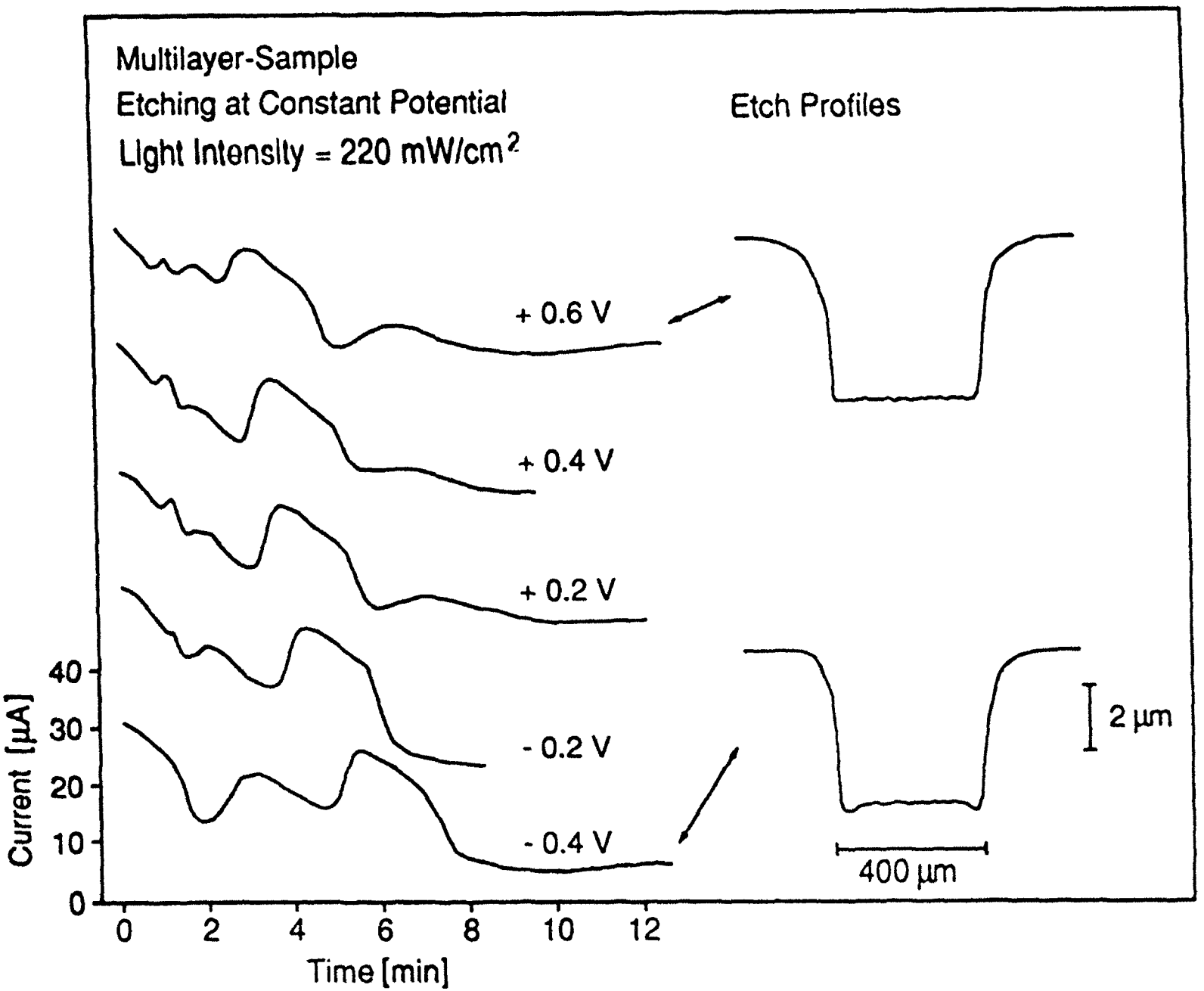
Multilayer-Sample
Etching at Constant Potential
Light Intensity = 220 mW/cm²
Etch Profiles
+ 0.6 V
+ 0.4 V
+ 0.2 V
- 0.2 V
- 0.4 V
2 µm
400 µm
Current [µA]
0
10
20
30
40
0
2
4
6
8
10
12
Time [min]

Fig. 12

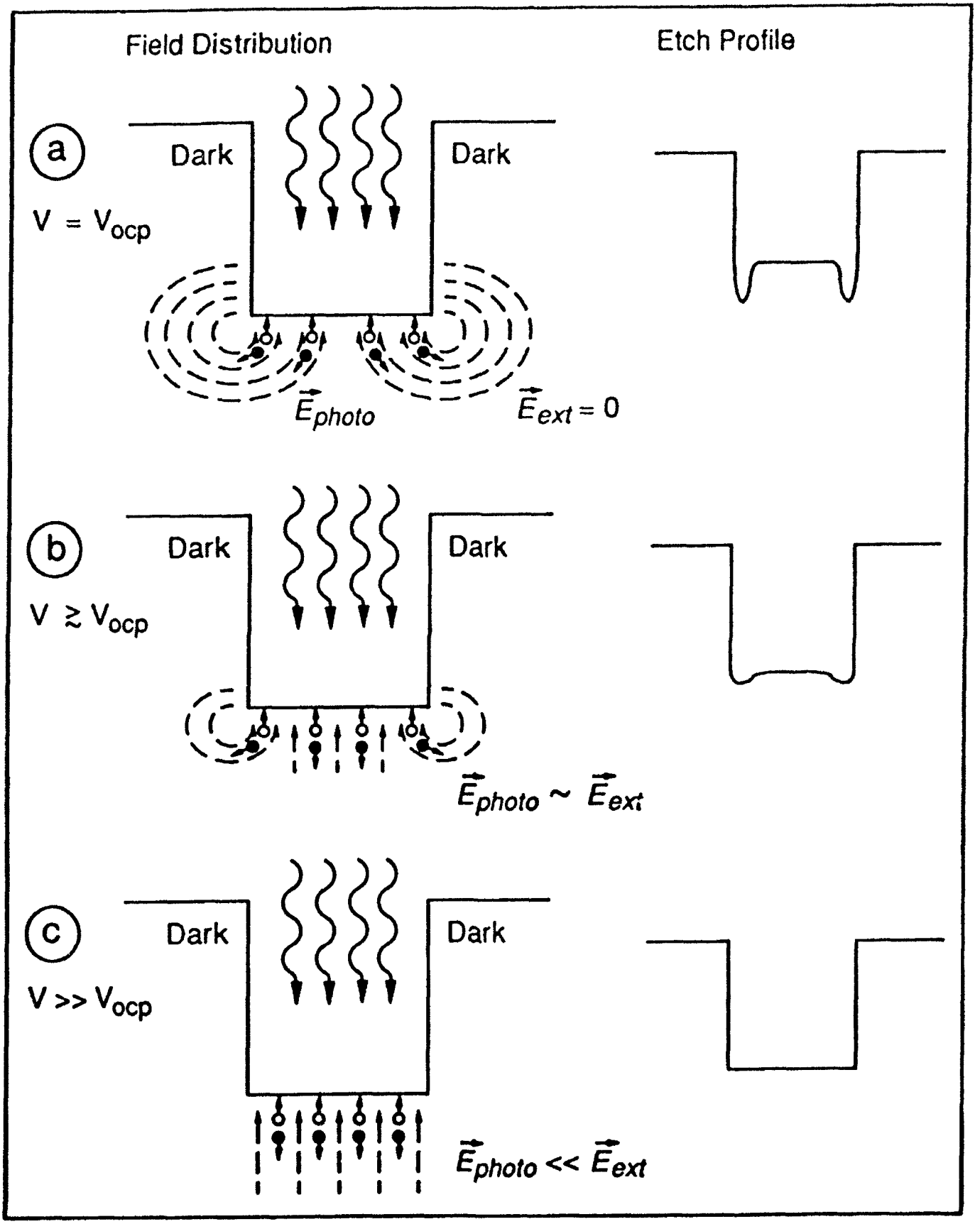
Field Distribution
Etch Profile
a
Dark
Dark
V = Vocp
Ephoto
Eext = 0
b
Dark
Dark
V ≳ Vocp
Ephoto ~ Eext
c
Dark
Dark
V >> Vocp
Ephoto << Eext

Fig. 13

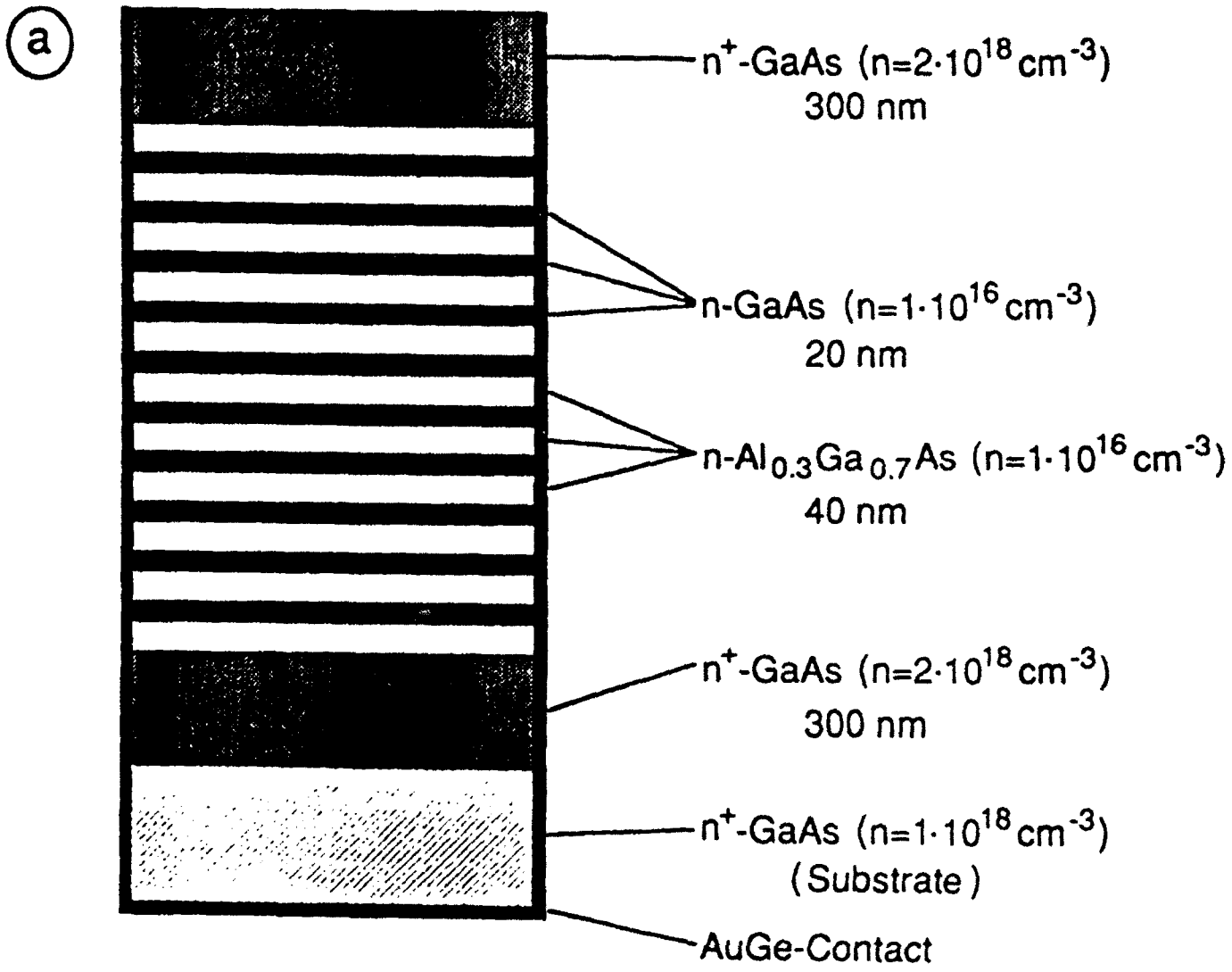
a
n+-GaAs (n=2·10^18 cm^-3)
300 nm
n-GaAs (n=1·10^16 cm^-3)
20 nm
n-Al0.3Ga0.7As (n=1·10^16 cm^-3)
40 nm
n+-GaAs (n=2·10^18 cm^-3)
300 nm
n+-GaAs (n=1·10^18 cm^-3)
(Substrate)
AuGe-Contact

Fig. 14a

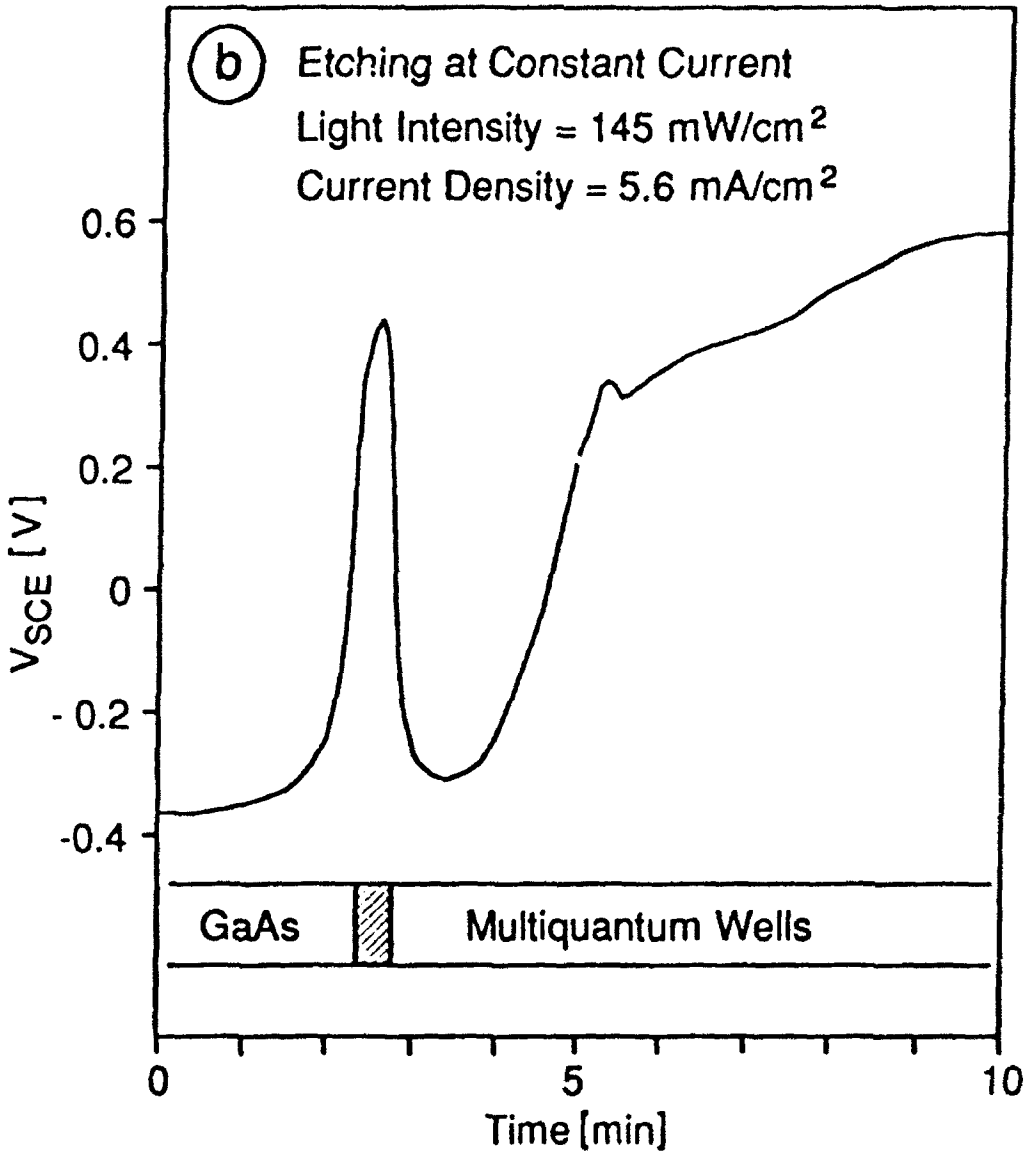
b
Etching at Constant Current
Light Intensity = 145 mW/cm²
Current Density = 5.6 mA/cm²
0.6
0.4
0.2
0
- 0.2
-0.4
V_SCE [V]
GaAs
Multiquantum Wells
0
5
10
Time [min]

Fig. 14b

Fig. 14c,d

(c)

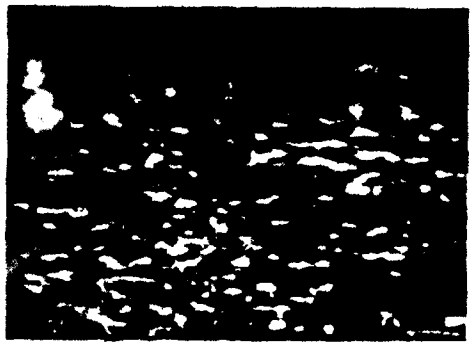

5 µm

(d)

5 µm

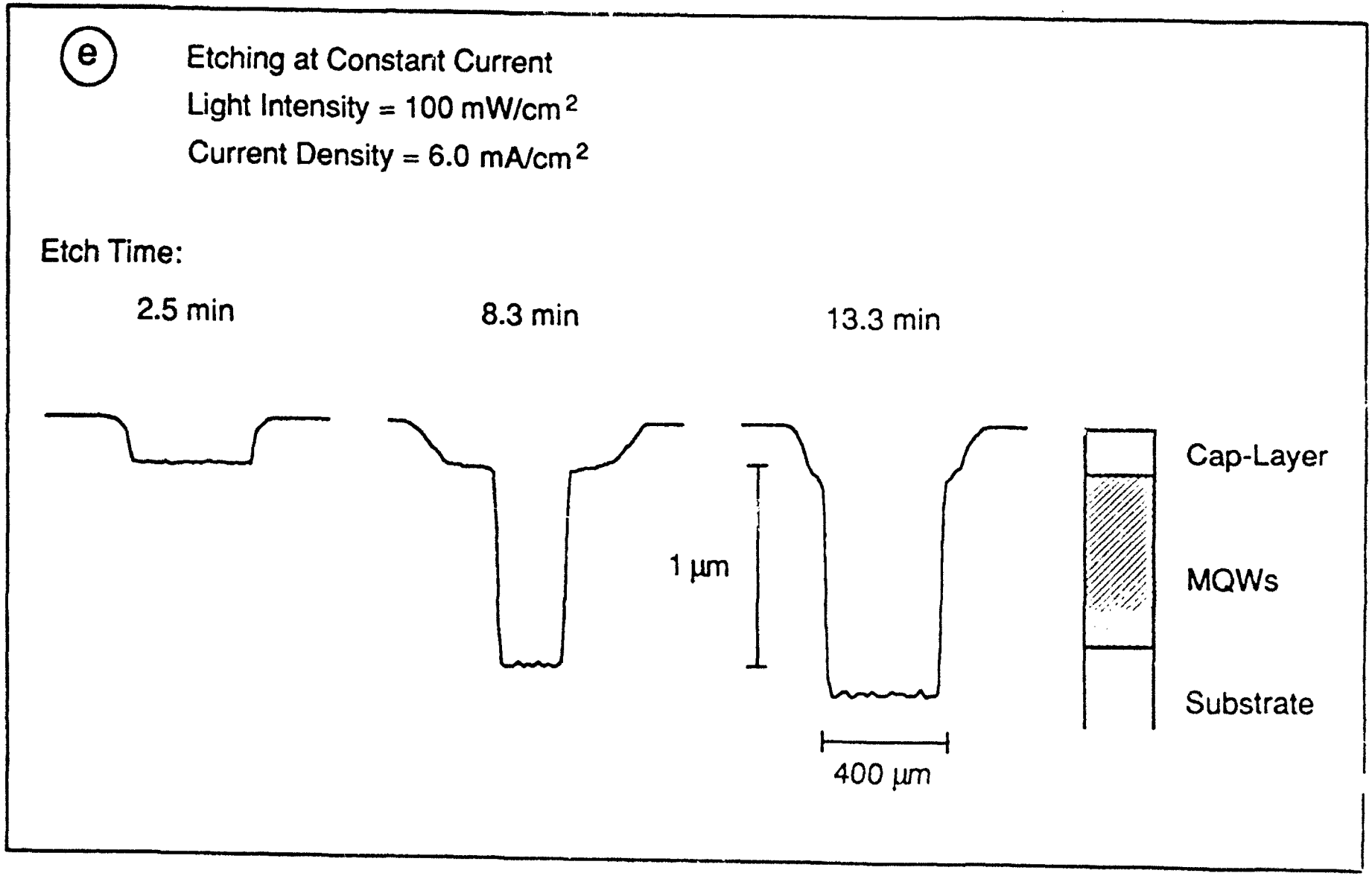
e
Etching at Constant Current
Light Intensity = 100 mW/cm 2
Current Density = 6.0 mA/cm 2
Etch Time:
2.5 min
8.3 min
13.3 min
1 µm
400 µm
Cap-Layer
MQWs
Substrate

Fig. 14e